Quantitative MRI of brain fluids

Jolanda Margaretha Spijkerman

Quantitative MRI of brain fluids

Cover design	Roy Sanders
Lay-out	Roy Sanders
Printed by	Ridderprint, Ridderkerk
ISBN	978-94-6375-231-2

Quantitative MRI of brain fluids

Kwantitatieve MRI van hersenvloeistoffen
(met een samenvatting in het Nederlands)

Proefschrift

ter verkrijging van de graad van doctor aan de Universiteit Utrecht op gezag van de rector magnificus, prof. dr. H.R.B.M. Kummeling, ingevolge het besluit van het college voor promoties in het openbaar te verdedigen op dinsdag 8 januari 2019 des middags te 2.30 uur

door

Jolanda Margaretha Spijkerman

geboren op 10 november 1989 te Nyköping, Zweden

Promotoren: Prof. dr. P.R. Luijten
Prof. dr. J. Hendrikse

Copromotor: Dr. ir. J.J.M. Zwanenburg

This research was supported by the European Research Council under grant agreements n°337333, n°637024, and n°666881.

Financial support by the Dutch Heart Foundation for the publication of this thesis is gratefully acknowledged.

Additional financial support was provided by Alzheimer Nederland.

Contents

Chapter 1

General introduction

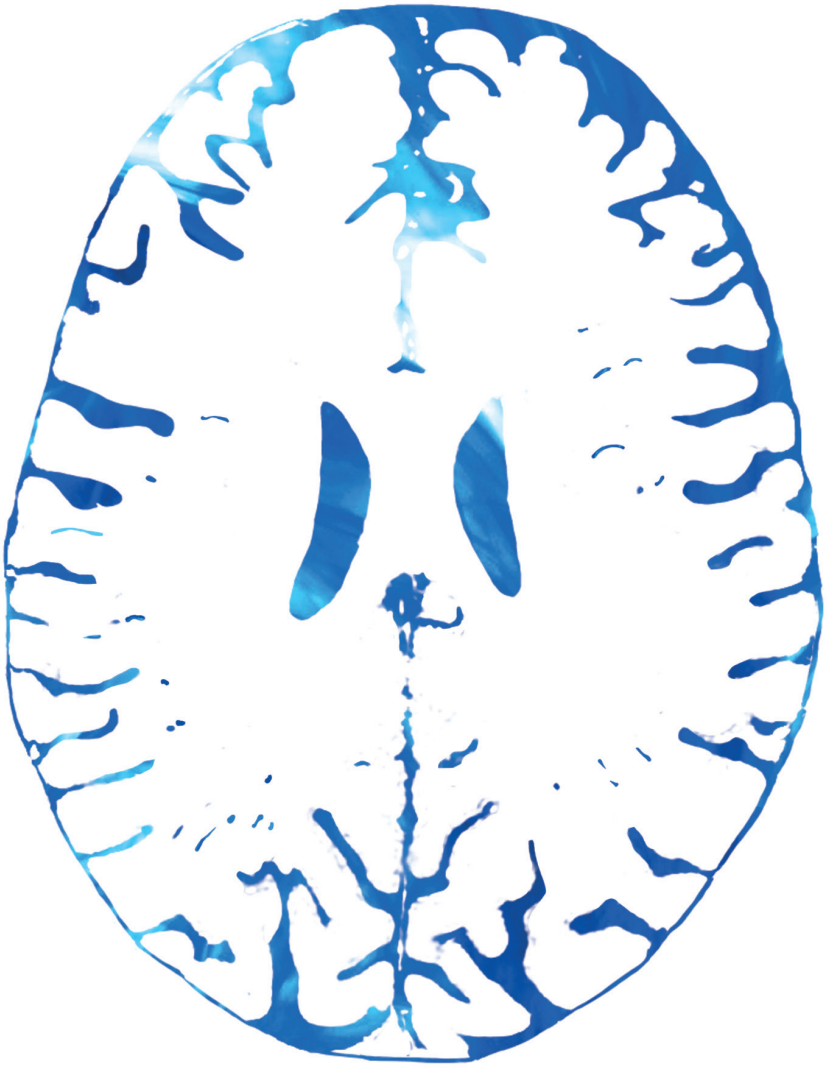

Cerebral Small Vessel Disease

Small Vessel Disease (SVD) can be defined as all pathological processes that affect the small vessels in the brain, including the small arteries and arterioles, capillaries, and small veins (*1*). SVD is a heterogeneous disease, with various pathological features that can occur to the blood vessels. These features include microaneurysms, amyloid deposition, the loss of smooth muscle cells, vessel wall thickening and lumen restriction (*1*). As a result of SVD pathology, brain tissue damage (either hemorrhagic or ischemic) occurs to the cerebral white matter and the deep grey matter (*1, 2*). SVD plays a crucial role in e.g. cognitive impairment and in stroke. SVD is the most common vascular cause of dementia (*3, 4*), and approximately a quarter of all ischemic strokes and a fifth of all strokes are linked to SVD (*1, 4*). However, much remains unclear about SVD. It is for example not clear how the vessels affected by SVD lead to brain tissue damage, or how this brain tissue damage leads to SVD-related cognitive decline and dementia (2). This is mainly due to the lack of tools to study SVD at the level of the small blood vessels, which is where the SVD pathology occurs.

Imaging cerebral Small Vessel Disease

Anatomical magnetic resonance imaging (MRI) offers excellent soft-tissue contrast, and allows for in vivo imaging of the damage to the brain tissue as a consequence of SVD (*2*). The brain tissue damage observed with MRI includes recent small subcortical infarcts, white matter hyperintensities, lacunes, perivascular spaces, cerebral microbleeds, and brain atrophy (*2, 5*), as shown in **Figure 1**. MR imaging of SVD can currently only be achieved by imaging this structural damage to the brain tissue (*2, 6*), as the affected blood vessels are too small to allow for direct (anatomical) imaging. However, the parenchymal pathology is merely a consequence of SVD, and does not reflect the SVD pathology of the small blood vessels itself. Also, the tissue damage occurs in a relatively late stage of SVD (*1, 2, 6*), while it is very important to better understand the development of SVD in earlier stages, in order to investigate the mechanisms linking the blood vessel pathology to the parenchymal pathology.

Current in vivo imaging can only visualize the (irreversible) effect of SVD, i.e. the tissue damage, rather than the small blood vessel pathology. As a result, SVD is not well understood and cannot be monitored in its earliest stage. This may be a major cause for the fact that efforts to develop therapeutic strategies for SVD have not yet been successful (*7*).

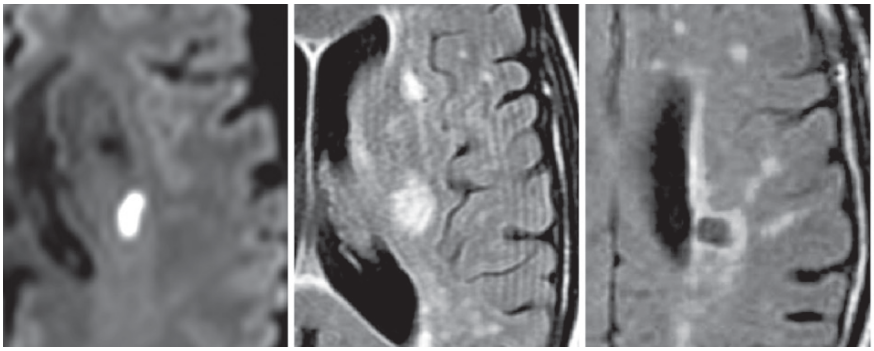

Recent small subcortical infarct | White matter hyperintensities | Lacune

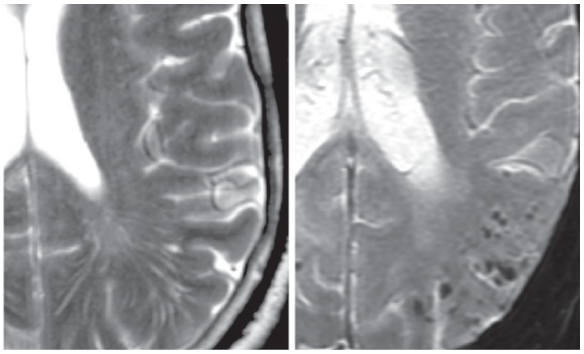

Perivascular spaces | Cerebral microbleeds

Figure 1 Brain tissue damage related to cerebral Small Vessel Disease observed with MRI. A recent small subcortical infarct is shown in a diffusion weighted image (DWI), white matter hyperintensities and a lacune are shown in a fluid attenuated inversion recovery (FLAIR) image, perivascular spaces are shown in a T_2-weighted scan, and cerebral microbleeds are shown in a T_2*-weighted scan.
(This figure is reproduced with permission from Wardlaw et al. (2))

MRI is a highly versatile technique and can also be used to acquire functional information that goes beyond structural imaging. Quantitative magnetic resonance imaging could thus potentially serve as a tool to investigate SVD closer to the level of the small vessels themselves. Three different angles can be chosen to try to assess the earlier stages of SVD in vivo. First, the functioning of the small blood vessels where SVD occurs can be assessed using perfusion measurements or assessment of blood flow velocities and pulsatility *(8, 9)*. Also, (local) brain tissue motion induced by intracranial blood volume variations can be measured (*10, 11*). Second, the brain tissue, where the secondary parenchymal pathology occurs as a consequence of the original vascular pathology, can be assessed. For example, the brain tissue structure can be assessed using diffusion weighted imaging (*12*). Third, the brain fluids, i.e. the cerebrospinal fluid (CSF), perivascular spaces (PVS), and the interstitial fluid, which are linked to both the blood vessels and the brain

tissue, can be targeted by assessment of the brain fluids volume, production rate, or composition. Since much research is already aimed at either (micro) vascular function or microstructural tissue changes, this thesis will focus on the development of methods to study brain fluids.

Role of perivascular spaces in Small Vessel Disease

Perivascular spaces (PVS) are cavities around the (small) brain penetrating blood vessels, filled with a fluid with similar signal intensity as CSF on MRI images. Perivascular spaces play an important physiological role: PVS can act as a conduit for fluid transport and enable exchange between CSF and interstitial fluid (*13*), and PVS are associated with brain clearance (*13–16*) and are therefore probably necessary to maintain homeostasis in the brain (*17*). In young, healthy subjects the largest perivascular spaces have a diameter of approximately 2-3 mm (*2, 18*). PVS with such large diameters can also be observed in scans acquired at commonly used field strengths, for example at 3T (*2, 18*). However, the sizes of PVS show a large distribution with the majority having sub-millimeter diameters. Part of these small PVS can be observed in high-resolution scans acquired at 7T (*2, 18*).

The presence of more and larger perivascular spaces has been linked to SVD (*13, 18, 19*), and to dysfunction of the blood brain barrier in SVD-related (lacunar) stroke (*20*). PVS enlargement correlates with an increased risk for stroke, vascular dementia, and cognitive impairment (*13*). Perivascular spaces may also play a role in other diseases. For example, an asymmetrical PVS count between the left and right hemispheres has been observed in epilepsy patients (*21*). Also, in multiple sclerosis (MS) more and larger PVS were observed compared with healthy controls (*22, 23*). In these patients the higher PVS count was associated with brain atrophy rather than MS lesion load (*22*).

Role of brain fluids in Small Vessel Disease

Additionally to the perivascular spaces, also other brain fluid properties can vary in disease, such as the levels of e.g. amyloid-β in the cerebrospinal fluid (CSF) (*24–27*). CSF serves multiple purposes in the brain. For example, the CSF compensates for intracranial blood volume variations over the cardiac cycle, following the Monro-Kellie hypothesis (*28*), and provides hydromechanical protection of the brain (*29*). Also, brain fluids have been hypothesized to be involved in the clearance of waste from the brain (*14*). Furthermore, brain fluids play a role in the distribution of specific vitamins, hormones, and ions to the brain tissue (*27*).

Supply of new CSF has been hypothesized to be of importance for maintaining homeostasis in the brain (*14, 27*). The general consensus is that CSF is mainly produced by the choroid plexus, and then secreted into the ventricles (*27, 30, 31*). Most of the choroid plexus is located at the lateral ventricles, but the choroid plexus is also partly located at the fourth ventricle (*32*). CSF flows from the ventricles through the cerebral aqueduct towards the subarachnoid space and the spine (27). CSF is re-absorbed in the dural sinuses by arachnoid granulations (*27*). The CSF production rate can be altered in disease. For example, it has been shown that the CSF production rate is reduced in Alzheimer's Disease (AD) (*33*), which may be linked to morphological changes in the choroid plexus (*34*). This makes the CSF production rate an interesting parameter for studying diseases such as SVD. Quantitative measurements of the CSF flow through the cerebral aqueduct can potentially serve as a measure for the CSF production rate in the lateral ventricles.

Impaired brain clearance has also been linked to disease. For example, CSF clearance has been shown to be reduced in AD patients (*35*). This may also be related to the altered solute concentration in brain fluids in disease, as is the case in AD, where e.g. amyloid-β levels in CSF are decreased (*24–27*), which may reflect reduced clearance of amyloid-β from the tissue. The composition of CSF is thus potentially a valuable parameter to investigate SVD. Currently, the CSF composition can only be assessed via a lumbar puncture, which is a highly invasive method. A non-invasive method to assess the (intracranial) CSF composition would therefore be very valuable.

Quantitative MRI measurements of perivascular spaces and brain fluids

(Semi-)quantitative assessment of several brain fluid parameters, such as the perivascular spaces (PVS), the CSF production rate, and (intracranial) CSF content, may be achieved with MRI. Fluid has distinctive MRI relaxation parameters that allow visualization of fluid with high contrast relative to the tissue, which is illustrated in **Figure 2**. This high contrast enables visualization and detection of PVS in MRI images (*36*). In literature the correlation between increased PVS count and SVD and vascular cognitive impairment has been shown using such MRI images (*18, 37–39*). In high-resolution scans acquired at 7T also more (smaller) PVS can be detected compared with lower field strengths, and as a result the PVS count can be determined more extensively. However, it is very labor intensive to determine the PVS count in high-resolution scans, due to the large number of PVS in these

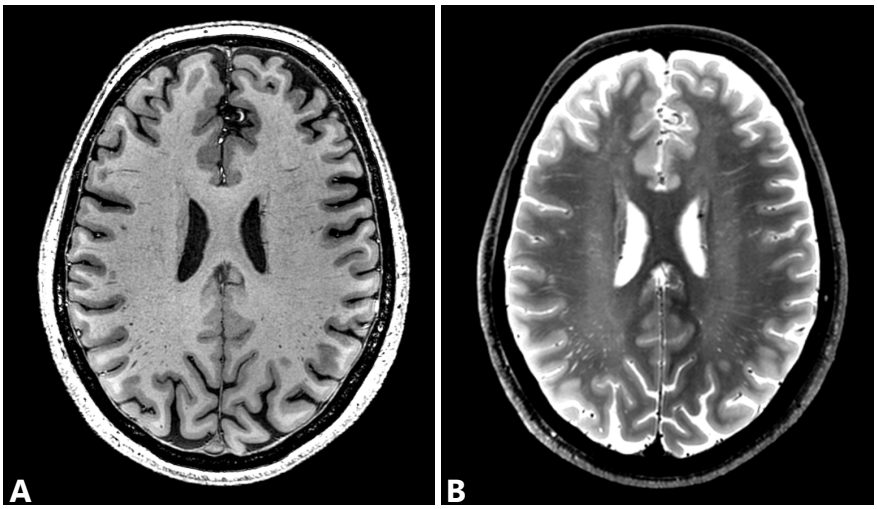

Figure 2 T_1-weighted (A) and T_2-weighted (B) MRI images of the brain, acquired at 7T MRI. The images were taken from a 63-year old woman. In the T_1-weighted image, the cerebrospinal fluid (CSF) and perivascular spaces (PVS) appear dark, whereas the CSF and PVS appear white in the T_2-weighted image.

scans (*18*). Furthermore, 7T MRI is not yet widely available. A method to determine a measure for the PVS count in T_2-weighted scans that have been acquired at lower field strengths, such as 3T, may be very beneficial for SVD research, as 3T MRI is widely available.

Quantitative MRI could potentially also be used to estimate the CSF production rate. MRI is highly sensitive to motion, and can be used to assess even Brownian motion, but also small coherent motion. This motion sensitivity is widely utilized in e.g. MRI phase contrast flow measurements in arteries. In late 1980's this technique was already used to measure net motion of CSF through the cerebral aqueduct as a measure for CSF production rate (*40–42*). In hydrocephalus patients the CSF dynamics and production rate are quite widely studied with phase contrast MRI (PC-MRI) (*43–48*). In these measurements it is generally assumed that the possibly confounding effect of the respiratory cycle on the measurements averages out due to the relatively long acquisition times (*42*). However, no conclusive evidence is available yet to verify this assumption. The cerebral aqueduct is a small structure and the net flow is very small with respect to the CSF pulsations, and therefore precise measurements of the velocity profile are needed. This requires high resolution and SNR for these measurements, whereas in literature mostly net CSF

flows measured at lower field strengths are reported (*46, 49–52*).

Finally, T_2 differences have been observed between ventricular CSF and subarachnoidal CSF using a dedicated CSF T_2 mapping sequence (*53, 54*). The CSF T_2 mapping sequence could potentially be used as a quick measure for atrophy from intracranial CSF volume estimation (*54*), and the T_2 differences may reflect molecular concentration differences (*53*). However, the use of this CSF T_2 mapping method as a measure for CSF composition differences has not been (thoroughly) validated yet. Therefore, the influence of possible confounding factors, such as partial volume and B_0- and B_1-inhomogeneities, is not yet known.

Goal and Outline of this thesis

The overall goal of this thesis is to explore quantitative MRI measurements of brain fluid properties as a potential measure for studying diseases such as SVD. The first two chapters focus on the PVS count in the brain. First, a method is presented to automatically determine the PVS count in high-resolution scans acquired at 7T (**Chapter 2**). This method also determines the length and tortuosity of all detected PVS. It was also investigated if the PVS count can be determined from existing clinical MRI scans acquired at 3T, to increase applicability in (large) clinical studies (**Chapter 3**). Subsequently, the possibility to use net CSF flow measurements using high-resolution PC-MRI at 7T as marker for the CSF production rate by the choroid plexus was investigated, and the effect of respiration on the reproducibility of the PC-MRI measurements was assessed (**Chapter 4**). Specifically, it was investigated whether these measurements are confounded by respiration. Next, the possibility to use quantitative T_2 mapping as a marker for CSF composition differences between brain regions was explored (**Chapter 5**). Regional CSF T_2 differences have been observed previously, and in this chapter the influence of possible confounding factors (B_0, B_1, and partial volume) are investigated. In the final chapter the main findings described in this thesis are discussed (**Chapter 6**).

References

1. L. Pantoni, Cerebral small vessel disease: from pathogenesis and clinical characteristics to therapeutic challenges. *Lancet Neurol*. 9, 689–701 (2010).
2. J. M. Wardlaw *et al.*, Neuroimaging standards for research into small vessel disease and its contribution to ageing and neurodegeneration. *Lancet Neurol*. 12, 822–838 (2013).
3. G. C. Román, T. Erkinjuntti, A. Wallin, L. Pantoni, H. C. Chui, Subcortical ischaemic vascular dementia. *Lancet Neurol*. 1, 426–436 (2002).
4. J. M. Wardlaw, C. Smith, M. Dichgans, Mechanisms of sporadic cerebral small vessel disease: Insights from neuroimaging. *Lancet Neurol*. 12, 483–497 (2013).
5. L. J. L. Craggs, Y. Yamamoto, V. Deramecourt, R. N. Kalaria, Microvascular pathology and morphometrics of sporadic and hereditary small vessel diseases of the brain. *Brain Pathol*. 24, 495–509 (2014).
6. J. J. M. Zwanenburg, M. J. P. van Osch, Targeting Cerebral Small Vessel Disease With MRI. *Stroke.* 48, 3175–3182 (2017).
7. P. M. Bath, J. M. Wardlaw, Pharmacological treatment and prevention of cerebral small vessel disease: A review of potential interventions. *Stroke.* 10, 469–478 (2015).
8. W. H. Bouvy *et al.*, Assessment of blood flow velocity and pulsatility in cerebral perforating arteries with 7-T quantitative flow MRI. *NMR Biomed*. 29, 1295–1304 (2016).
9. H. S. Markus, D. J. Lythgoe, L. Ostegaard, M. O'Sullivan, S. C. Williams, Reduced cerebral blood flow in white matter in ischemic leukoaraiosis demonstrated using quantitative exogeneous contrast based perfusion *MRI. J Neurol Neurosurg Psychiatry*. 69, 48–53 (2000).
10. A. Adams, P. R. Luijten, J. J. M. Zwanenburg, in *ISMRM proceedings* (2017), p. 704.
11. I. Terem *et al.*, Revealing sub-voxel motions of brain tissue using phase-based amplified MRI. *Magn. Reson. Med*. (2018), doi:10.1002/mrm.27236.
12. Y. D. Reijmer *et al.*, Microstructural white matter abnormalities and cognitive functioning in type 2 diabetes: A diffusion tensor imaging study. *Diabetes Care*. 36, 137–144 (2013).
13. R. Brown *et al.*, Understanding the role of the perivascular space in cerebral small vessel disease. *Cardiovasc. Res*. (2018), doi:https://doi.org/10.1093/cvr/cvy113.
14. N. J. Abbott, M. E. Pizzo, J. E. Preston, D. Janigro, R. G. Thorne, The role of brain barriers in fluid movement in the CNS: is there a 'glymphatic' system? *Acta Neuropathol.* 135, 387–407 (2018).
15. A. Bacyinski, M. Xu, W. Wang, J. Hu, The paravascular pathway for brain waste clearance: Current understanding, significance and controversy. *Front. Neuroanat*. 11, 1–8 (2017).
16. A. J. Smith, A. S. Verkman, The "glymphatic" mechanism for solute clearance in Alzheimer's disease: game changer or unproven speculation? *FASEB J*. 32, 543–551 (2018).
17. B. Engelhardt *et al.*, Fluids and barriers of the CNS establish immune privilege by confining immune surveillance to a two-walled castle moat surrounding the CNS castle. *Fluids Barriers CNS*. 8, 4 (2011).
18. W. H. Bouvy *et al.*, Perivascular spaces on 7 Tesla brain MRI are related to markers of small vessel disease but not to age or cardiovascular risk factors. *JCBFM*. 36, 1708–1717 (2016).
19. R. P. W. Rouhl, R. J. van Oostenbrugge, I. L. H. Knottnerus, J. E. A. Staals, J. Lodder, Virchow-Robin spaces relate to cerebral small vessel disease severity. *J. Neurol*. 255, 692–696 (2008).

20. J. M. Wardlaw *et al.*, Lacunar stroke is associated with diffuse Blood-Brain barrier dysfunction. *Ann. Neurol*. 65, 194–202 (2009).

21. R. E. Feldman *et al.*, Quantification of perivascular spaces at 7 T : A potential MRI biomarker for epilepsy. *Seizure*. 54, 11–18 (2018).

22. I. D. Kilsdonk *et al.*, Perivascular spaces in MS patients at 7 Tesla MRI: A marker of neurodegeneration? *Mult. Scler. J*. 21, 155–162 (2015).

23. J. Wuerfel *et al.*, Perivascular spaces - MRI marker of inflammatory activity in the brain? *Brain*. 131, 2332–2340 (2008).

24. L. M. Shaw *et al.*, Cerebrospinal fluid biomarker signature in Alzheimer's disease neuroimaging initiative subjects. *Ann Neurol*. 65, 403–413 (2009).

25. K. Blennow, H. Zetterberg, The past and the future of Alzheimer's disease CSF biomarkers - a journey toward validated biochemical tests covering the whole spectrum of molecular events. *Front. Neurosci.* 9, 1–8 (2015).

26. A. Lleó *et al.*, Cerebrospinal fluid biomarkers in trials for Alzheimer and Parkinson diseases. *Nat. Rev. Neurol.* 11, 41–55 (2015).

27. R. Spector, S. Robert Snodgrass, C. E. Johanson, A balanced view of the cerebrospinal fluid composition and functions: Focus on adult humans. *Exp. Neurol.* 273, 57–68 (2015).

28. B. Mokri, The Monro-Kellie hypothesis. *Neurology*. 56, 1746–1748 (2001).

29. L. Sakka, G. Coll, J. Chazal, Anatomy and physiology of cerebrospinal fluid. *Eur. Ann. Otorhinolaryngol. Head Neck Dis*. 128, 309–316 (2011).

30. N. J. Abbott, Evidence for bulk flow of brain interstitial fluid: significance for physiology and pathology. *Neurochem Int*. 45, 545–552 (2004).

31. S. B. Hladky, M. A. Barrand, Mechanisms of fluid movement into, through and out of the brain: evaluation of the evidence. *Fluids Barriers CNS*. 11, 26–57 (2014).

32. K. M. Dziegielewska, C. J. Ek, M. D. Habgood, N. R. Saunders, Development of the choroid plexus. *Microsc. Res. Tech.* 52, 5–20 (2001).

33. G. D. Silverberg *et al.*, The cerebrospinal fluid production rate is reduced in dementia of the Alzheimer's type. *Neurology*. 57, 1763–1766 (2001).

34. J. M. Serot, M. C. Béné, B. Foliguet, G. C. Faure, Morphological alterations of the choroid plexus in late-onset Alzheimer's disease. *Acta Neuropathol.* 99, 105–108 (2000).

35. M. J. de Leon *et al.*, CSF clearance in Alzheimer Disease measured with dynamic PET. *J. Nucl. Med*., 1471–1476 (2017).

36. W. H. Bouvy *et al.*, Visualization of perivascular spaces and perforating arteries with 7 T magnetic resonance imaging. *Invest. Radiol*. 49, 307–313 (2014).

37. F. N. Doubal, A. M. J. MacLullich, K. J. Ferguson, M. S. Dennis, J. M. Wardlaw, Enlarged perivascular spaces on MRI are a feature of cerebral Small Vessel Disease. *Stroke*. 41, 450–454 (2010).

38. C. Moran, T. G. Phan, V. K. Srikanth, Cerebral small vessel disease : a review of clinical , radiological , and histopathological phenotypes. *Int. J. Alzheimers. Dis.* 7, 36–46 (2012).

39. V. Deramecourt *et al.*, Staging and natural history of cerebrovascular pathology in dementia. *Neurology*. 78, 1043–1050 (2012).

40. D. A. Feinberg, A. S. Mark, Human brain motion and cerebrospinal fluid circulation demonstrated with MR velocity imaging. *Radiology*. 163, 793–799 (1987).

41. F. Ståhlberg *et al.*, A method for MR quantification of flow velocities in blood and CSF using interleaved gradient-echo pulse sequences. *Magn. Reson. Imaging*. 7, 655–667 (1989).

42. D. R. Enzmann, N. J. Pelc, Cerebrospinal fluid flow measured by phase-contrast cine MR. *Am J Neuroradiol.* 14, 1301–1307 (1993).

43. P. Gideon *et al.*, Cerebrospinal fluid flow and production in patients with normal pressure hydrocephalus studied by MRI. *Neuroradiology*. 36, 210–215 (1994).

44. P. H. Luetmer *et al.*, Measurement of cerebrospinal fluid flow at the cerebral aqueduct by use of phase-contrast magnetic resonance imaging: Technique validation and utility in diagnosing idiopathic normal pressure hydrocephalus. *Neurosurgery*. 50, 534–543 (2002).

45. G. A. Bateman, C. R. Levi, P. Schofield, Y. Wang, E. C. Lovett, The pathophysiology of the aqueduct stroke volume in normal pressure hydrocephalus: Can co-morbidity with other forms of dementia be excluded? *Neuroradiology*. 47, 741–748 (2005).

46. O. Balédent *et al.*, Relationship between cerebrospinal fluid and blood dynamics in healthy volunteers and patients with communicating hydrocephalus. *Invest. Radiol*. 39, 45–55 (2004).

47. S. El Sankari *et al.*, Cerebrospinal fluid and blood flow in mild cognitive impairment and Alzheimer's disease: A differential diagnosis from idiopathic normal pressure hydrocephalus. *Fluids Barriers CNS*. 8, 12 (2011).

48. G. Ringstad, K. E. Emblem, P. K. Eide, Phase-contrast magnetic resonance imaging reveals net retrograde aqueductal flow in idiopathic normal pressure hydrocephalus. *J. Neurosurg*. 124, 1850–1857 (2016).

49. K. Yoshida *et al.*, Phase-contrast MR studies of CSF flow rate in the cerebral aqueduct and cervical subarachnoid space with correlation-based segmentation. *Magn. Reson. Med. Sci.* 8, 91–100 (2009).

50. S. K. Piechnik, P. E. Summers, P. Jezzard, J. V. Byrne, Magnetic resonance measurement of blood and CSF flow rates with phase contrast - Normal values, repeatability and CO_2 reactivity. *Acta Neurochir. Suppl*., 263–270 (2008).

51. A. Wåhlin *et al.*, Phase contrast MRI quantification of pulsatile volumes of brain arteries, veins, and cerebrospinal fluids compartments: Repeatability and physiological interactions. *J. Magn. Reson. Imaging*. 35, 1055–1062 (2012).

52. C. B. Beggs *et al.*, Aqueductal cerebrospinal fluid pulsatility in healthy individuals is affected by impaired cerebral venous outflow. *J. Magn. Reson. Imaging*. 40, 1215–1222 (2014).

53. Q. Qin, A simple approach for three-dimensional mapping of baseline cerebrospinal fluid volume fraction. *Magn Reson Med*. 65, 385–391 (2011).

54. J. B. de Vis *et al.*, Cerebrospinal fluid volumetric MRI mapping as a simple measurement for evaluating brain atrophy. *Eur. Radiol.* 26, 1254–1262 (2016).

Chapter 2

Automatic quantification of perivascular spaces in T_2-weighted images at 7T MRI

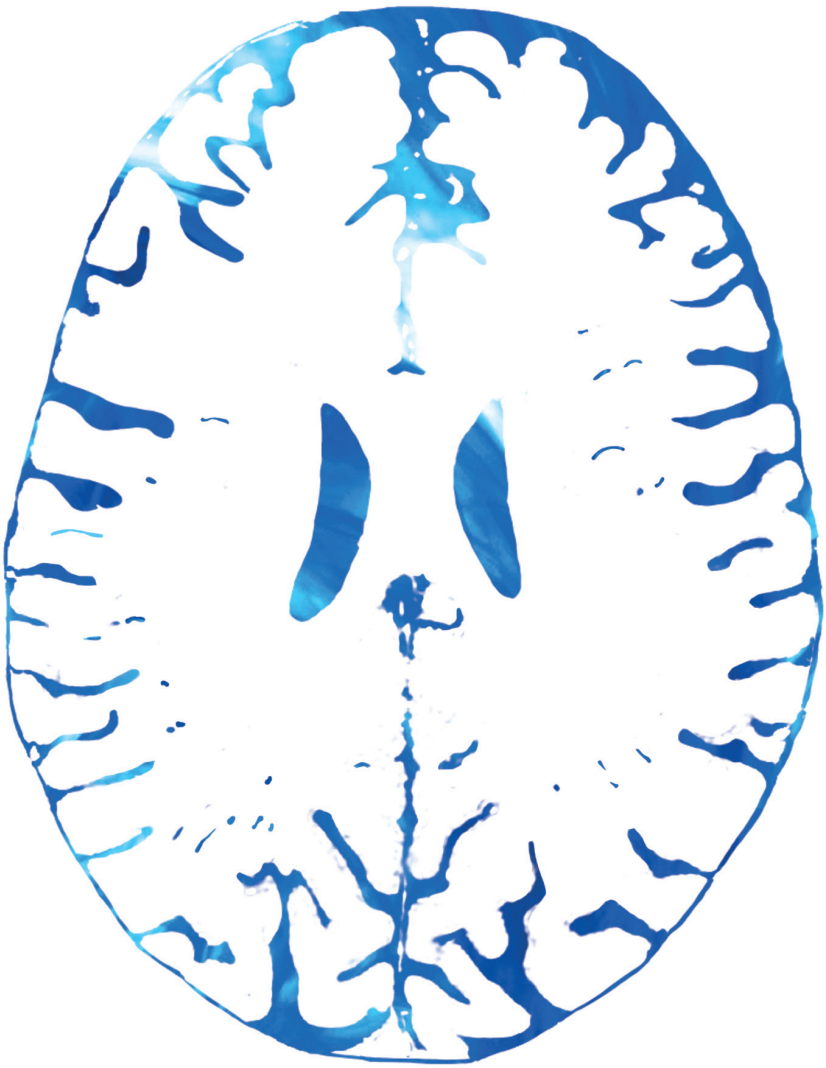

Jolanda M. Spijkerman, Jaco J.M. Zwanenburg, Willem H. Bouvy, Mirjam I. Geerlings, Geert-Jan Biessels, Jeroen Hendrikse, Peter R. Luijten, Hugo J. Kuijf

Submitted

Abstract

Objective

Perivascular spaces (PVS) are believed to be involved in brain waste disposal. PVS are associated with cerebral small vessel disease. At higher field strengths more PVS can be observed, which is challenging for manual PVS assessment. The aim of this work was therefore to develop a method to automatically detect and quantify PVS.

Methods

A machine learning approach identified possible PVS in an automatically positioned region-of-interest (ROI) in the centrum semiovale (CSO), based on signal intensities in high-resolution T_2-weighted TSE scans and vesselness values. Next, 3D PVS tracking was performed in 50 subjects, and quantitative measures were extracted. Maps of PVS density, length, and tortuosity were created. Manual PVS annotations were available to train and validate the automatic method.

Results

Good correlation was found between the automatic and manual PVS: ICC (absolute/consistency) is 0.64/0.75, and DSC is 0.61. For 20 subjects manual PVS annotations of a second observer were available. Compared with the correlation between the automatic and manual PVS, higher inter-observer ICC was observed (0.85/0.88), but DSC was lower (0.49 in 4 subjects).

Conclusion

Our fully automatic method can detect PVS in a 2D slab in the CSO, and extract quantitative PVS parameters by performing 3D tracking. This method enables automated quantitative analysis of PVS in healthy and diseased subjects.

Introduction

Perivascular spaces (PVS) are fluid-filled spaces around the brain-perforating blood vessels (*1*), and are connected to the cerebrospinal fluid (CSF) in the subarachnoidal space. PVS can be observed in MRI images, where they appear with a (visually) similar signal intensity as CSF (*1*). PVS are believed to be involved in the clearance of waste products from the brain (*2*, *3*). Furthermore, the appearance of more and/or larger perivascular spaces has been linked to aging (*4–6*) and is a feature of cerebral Small Vessel Disease (SVD) (*6–8*). Therefore, perivascular spaces are highly relevant when investigating the healthy and diseased brain.

Currently, PVS are mostly evaluated visually, using qualitative measures such as a rating scale for PVS counts in brain regions like the basal ganglia (BG) and the centrum semiovale (CSO) (*9–11*). The actual PVS count could offer a more precise method to determine PVS load, as this results in a continuous scale rather than an ordinal scale, thereby eliminating discretization and ceiling effects. However, manual annotation is highly labor intensive, especially at higher field strengths where high numbers of PVS are observed (*12*). Also, inter-rater differences remain, since for example (very) small PVS can easily be confused with motion-artefacts or noise. It is illustrative that in a recent 7T study on average more than 70 PVS could be counted in a single slice from one hemisphere (*12*), making their manual assessment very labor intensive. This limits further evaluation of PVS in high resolution scans, regarding e.g. PVS asymmetry (*13*). Still, even if manual PVS annotation would be feasible, it lacks additional quantitative information. An automatic method would be easier to apply and eliminates inter-rater variability, and could be used to acquire quantitative PVS measures, such as PVS length and tortuosity.

In this work a method was developed to automatically detect and quantify PVS in the centrum semiovale. Automatic PVS detection was performed in an automatically determined region-of-interest (ROI) in the CSO. The method was trained and validated with manual PVS annotations that were available in a single slice in the CSO, in the right hemisphere (*12*). Tracking of all automatically detected PVS resulted in PVS length and PVS tortuosity measurements in these subjects.

Methods

Data

Scans of 50 subjects (19 male, mean age 62.9 years, age range 27 – 78 years) from two earlier studies with identical 7T protocols were used. Scans of 30 participants of the PREDICT-MR study (*14*), and scans of 20 participants of the second Utrecht Diabetic Encephalopathy Study (UDES2) were available (*15*). PREDICT-MR and UDES2 were approved by the medical ethics committee of the University Medical Center Utrecht (UMCU), and all subjects gave written informed consent. The guidelines of the Declaration of Helsinki of 1975 were followed. The PREDICT subjects were randomly recruited in waiting rooms of general practices and had no cognitive impairment. The UDES2 subjects were recruited through their general practitioners, and had no cognitive impairment. Of the 20 UDES2 subjects included in this study, 8 subjects had diabetes mellitus. The used data is described in detail by Bouvy *et al.* (*12*). Briefly, for all subjects a 3D T_2-weighted TSE scan acquired at 7T was available, with 0.7 mm isotropic resolution, reconstructed to 0.35 mm isotropic. TR/TE were 3158/301 ms. Also, for all subjects a T_1-weighted TFE scan acquired at 7T was available, with 1 mm acquired isotropic resolution, reconstructed to 0.66×0.66×0.5 mm^3. TR/TE were 4.8/2.2 ms. For all subjects PVS markers from an expert observer were available in the centrum semiovale, in the right hemisphere (*12*) of a predefined slice. This slice was located in the CSO, 1 cm above the most cranial slice where the lateral ventricles were visible. For subjects of the UDES2 study also PVS markers of a second observer were available.

Semi-automatic PVS detection and tracking

The T_1-weighted scans were used for segmentation of the white matter (WM) using SPM12 (*16*). The WM mask was registered to the T_2-weighted scans using rigid registration with elastix (*17*). To enhance all vessel-like structures, the T_2-weighted scans were filtered with a vesselness filter. We used a multi-scale 3D vesselness implementation as proposed by Sato *et al.* (*18*). Specifically, we computed 10 scales with uniform distributed sigma ranging from 0.30 – 1.00 mm (inclusive) as implemented in MeVisLab (*18–20*). Subsequently, a plane was automatically positioned in the CSO, parallel to the line connecting the genu and splenium of the corpus callosum, perpendicular to the midsagittal plane, and 10 mm above the lateral ventricles. The genu and splenium and the midsagittal plane were automatically detected as described elsewhere (*21–23*). The CSO-plane was extended to a slab of 7 slices, and the CSO region-of interest (CSO-ROI) was defined as the WM in this slab. **Figure 1** shows an example of the automatically positioned CSO-plane for one subject.

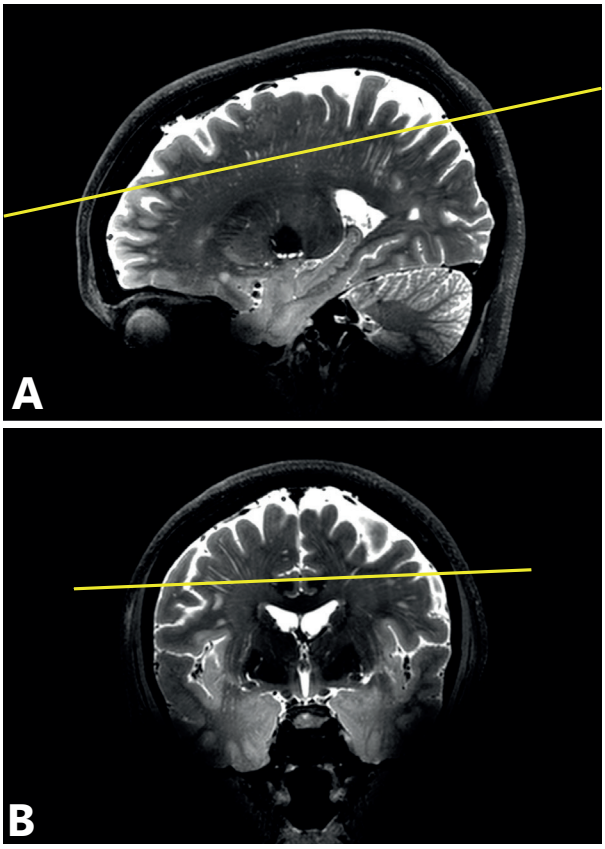

Figure 1 Automatically determined CSO plane (yellow) in one subject (T_2-weighted TSE scan), in sagittal (A) and coronal (B) view. The CSO plane is located 1 cm above the ventricles, and is oriented parallel to the line connecting the bottom of the genu and splenium of the corpus callosum, and perpendicular to the midsagittal plane.

For the automatic PVS detection, PVS probability maps were created based on a binary kNN classifier (*24*) trained using the T_1 and T_2 signal intensities, and the vesselness values. A leave-one-out approach was used: for each subject, the classifier was trained on the data of all other subjects. The training data included all manually annotated PVS points dilated by one voxel in all directions (resulting in a 3×3×3 window), and a random sample of 10% of all white matter voxels within the slab as background class. K was set at 51 and the nearest neighbors were weighted by the inverse of their distance. Local non-maximum suppression was applied to create seedpoints and all locations having a PVS probability above 0.50 were used in a bidirectional 3D tubular tracking algorithm (radius range: 0.15 - 0.70 mm; search depth: 3 steps, 2 angles, pruning threshold of 5; and a termination threshold of 10) (*25*). PVS tracking was performed within the WM in the entire CSO. The length and other parameters of each PVS track were determined using the skeleton of

each individually tracked PVS. The resulting PVS tracks shorter than 2 mm were considered false positives and tracks longer than 50 mm were considered to be physiologically unfeasible, and were therefore excluded. The source code for the automatic PVS detection and tracking was made publicly available online.

For each subject the PVS count was determined. Furthermore, for each tracked PVS the PVS length and tortuosity τ ($\tau = L/C$, with L the PVS length, and C the shortest distance between the begin- and endpoints of the PVS) were determined.

Validation metrics

To validate the automatic PVS detection method, the Intraclass Correlation Coefficient (ICC) and the Dice Similarity Coefficient (DSC) metrics were used. The data used in this work was acquired with 7T MRI, which results in a much larger number of visible PVS compared with data acquired with e.g. 3T MRI. This introduces a bias in the ICC, with higher ICC for a larger PVS count, as the ICC is a data-dependent metric (*26*). The DSC takes also the PVS location into account, additionally to the PVS count, and is therefore regarded as a more reliable metric. However, the DSC value is generally (much) lower than the ICC value for rating highly-frequent noisy objects (*26*).

To compare the performance of the automatic method with manual PVS counting, PVS detection was performed in the exact same slice as manually selected by Bouvy *et al.* (*12*), in the right hemisphere. The automatically tracked PVS and the available manual PVS annotations in this slice were compared based on count and location, using the ICC and the DSC. This was compared with the available inter-observer ICC and DSC for the UDES2 data, between the first and second observer (*12*). Furthermore, the ICC between the automatically detected PVS in the slice used by the first observer and the automatically positioned plane was determined, as a measure of the dependency of the PVS count on the chosen scan section.

Additional quantitative PVS features

The subject images were registered to the MNI-152 brain template (*27*, *28*). The registration method is described by Biesbroek *et al.* (*29*), and is also effective for scans of older subjects. The resulting transformation was applied to the 3D tracked PVS. The PVS density, length, and tortuosity distributions were plotted on top of the MNI-152 brain template. PVS density is computed as the average number of 3D tracked PVS points (resulting from the tubular tracking algorithm) within a 2 mm radius around each voxel in the MNI-152 brain template. Each individual transformed PVS skeleton in MNI-152 space was dilated by 2 mm, and its length and tortuosity were averaged with all other PVS tracks of all subjects in that area.

Results

Figure 2AB shows the T_2-weighted TSE image of one subject in the middle slice of the CSO-slab, and the same image after vesselness filtering. **Figure 2CD** shows the PVS probability map resulting from the kNN classifier, and the detected PVS relative

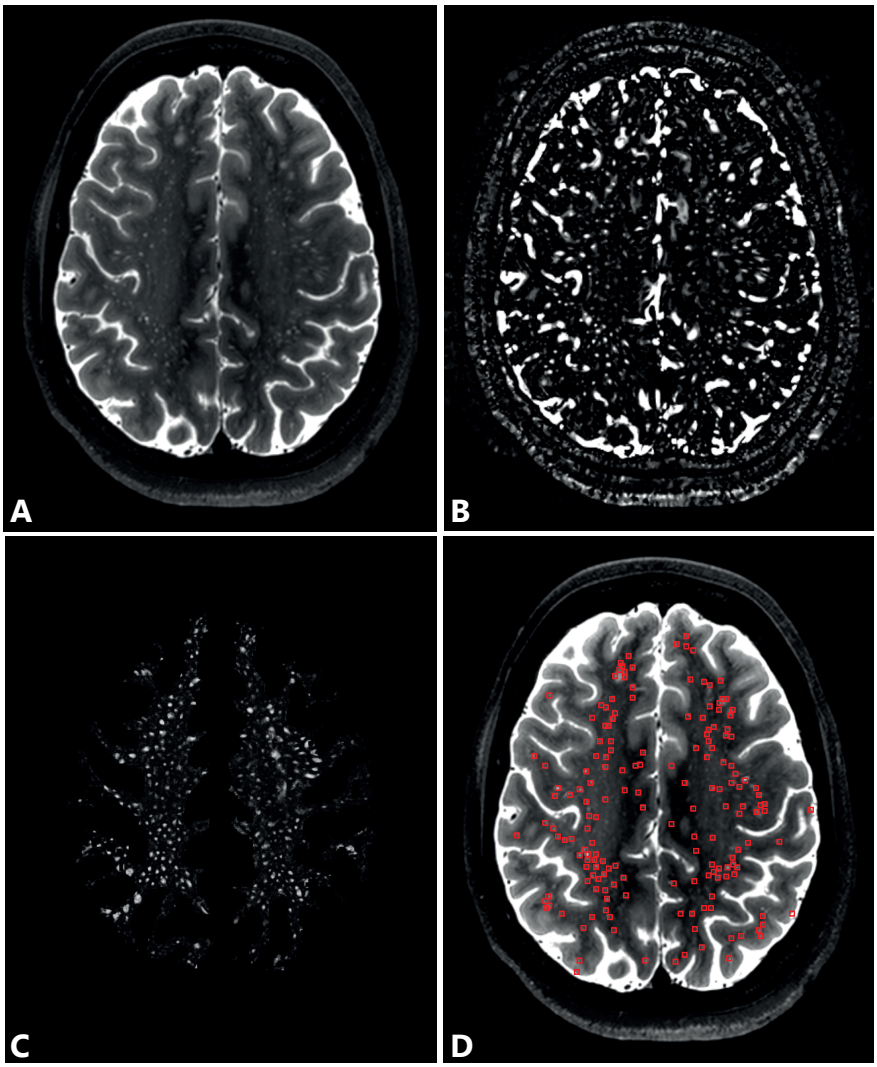

Figure 2 The automatically determined CSO plane from the 3D T_2-weighted TSE volume (A), the vesselness filtered scan (B), the PVS probability map (C), and the detected PVS relative to the T_2-weighted TSE image (D). The PVS detection was performed by thresholding the probability map (threshold = 50%).

to the original T_2-weighted TSE image. For the same subject the 3D tracked PVS are shown relative to a maximum intensity projection (MIP) of a sagittal slab of the T_2-weighted TSE scan (**Figure 3**).

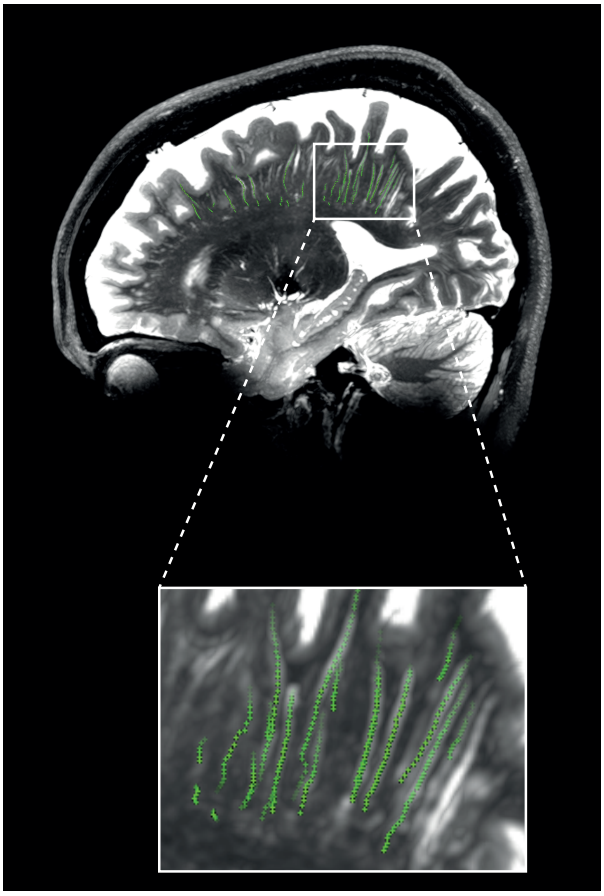

Figure 3 Sagittal view of the tracked PVS (green markers), relative to a maximum intensity projection (MIP) of a sagittal slab (thickness 4 slices) of the 3D T_2-weighted TSE images of a subject.

Validation of automatic PVS detection

To assess the performance of the automatic PVS detection method, the correlation between the number of automatically detected PVS and the number of manually annotated PVS was determined for all 50 subjects. This was done in the exact same slice that was used by the human observer, in the right hemisphere (the left hemisphere was not taken into account by Bouvy *et al.* (*12*)). **Figure 4** shows a scatter

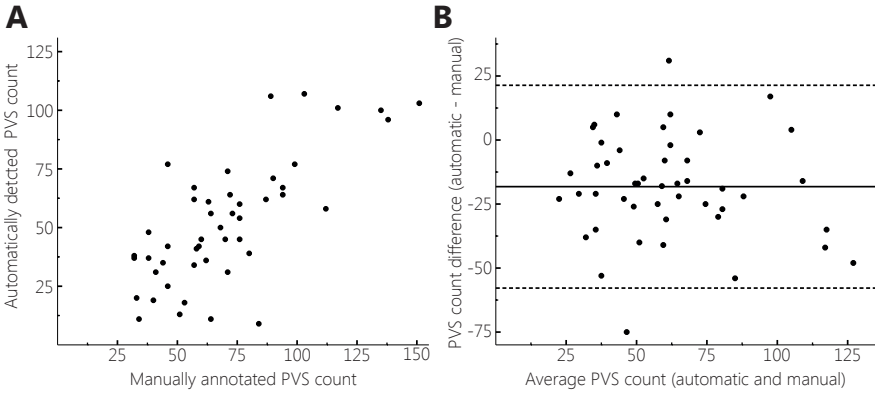

Figure 4 Scatterplot (A) and Bland-Altman plot (B) of the PVS count detected by the automatic method and the PVS count annotated by the human observer, in the slice that was used by the human observer, in the right hemisphere. Overall, the automatic method detected less PVS than the human observer.

plot and a Bland-Altman plot of the PVS counts detected by the automatic method and the human observer. Overall, a smaller PVS count was found by the automatic method compared with the human observer. This can be partially contributed to the fact that the automatic method ignores the smallest PVS (length <2 mm). The ICC (absolute/consistency) was 0.64/0.75, and the DSC was 0.61 between the automatically detected PVS and the manually annotated PVS. In the scans of two subjects artifacts were observed. Despite the artifacts, the method performed relatively well, although the correlation with the visual observers was below average for these two subjects.

To compare the performance of the automatic method with the performance of manual PVS annotation, correlation of the manually annotated PVS with a second human observer was determined. For 20 subjects manually annotated PVS of the second observer were available (*12*). Inter-observer ICC (absolute/consistency) between the original observer and the second observer was 0.85/0.88. However, DSC could not be determined in 16/20 subjects, as different slices were selected by both observers: on average, the distance between the slices was 1.33±0.98 mm (range: 0.34 – 4.17 mm). In four subjects both observers actually annotated the same slice. In these four subjects, the DSC was 0.49 (range 0.32 – 0.73) for the manual PVS annotations between the first and second observer. In these same four subjects, higher DSC was found for the automatic method, compared with both human observers: between the automatically detected PVS and the manually annotated PVS by the first/second observer for these four subjects, DSC was 0.64/0.62 (range 0.59 – 0.75 / 0.55 – 0.73).

Finally, as a measure for the dependency of the PVS count on the chosen scan section, the number of automatically detected PVS was compared between the slice that was used by the human observer and the automatically positioned plane. This resulted in ICC (absolute/consistency) of 0.74/0.74.

Additional quantitative PVS features

Figure 5 shows the average distribution of PVS density relative to the MNI-152 atlas. In both hemispheres two foci of high PVS density can be observed, anterior and posterior in the CSO-slab. **Figure 6** shows the average distribution of PVS length in MNI space; the color indicates the PVS length, and the transparency indicates the number of subjects. Longer PVS can be observed posterior in the CSO, and shorter PVS can be observed anterior in the CSO. Anterior in the CSO, higher PVS lengths are plotted in the most caudal slices compared with more cranial slices: only the longest PVS that were detected in the CSO-ROI, are located in the most caudal slices, whereas more cranially also the shorter PVS are found. **Figure 7** shows the average distribution of the PVS tortuosity relative to the MNI atlas; the color indicates the PVS tortuosity, and transparency indicates the number of subjects. Higher PVS tortuosity can be observed in the center of the CSO, and smallest PVS tortuosity can be observed at the periphery of the CSO. **Figure 8** shows the average and 95% confidence interval (95% CI) distributions of the PVS length and tortuosity, for the tracked PVS of all subjects.

Figure 5 Average distribution of PVS density of all subjects, plotted in MNI space. Very similar PVS densities can be observed in both hemispheres, with two foci with high PVS density anterior and posterior in the CSO.

Figure 6 Distribution of PVS length of all subjects, plotted in MNI space. The markers were dilated to a diameter of 2 mm. The marker color indicates the PVS length; marker transparency indicates the number of PVS markers. Largest PVS lengths can be observed posterior in the CSO, shorter PVS lengths can be observed anterior in the CSO.

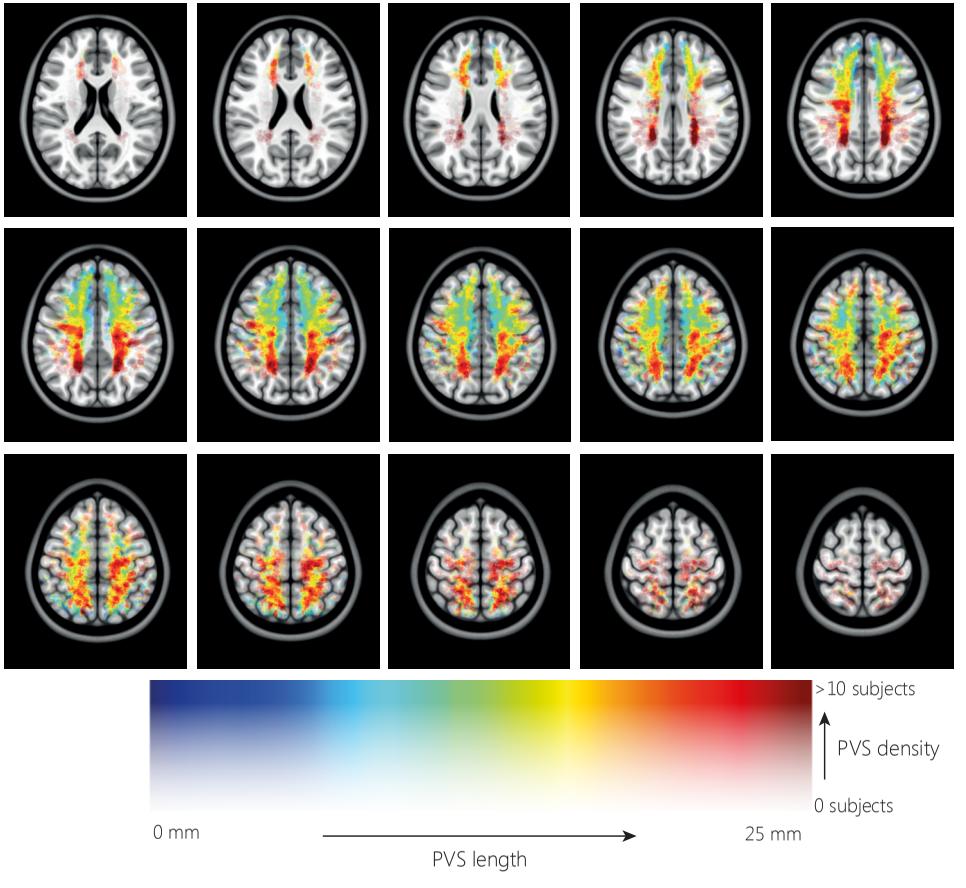

Figure 7 Distribution of PVS tortuosity of all subjects, plotted in MNI space. The markers were dilated to a diameter of 2 mm. The marker color indicates the PVS tortuosity; marker transparency indicates the number of PVS markers. Higher PVS tortuosity can be observed in the center of the CSO, and smallest PVS tortuosity can be observed at the periphery of the CSO and posterior in the CSO.

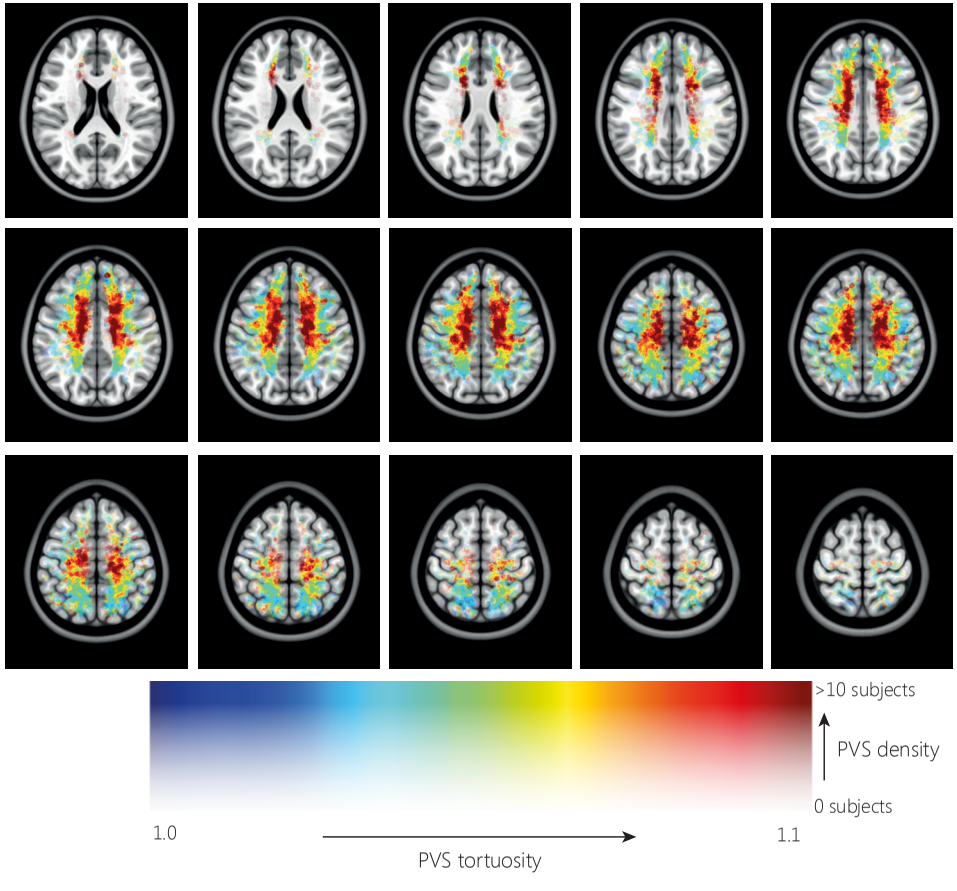

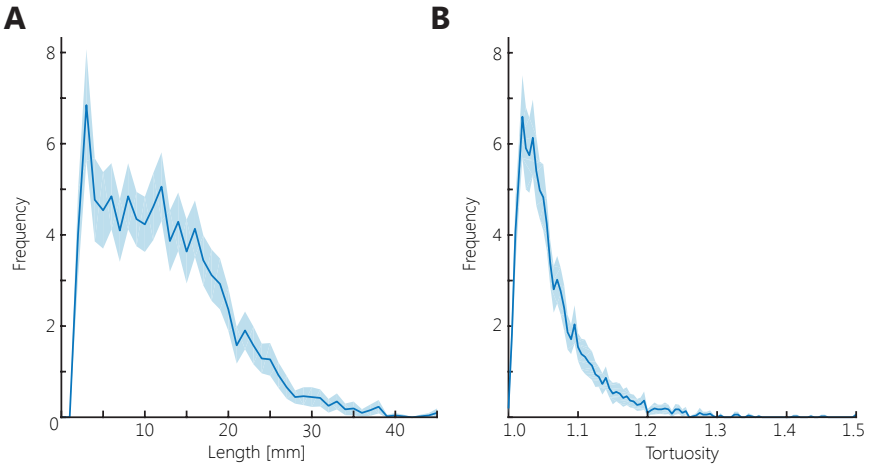

Figure 8 The PVS length (A) and tortuosity distribution (B) for the tracked PVS of all subjects. The line represents the average distribution, the transparent band represents the 95% confidence interval. Median PVS length is 12.1 mm (range: 2 – 48 mm), the median of PVS tortuosity is 1.05 (range: 1.00 – 1.54).

Discussion

In this work a method was developed to automatically detect and quantify PVS in the centrum semiovale. 3D T_2-weighted TSE images acquired at 7T were used as input for the method. The method yields PVS measurements in an automatically detected ROI in the CSO, including count, length, and tortuosity.

The main strength of this fully-automatic method is that it is deterministic, meaning that rerunning the method yields exactly the same results. This increases the repeatability and reproducibility compared with manual PVS assessment. Also, the vesselness filter that was used in this method is independent of possible signal inhomogeneities. Therefore, possible variations in signal intensities (and thus SNR) between regions only have a limited effect on the performance of the method.

Furthermore, additionally to the PVS count, quantitative parameters (length and tortuosity) could be acquired for each PVS by performing 3D tracking of the detected PVS. Also, the large dataset enabled mapping of the quantitative parameters (PVS density, length, and tortuosity) to MNI space.

Finally, a large dataset of high-resolution scans acquired at 7T of 50 subjects with manually annotated PVS was available for this work. This dataset enabled good validation of the automatic PVS detection method.

Our results support the hypothesis that automatic PVS detection is less sensitive to noise and/or motion compared with manual PVS annotation. Our automatic method detects the larger, well-visible PVS and ignores the smallest PVS close to the noise-level, by taking the signal intensity into account along with the vesselness value, and by applying a length restriction on the detected and tracked PVS (PVS must be at least 2 mm in length). These conditions decreased the sensitivity for noise and/or motion in the scan, and therefore resulted in a lower automatically detected PVS count compared with the manual annotated PVS. Also, the manual annotations, that were available from a previous study (*12*), included as many PVS as possible, including the smallest PVS. As a result, the automatic method systematically detected a smaller number of PVS compared with the original manual segmentation (**Figure 4**). This is also likely to contribute to the lower absolute versus consistency ICC between the automatically detected PVS count and the manually annotated PVS. On the other hand, in the four subjects where inter-observer DSC could be determined, DSC was higher for the automatic method compared with the human observers.

The performance of the automatic PVS detection method is on par with what can be expected for this specific task, i.e. counting highly-frequent and inherently noisy objects in 7T images. Only a fraction of all PVS is sufficiently large to be distinguishable above the noise level (*6*, *12*). This yields an inherently ill-defined difference between detectable and non-detectable PVS. Visual (and automatic) PVS rating is still possible, but a consistent method to annotate the PVS is necessary. Individual human observers have different intrinsic cut-offs for annotating an object as PVS or ignoring it as noise. Training of observers can decrease the difference between these intrinsic cut-offs, but inter-observer differences remain. Paradoxically, these inter-observer differences are amplified in 7T scans, due to the significantly higher visibility of PVS on 7T MRI compared with 1.5T or 3T. If fewer and larger PVS are visible (e.g. on 3T MR images), the likelihood that both observers will identify the same objects is higher. On 7T MRI images, much more and smaller PVS (and PVS-like objects) are visible, which decreases the inter-observer agreement. This is not related to the performance of the observers (human or machine), but can be fully attributed to the increased difficulty of rating 7T MR images. This was demonstrated earlier for rating cerebral microbleeds by Kuijf *et al.* (*26*): in this work it was shown that the difference between the ICC and DSC increases for increasing object counts.

Our human observers had an inter-observer ICC of 0.85/0.88 for the PVS count, which can be qualified as "good". However, when considering the overlap between the annotations, the DSC is only 0.49. Thus, the human observers agreed on the PVS count, but did not necessarily identify the same PVS. This demonstrates the difficulty in rating highly-frequent noisy objects on 7T MR images: it is hard to consistently identify the same object in an image. The DSC between the automatic method and the human observers was larger than the inter-observer DSC. This illustrates that the agreement between the method and either observer is larger than the inter-observer agreement.

Recently, several automatic methods for (semi-)automatic PVS segmentation have been proposed by different groups currently working on automatic PVS detection (*30*–*36*). For the automatic PVS detection and tracking method that was proposed in this work a low-resolution T_1-weighted scan (to determine the WM mask) and a high-resolution T_2-weighted TSE scan (for PVS segmentation) were used as input, with a total scan time of approximately 12 minutes. This scan time is relatively short compared with other automatic PVS detection methods. For example, Park *et al.* (*31*) used two high-resolution (T_1- and T_2-weighted) scans acquired at 7T, with a total scan time of approximately 22 minutes.

Our automatic PVS detection method resulted in similar or higher correlation with human observers, compared with other automatic detection methods. Boespflug *et al.* (*33*) used a PVS detection method based on signal intensities in T_1-weighted, fluid-attenuated inversion recovery, T_2-weighted, and proton density data (acquired at 3T), and filtered the detected PVS based on multiple morphological features (width, volume, and linearity). In contrast, in our method included a morphological feature (vesselness) in the detection step, thereby eliminating the need for extensive filtering after PVS detection. Boespflug *et al.* tested their method in a dataset of 14 subjects (age ranging between 70 – 101 years), and achieved correlation R of 0.54 – 0.69, relative to three raters. In our study R was 0.76 compared with the manually annotated PVS. Park *et al.* used a learning-approach method for PVS detection, and Lian *et al.* (*32*) used a fully convolutional neural network approach. Both methods used extensive image filtering: Park *et al.* used randomized 3D Haar features, and Lian *et al.* incorporated enhancement of the used MRI images using a non-local Haar-transform-based method, which was introduced by Hou *et al.* (*37*). In contrast, in our work a more simple method based on vesselness value and signal intensity was used. Both Park *et al.* and Lian *et al.* compared their automatic methods with a ground truth that was determined semi-automatically, in subsets of 11 and 14 subjects, respectively. Both methods resulted in relatively high correlation relative

to the ground truth, with DSC slightly above 0.7. This is higher than the DSC of 0.61 found in our work, which was derived from a dataset of 50 subjects. However, in our work the automatic method was compared with manually annotated PVS, including very small PVS, which were excluded from the ground truths used by Park *et al.* and Lian *et al.*. Also, Park *et al.* used young, healthy volunteers (age ranging between 25 – 37 years) and detected on average 298 PVS in the whole brain, whereas in this study also elderly subjects were included with higher PVS density (on average 106 PVS were detected in only one slice). Furthermore, the scans used in our work occasionally showed motion, which potentially decreased the overall correlation with the manually counted PVS.

In work by Hou *et al.* (*37*) 7T MRI scans were enhanced using a method based on the Haar transform, which increased the distinguishability of PVS. Hou *et al.* showed that PVS detection by thresholding the scans after vesselness filtering was significantly improved by using the enhanced and denoised scans. In our work a combination of the vesselness filter with signal intensities in the T_2-weighted scan was used for PVS detection. Incorporating Hou's scan enhancement in our automatic method may offer possibilities to further improve both detection and tracking of PVS. However, in our method only larger PVS were included (PVS shorter than 2 mm are excluded), and therefore the scan enhancement by Hou *et al.* is expected to offer only minor improvements for our PVS detection method.

The method presented in this work was developed for PVS detection in a 2D slab, similar to commonly used visual rating scales (*9–11*), which enabled thorough validation using the manually annotated PVS. This is contrary to several other published (semi-)automatic methods (*30–35*) where PVS segmentation is performed in the entire brain or within certain brain regions (centrum semiovale and basal ganglia). The comparison between the PVS count in the automatically determined CSO-ROI in this work and the slice used by the first observer in Bouvy *et al.*, resulted in ICC of 0.74. This is in line with literature, where lower correlation was found between observers when different slices were used (*35*), and relatively low correlation was observed between PVS count in a single slice and in the whole brain (*30*). Automatic slice selection, as was performed in our method, can reduce PVS count variation induced by the selected slice. However, whole-brain PVS segmentation or PVS segmentation for 3D brain regions may offer the most reliable PVS count. Therefore we aim to extend our method to a full 3D assessment in future work.

The spatial differences in PVS density, length, and tortuosity observed in this work may be related to the relatively high age of subjects in this study. Contrary to our results, Park *et al.* (*31*), found similar PVS lengths in the parietal-occipital lobe and the frontal lobe, and slightly shorter PVS in the temporal lobe, in younger subjects (25 – 37 years). Also, Park *et al.* found shorter PVS, up to 18 mm, compared with the PVS lengths acquired in our work. This may suggest that, in aging subjects, PVS posterior in the CSO increase in length before PVS in other regions of the CSO. It would be very interesting to further investigate such regional differences in PVS properties in relation to age and between different diseases. Furthermore, Feldman *et al.* (*13*) have recently found asymmetry in PVS count in epilepsy patients; possibly also asymmetry in PVS length and/or tortuosity can be found in diseases such as epilepsy.

In contrast to Park *et al.* (*31*), Boespflug *et al.* (*33*), Ramirez *et al.* (*30*), and Cai *et al.* (*34*), PVS diameter and volume were not determined in this work, which could be regarded as a limitation. However, the measured PVS diameter can be expected to depend strongly on the acquired resolution. Moreover, reliable diameter estimates require more than a single voxel within the PVS, limiting measurements to only the largest diameters >1 mm (*38*). Due to the small PVS diameter (normally less than 2 mm in healthy subjects) relative to the acquired isotropic resolution of 0.7 mm, estimates of PVS diameter and volume will certainly suffer from considerable errors and partial volume effects.

The main limitation of this work is that the method is currently not able to perform 3D detection. However, using a 2D slab enabled good validation with manual PVS assessment. In future work our automatic PVS detection method can be extended to a full-brain PVS detection method.

Also, manual PVS markers were used to train the method. These markers included the very small PVS, which may not be reproducible, and is expected to increase the risk of selecting false positives. To minimize the number of false positive detected PVS, a minimum PVS length of 2 mm after tracking was used, but false positive detected PVS cannot be prevented entirely.

Furthermore, occasionally a (long) in-plane perivascular space was detected more than once. Tracking of these detected points can result in multiple short PVS, rather than one long PVS track, thereby resulting in underestimated (average) PVS length. In the slices used for PVS detection in this work (almost) all PVS were almost perpendicular to the plane. Therefore the effect of in-plane PVS was very limited. Merging of the identified PVS pixels may resolve this issue for extending our method to whole-brain PVS detection.

Finally, despite the high resolution of the scans used in this work, many small PVS cannot be detected due to their small size. Therefore, quantitative PVS measurements could only be performed for larger PVS. As PVS diameters range down to the micrometer scale (*39*), this will remain a challenge for all PVS detection methods that are based on anatomical images.

Conclusion

In this work we present a fully automatic method to detect PVS in a 2D slab in the CSO, and to extract quantitative PVS parameters by performing 3D tracking of the detected PVS. Our method shows good correlation with manual PVS assessment and has the potential to quantitatively study PVS characteristics such as density, length and tortuosity in aging and disease.

References

1. R. M. Kwee, T. C. Kwee, Virchow-Robin spaces at MR Imaging. *RadioGraphics.* 27, 1071–1086 (2007).
2. J. J. Iliff *et al.*, Cerebral arterial pulsation drives paravascular CSF-interstitial fluid exchange in the murine brain. *J Neurosci.* 33, 18190–18199 (2013).
3. N. J. Abbott, Evidence for bulk flow of brain interstitial fluid: significance for physiology and pathology. *Neurochem Int.* 45, 545–552 (2004).
4. C. Moran, T. G. Phan, V. K. Srikanth, Cerebral small vessel disease : a review of clinical , radiological , and histopathological phenotypes. *Int. J. Alzheimers. Dis.* 7, 36–46 (2012).
5. C. L. Satizabal, Y. C. Zhu, C. Dufouil, C. Tzourio, Inflammatory proteins and the severity of dilated Virchow-Robin spaces in the elderly. *J. Alzheimer's Dis.* 33, 323–328 (2013).
6. J. M. Wardlaw *et al.*, Neuroimaging standards for research into small vessel disease and its contribution to ageing and neurodegeneration. *Lancet Neurol.* 12, 822–838 (2013).
7. J. Ramirez *et al.*, Imaging the perivascular space as a potential biomarker of neurovascular and neurodegenerative diseases *Cell. Mol. Neurobiol.* 36, 289–299 (2016).
8. G. Banerjee *et al.*, MRI-visible perivascular space location is associated with Alzheimer's disease independently of amyloid burden. *Brain.* 140, 1107–1116 (2017).
9. G. M. Potter, F. M. Chappell, Z. Morris, J. M. Wardlaw, Cerebral perivascular spaces visible on magnetic resonance imaging: Development of a qualitative rating scale and its observer reliability. *Cerebrovasc. Dis.* 39, 224–231 (2015).
10. H. H. H. Adams *et al.*, Rating Method for Dilated Virchow - Robin Spaces on Magnetic Resonance Imaging. *Stroke.* 44, 1732–1735 (2013).
11. T. F. Patankar *et al.*, Dilatation of the Virchow-Robin Space Is a Sensitive Indicator of Cerebral Microvascular Disease : Study in Elderly Patients with Dementia, *Am J Neuroradiol. 26*,1512–1520 (2005).
12. W. H. Bouvy *et al.*, Perivascular spaces on 7 Tesla brain MRI are related to markers of small vessel disease but not to age or cardiovascular risk factors. *JCBFM.* 36, 1708–1717 (2016).
13. R. E. Feldman *et al.*, Quantification of perivascular spaces at 7 T : A potential MRI biomarker for epilepsy. *Seizure.* 54, 11–18 (2018).
14. L. E. M. Wisse *et al.*, Subfields of the hippocampal formation at 7T MRI: In vivo volumetric assessment. *Neuroimage.* 61, 1043–1049 (2012).
15. Y. D. Reijmer *et al.*, Microstructural white matter abnormalities and cognitive functioning in type 2 diabetes: A diffusion tensor imaging study. *Diabetes Care.* 36, 137–144 (2013).
16. J. Ashburner, K. J. Friston, Unified segmentation. *Neuroimage.* 26, 839–851 (2005).
17. S. Klein, M. Staring, K. Murphy, M. A. Viergever, J. Pluim, elastix: A toolbox for intensity-based medical image registration. IEEE Trans. *Med. Imaging.* 29, 196–205 (2010).
18. Y. Sato *et al.*, Three-dimensional multi-scale line filter for segmentation and visualization of curvilinear structures in medical images. *Med. Image Anal.* 2, 143–168 (1998).
19. A. F. Frangi, W. J. Niessen, K. L. Vincken, M. A. Viergever, in Medical Image Computing and Computer-Assisted Interventation—*MICCAI'98* (1998), pp. 130–137.
20. MeVisLab Vesselness (2018), (available at http://mevislabdownloads.mevis.de/docs/current/FMEsTable/ReleaseMeVis/Documentation/Publish/ModuleReference/Vesselness.html).
21. H. J. Kuijf, A. Leemans, M. A. Viergever, K. L. Vincken, Assessment of methods to extract the mid-sagittal plane from brain MR images. *Proc. SPIE 8673, Med. Imaging* 2013: *Image Perception, Obs. Performance, Technol. Assess*., 86731K (2013).

22. I. Volkau *et al.*, Extraction of the midsagittal plane from morphological neuroimages using the Kullback–Leibler's measure. *Med. Image Anal.* 10, 863–874 (2006).

23. H. J. Kuijf *et al.*, Quantification of deep medullary veins at 7 T brain MRI. *Eur. Radiol.* 26, 3412–3418 (2016).

24. F. Pedregosa *et al.*, Scikit-learn: Machine Learning in Python. *J. Mach. Learn. Res.* 12, 2825–2830 (2012).

25. O. Friman, M. Hindennach, C. Kühnel, H. O. Peitgen, Multiple hypothesis template tracking of small 3D vessel structures. *Med. Image Anal.* 14, 160–171 (2010).

26. H. J. Kuijf, S. J. van Veluw, M. A. Viergever, K. L. Vincken, G. J. Biessels, How to assess the reliability of cerebral microbleed rating? *Hugo. Front. Aging Neurosci.* 5, 1–2 (2013).

27. V. Fonov, A. Evans, R. McKinstry, C. Almli, D. Collins, Unbiased nonlinear average age-appropriate brain templates from birth to adulthood. *Neuroimage.* 47, S102 (2009).

28. V. Fonov *et al.*, Unbiased average age-appropriate atlases for pediatric studies. *Neuroimage.* 54, 313–327 (2011).

29. J. M. Biesbroek *et al.*, Association between subcortical vascular lesion location and cognition: a voxel-based and tract-based lesion-symptom mapping study. The SMART-MR study. The SMART-MR Study. *PLoS One.* 8 (2013), doi:10.1371/journal.pone.0060541.

30. J. Ramirez *et al.*, Visible Virchow-Robin spaces on magnetic resonance imaging of Alzheimer's disease patients and normal elderly from the Sunnybrook dementia study. *J. Alzheimer's Dis.* 43, 415–424 (2015).

31. S. H. Park, X. Zong, Y. Gao, W. Lin, D. Shen, Segmentation of perivascular spaces in 7 T MR image using auto-context model with orientation-normalized features. *Neuroimage.* 134, 223–235 (2016).

32. C. Lian *et al.*, Multi-channel multi-scale fully convolutional network for 3D perivascular spaces segmentation in 7T MR images. Med. *Image Anal.* (2018), doi:10.1016/j.media.2018.02.009.

33. E. L. Boespflug *et al.*, MR imaging-based multimodal autoidentification of perivascular spaces (mmaps): automated morphologic segmentation of enlarged perivascular spaces at clinical field. *Radiology* 286, 632-642 (2018).

34. K. Cai *et al.*, The feasibility of quantitative MRI of perivascular spaces at 7T. J. *Neurosci. Methods*. 256, 151–156 (2015).

35. X. Wang *et al.*, Development and initial evaluation of a semi-automatic approach to assess perivascular spaces on conventional magnetic resonance images. *J. Neurosci. Methods.* 257, 34–44 (2016).

36. L. Ballerini *et al.*, Perivascular spaces segmentation in brain MRI using optimal 3D filtering. *Sci. Rep*. 8 (2018), doi:10.1038/s41598-018-19781-5.

37. Y. Hou *et al.*, Enhancement of perivascular spaces in 7 T MR image using Haar transform of non-local cubes and block-matching filtering. *Sci. Rep.* 7, 8569 (2017).

38. W. H. Bouvy *et al.*, Visualization of perivascular spaces and perforating arteries with 7 T magnetic resonance imaging. *Invest. Radiol.* 49, 307–313 (2014).

39. M. Marín-Padilla, D. S. Knopman, Developmental aspects of the intracerebral microvasculature and perivascular spaces: insights into brain response to late life diseases. *J. Neuropathol. Exp. Neurol*. 70, 1060–1069 (2011).

Chapter 3

Assessing the perivascular spaces count using texture features in 3T MRI scans: a feasibility study

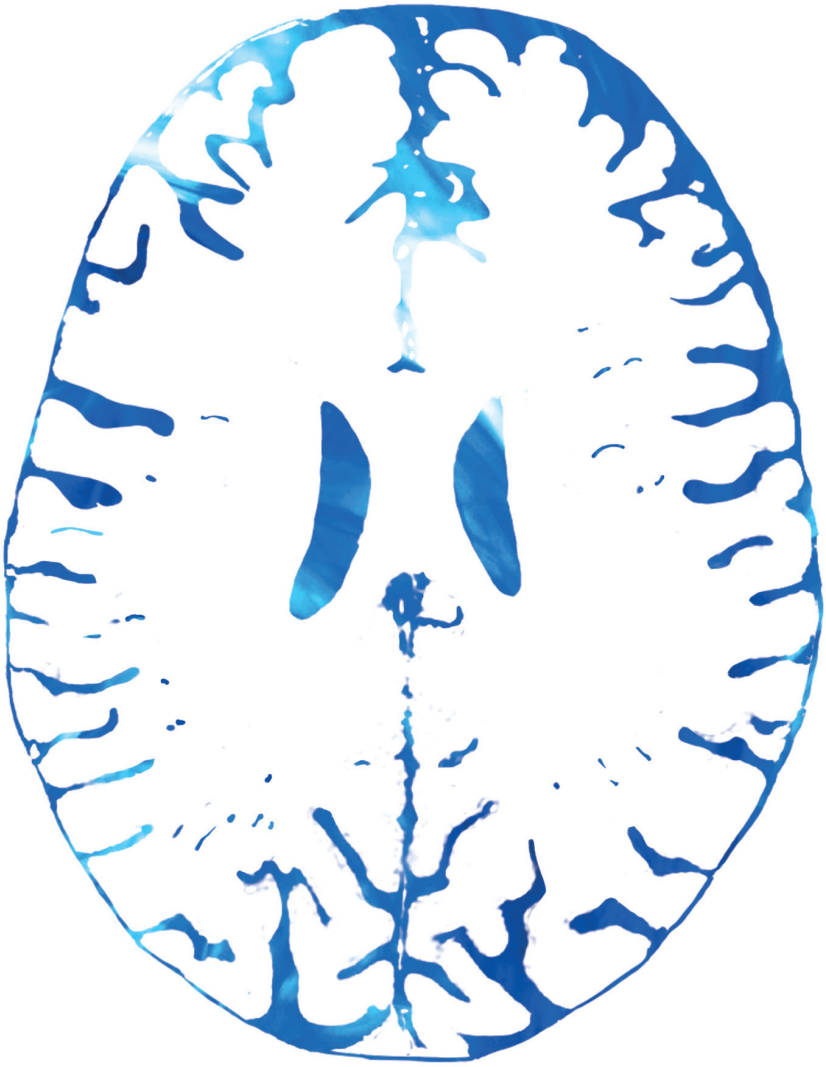

Jolanda M. Spijkerman, Bas H.M. van der Velden, Geert-Jan Biessels, Jeroen Hendrikse, Peter R. Luijten, Jaco J.M. Zwanenburg, Hugo J. Kuijf

In preparation

Abstract

Objective

At 7T MRI many more perivascular spaces are observed compared to 3T MRI, but 7T MRI is not yet widely available. The perivascular spaces count in low-resolution 3T scans was hypothesized to be a poor predictor for the perivascular spaces count in high-resolution 7T scans. Therefore, the feasibility of using texture features in the 3T scans as predictor for the high-resolution perivascular spaces count was explored. Furthermore, texture features in 3T scans were hypothesized to show better correlation with the perivascular spaces count in 7T scans than with the count in 3T scans.

Methods

Perivascular spaces were annotated automatically in a plane in the centrum semiovale in T_2-weighted 7T scans (resolution: 0.7×0.7×0.7 mm^3). T_2-weighted 3T scans (resolution: 1×1×3 mm^3) were used for manual perivascular spaces annotation in a single slice, and to determine texture features based on the co-occurrence matrix. Correlation between the low- and high-resolution counts was assessed using the Intraclass Correlation Coefficient; correlation between the high-resolution perivascular spaces count and the texture features was assessed using a least absolute shrinkage and selection operator regression analysis.

Results

The perivascular spaces count was 19±8 (mean ± standard deviation) at 3T, and 111±40 at 7T. Intraclass Correlation Coefficient between the low- and high-resolution counts was 0.14. The regression analysis showed no significant correlation between the texture features and perivascular spaces counts, neither on 3T nor 7T.

Conclusion

No correlations were found between the perivascular spaces counts at 3T and 7T, and between the perivascular spaces counts and the texture features in the low-resolution scans. Thus, currently the perivascular spaces count in high-resolution scans acquired at 7T MRI cannot be estimated using 3T scans.

Introduction

Perivascular spaces (PVS), or Virchow-Robin spaces, are fluid-filled spaces around the brain penetrating blood vessels (*1*), and are connected to the CSF in the subarachnoid space. The perivascular spaces play an important physiological role: they probably enable exchange between CSF and interstitial fluid (*2*), and are associated with brain clearance (*2–5*). Therefore, PVS are likely necessary for maintaining homeostasis in the brain (*6*). There is a wide range of PVS sizes, with the majority of the PVS having sub-millimeter diameters (*7*). The largest perivascular spaces in young, healthy subjects have a diameter of approximately 2 - 3 mm (*7*, *8*). The appearance of more and/or larger perivascular spaces is a feature of cerebral Small Vessel Disease (SVD) (*7*, *9*, *10*), and an asymmetrical PVS count between the two brain hemispheres has been linked with epilepsy (*11*). PVS are thus a highly relevant metric for investigating the healthy and diseased brain.

PVS can be observed in MR images, where they appear with a (visually) similar signal intensity as CSF (*1*). In clinical 3T MRI scans generally only the largest PVS can be observed. The PVS load can be assessed more extensively in high-resolution scans acquired using 7T MRI, as also smaller PVS are visible in these scans. The PVS count in these high-resolution scans correlates with SVD features and not with age (*8*), contrary to the PVS count in low-resolution scans (*12–14*). This suggests that the PVS count in high-resolution scans is more (clinically) relevant than the PVS count in low-resolution scans. However, 7T MRI is not (yet) widely available. As a result, in most large-scale (clinical) studies it is not feasible to obtain a good measure of the PVS count in high-resolution scans. Thus, a more complete measure of the PVS load using lower-resolution scans acquired at a lower field strength, such as 3T, would be very relevant.

The PVS count in 7T images is expected to be more representative for the total PVS load than the PVS count in 3T images, and the PVS count in 3T images may not be suitable as a predictor for the PVS count in 7T images. On the other hand, image texture features have the potential to reveal differences between healthy and diseased subjects. For example, De Bresser *et al.* (*15*) found a larger number of non-punctuate white matter hyperintensities (WMH) in diabetes patients compared with healthy controls, and differences in the WMH shape, using shape features of the WMH. Furthermore, Wibmer *et al.* (*16*) showed that cancerous prostate tissue can be distinguished from non-cancerous tissue using Haralick texture features. Due to the higher signal intensity of PVS compared to the brain tissue in MRI images, sub-voxel PVS can subtly alter the signal intensity in a voxel. As a result, the

signal intensity distribution in the white matter can be more irregular in subjects with a larger PVS count when compared to subjects with a smaller PVS count. Since we expect that the PVS count in 7T images is most representative for the total PVS load, we hypothesized that the PVS count in 7T images shows better correlation with texture measures in 3T images than with the PVS count in 3T images.

Methods

Data

Scans of participants from the second Utrecht Diabetic Encephalopathy Study (UDES2) were available for this study (*17*). UDES2 was approved by the medical ethics committee of the University Medical Center Utrecht, and all subjects gave written informed consent. The guidelines of the Declaration of Helsinki of 1975 were followed. The inclusion protocol is described in detail elsewhere (*8*, *17*). Briefly, in the UDES2 study both patients with diabetes mellitus and healthy controls were included. The subjects had no cognitive impairment. For all subjects both a 3T and a 7T dataset were available.

The inclusion criterion for UDES2 subjects in this study was the availability of a T_2-weighted TSE scan in the 7T dataset. This resulted in the inclusion of 32 UDES2 subjects in this study (14 male, 14 diabetic, mean age 69.7 years (range 65.4 – 76.8)). From the 3T dataset a 3D T_1-weighted scan was available, with 1 mm isotropic resolution, and TR/TE 7.9/4.5 ms. Also, a T_2-weighted TSE scan acquired at 3T was available, with 0.96×0.96×3 mm^3 resolution, and TR/TE were 3000/101 ms. The 7T 3D T_2-weighted TSE scan had 0.7 mm isotropic resolution, reconstructed to 0.35 mm isotropic, and a TR/TE of 3158/301 ms. Also, for all subjects a T_1-weighted TFE scan acquired at 7T was available, with 1 mm acquired isotropic resolution, reconstructed to 0.66×0.66×0.5 mm^3, and TR/TE of 4.8/2.2 ms.

After visual inspection of the scans, 4 subjects were excluded due to poor (7T) scan quality caused by motion. Of the 4 excluded subjects, 1 subject had diabetes mellitus. Therefore, the data of 28 subjects (12 male, 13 diabetic, mean age 69.6 years (range 65.4 – 76.8)) was used in this work.

PVS annotation

The high-resolution 7T scans were used for the automatic PVS detection. The automatic PVS detection was performed using an in-house developed method that was designed specifically for PVS detection in high-resolution scans (Chapter 2 (*18*)). This method showed good correlation with PVS annotation by human

observers, with Dice Similarity Coefficient (DSC) of 0.61. In short, the PVS detection method consists of nine steps. 1) Segmentation of the white matter was performed in the T_1-weighted scans, using SPM12 (*19*). 2) The T_1-weighted scans were registered to the T_2-weighted scans with rigid registration, using elastix (*20*). The obtained registration field was then used to register the white matter (WM) mask to the T_2-weighted scans. 3) All vessel-like structures in the T_2-weighted scans, thus including the PVS, were enhanced by vesselness filtering the scan with a multi-scale 3D vesselness filter. A multi-scale 3D vesselness implementation as proposed by Sato *et al.* and implemented in MeVisLab was used (*21–23*). 4) A slab of 7 slices was automatically positioned in the centrum semiovale (CSO), parallel to the line connecting the genu and splenium of the corpus callosum, perpendicular to the midsagittal plane, and 10 mm above the lateral ventricles, as shown in **Figure 1**. 5) The CSO region-of-interest (ROI) was defined as the WM within this slab. 6) The T_1- and T_2-weighted signal intensities and the vesselness values for all voxels within the CSO-ROI were used to determine a PVS-probability map. 7) PVS seedpoints were obtained by thresholding this probability map. 8) The PVS were tracked using bi-directional tubular tracking, with the PVS seedpoints as starting point. 9) The PVS count was determined as all PVS tracks with a length between 2 – 50 mm.

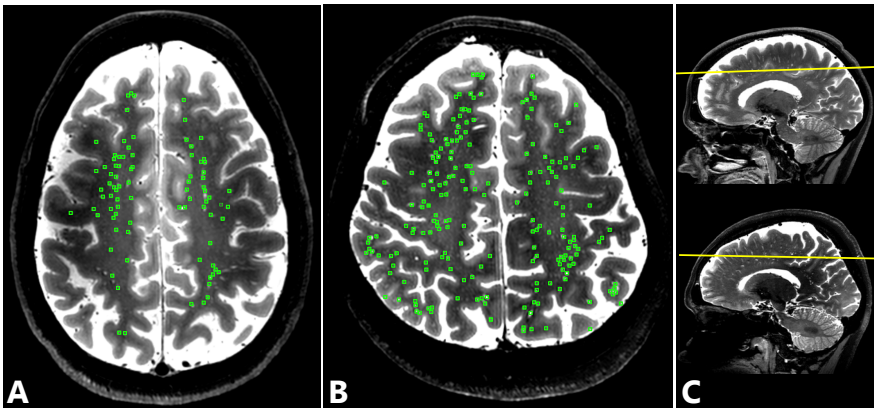

Figure 1 High-resolution T_2-weighted TSE scans acquired at 7T and the automatically annotated PVS (green), for subject 1 with a low PVS count of 73 PVS (A) and for subject 2 with a high PVS count of 178 PVS (B). The automatically determined CSO planes are represented by the yellow line (C; top: subject 1; bottom: subject 2).

The low-resolution scans acquired at 3T were used for manual PVS annotation by a human observer in a single slice. The first slice above the lateral ventricles was used, as shown in **Figure 2**.

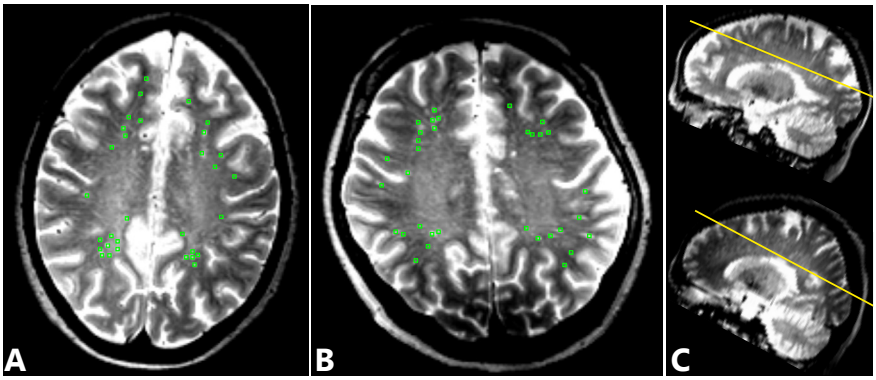

Figure 2 Low-resolution T_2-weighted TSE scans acquired at 3T and the manually annotated PVS (green) for subject 1 (A) and for subject 2 (B). The selected slices are represented by the yellow line (C; top: subject 1; bottom: subject 2). In the 3T scans the PVS counts were 31 and 33 for subjects 1 and 2, respectively. In the 7T scans the PVS counts were 73 and 178 for subjects 1 and 2, respectively.

Texture features

The texture features were determined in the T_2-weighted scans acquired at 3T. Segmentation of the white matter was performed in the T_1-weighted scans, using SPM12 (*19*). The T_1-weighted scans were registered to the T_2-weighted scans with rigid registration, using elastix (*20*). The obtained registration field was then used to register the WM mask to the T_2-weighted scans. Manual segmentations of all white matter lesions were available from previous work (*24*), and were removed from the WM mask. Subsequently, the WM mask was eroded to prevent leaking of texture information outside the masked region.

To determine the texture features, texture filters were applied to the WM in the T_2-weighted scans, using a two-dimensional 5x5 kernel. The used texture features are based on the co-occurrence matrix, as introduced by Haralick (*25*), and are widely used in image analysis and radiomics (*16*, *26*). Thirteen features can be derived from the co-occurrence matrix. The texture feature values were determined for all voxels within the WM mask.

Statistical analysis

The primary goals of this study were to explore if the PVS count in the low-resolution scans (3T) is associated with the PVS count in the high-resolution scans (7T), and to explore if the texture features in the low-resolution scans are associated with the PVS count in the low- and high-resolution scans. To assess the correlation between the low- and high-resolution PVS count the consistency Intraclass Correlation Coefficient (ICC) was determined, and a scatter plot of the low- and high-resolution PVS counts was made. To assess the associations between the texture features and the low- and high-resolution PVS counts, a least absolute shrinkage and selection operator (LASSO) regression analysis (*27*) was performed. To compare texture features with the low-resolution PVS count, the texture features were determined in the same slice that was used for PVS annotation. To compare texture features with the high-resolution PVS count, the texture features were determined over the whole brain, since the plane used for PVS annotation in the 7T scans has a different orientation than the slice orientation of the 3T scans. LASSO analyses were performed for three types of texture feature sets within the WM mask: 1) the average and standard deviations of the texture features, 2) the percentiles of texture features, and 3) the average of the values below and above a given percentile of the texture features. The percentiles were chosen between 10 and 90 in increments of 10. Since it is not a-priori known whether a low or high feature is informative, percentile features were paired according to their relative location on a distribution. Thus, the features of the 10^{th} percentile were added to the 90^{th} percentile, features of the 20^{th} percentile to those of the 80^{th} percentile, and so on. The LASSO analysis was then performed for each percentile pair, thus the correlation between the high-resolution PVS count and e.g. the $10^{th}/90^{th}$ percentiles was determined. Therefore, eleven feature sets were analyzed (one of type 1, five of types 2 and 3).

Several steps were performed to prevent overfitting. First, a dimensionality reduction was performed:, features underwent a principal component analysis with varimax rotation after normalization to a zero mean with a standard deviation of one. The number of selected components was chosen to cumulatively explain 99% of the variance of the original features. Second, the LASSO regularization parameter λ was selected using tenfold cross validation: λ was selected using the 'one standard error rule' (*28*).

For all statistical tests a two-tailed p-value <0.05 was considered significant. Statistical analysis of the PVS counts was performed using IBM SPSS Statistics (version 24). Statistical analysis of the texture features was performed using R 3.5.1 (R Foundation for Statistical Computing, Vienna, Austria).

Results

PVS detection and texture features

The automatically determined PVS count in the high-resolution 7T MRI scans was 111±40 (mean ± standard deviation (SD)). In **Figure 1** the T_2-weighted TSE scans acquired at 7T of a subject with a low PVS count of 73 PVS, and for a subject with a high PVS count of 178 PVS are shown.

The manually determined PVS count in the low-resolution 3T MRI scans was 19±8 (mean±SD). In **Figure 2** the low-resolution T_2-weighted TSE scans acquired at 3T are shown for the same subjects. In these low-resolution scans, the large difference in PVS count that was obtained using the high-resolution scans is not observed and the PVS counts were quite similar: 31 and 33 PVS, respectively. However, the WM structure visually seems slightly more irregular for the subject with the highest PVS count.

In **Figure 3** the resulting texture-filtered images are shown for three texture filters, i.e. the difference entropy, the measure of correlation_1, and the sum entropy filters. The difference entropy and the sum entropy filtered images appear to be higher for the subject with the lowest PVS count, while they appear to be lower for the measure of correlation_1 filter. However, these visual inter-subject differences were not obvious for all subjects and texture-filters.

Associations between PVS counts and texture features

Figure 4 shows the scatter plot of the high- and low-resolution PVS counts at 7T and 3T. The correlation between these PVS counts was poor, with ICC of 0.13 and R^2 of 0.032.

Results of the LASSO analysis are shown for the mean and standard deviation texture feature set. The principal component analysis shows that 99% of the variance is captured by the first eight components. Loadings of the rotated components are shown in **Figure 5**, and indicate the fraction of variance in the original variables that is explained by each component. Using the 'one standard error rule', the LASSO did not select rotated components with respect to the low- and high-resolution PVS counts from any of the feature sets. The cross-validated LASSO shows that at the optimum λ value – and thus, also at the one standard error λ value – no components are selected (**Figure 6**).

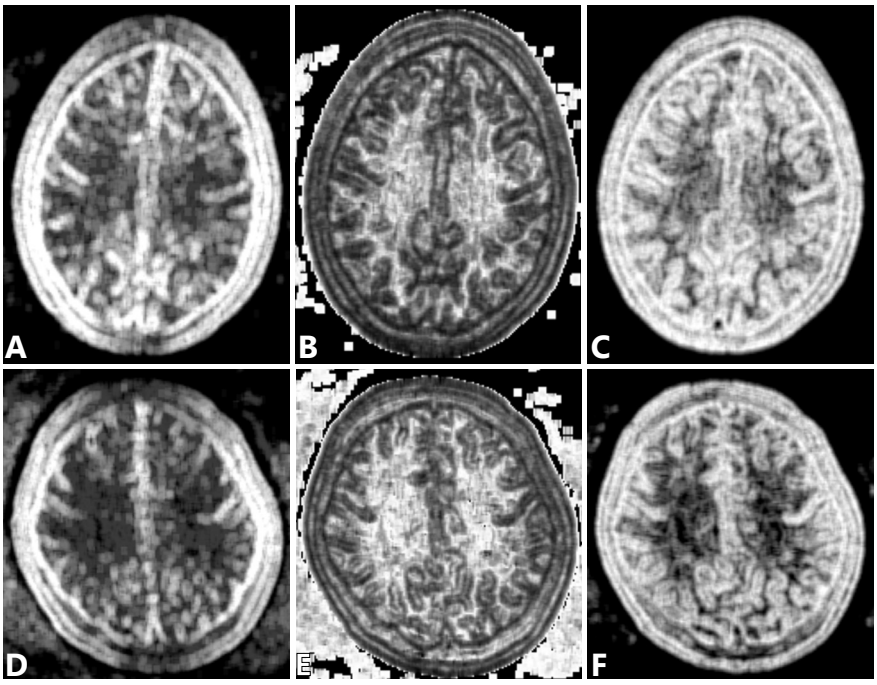

Figure 3 Structure filtered scans for subject 1, with a low PVS count of 73 PVS in the high-resolution scan acquired at 7T (A-B-C) and for subject 2 with a high PVS count of 178 PVS in the high-resolution scan acquired at 7T (D-E-F). The structure filtered images are shown for the difference entropy (A, D), the measures of correlation_1 (B, E), and the sum entropy filters (C, F). Image pairs are scaled equally to allow direct comparison.

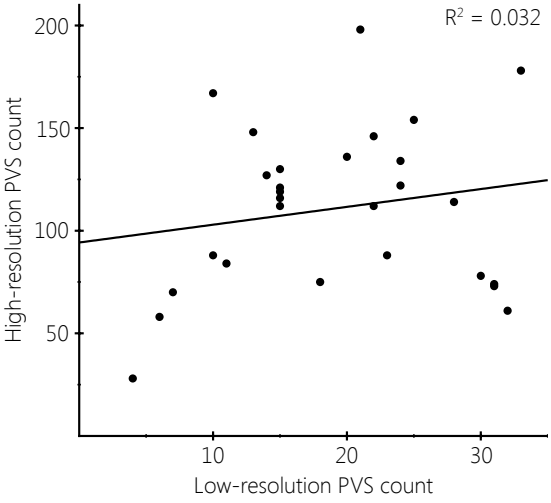

Figure 4 scatter plot of the high- and low-resolution PVS counts. Correlation between the PVS counts was poor (ICC = 0.13, R^2 = 0.032).

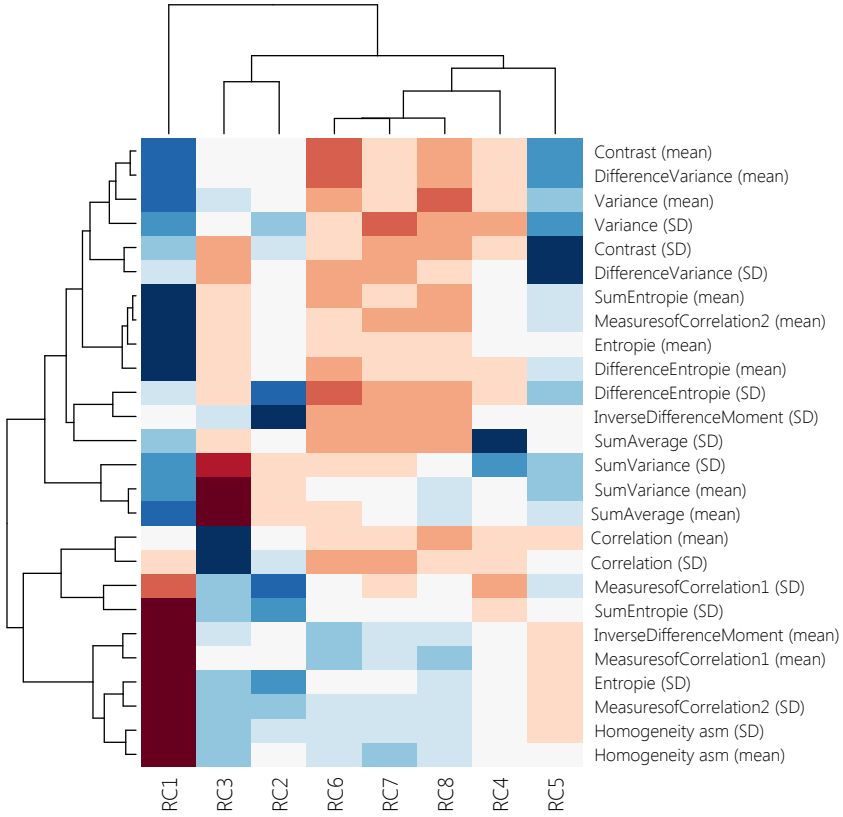

Figure 5 Loadings between the mean/SD-texture feature set and the rotated components. Positive loadings are displayed in blue, negative loadings in red. Darker colors indicate higher loadings.

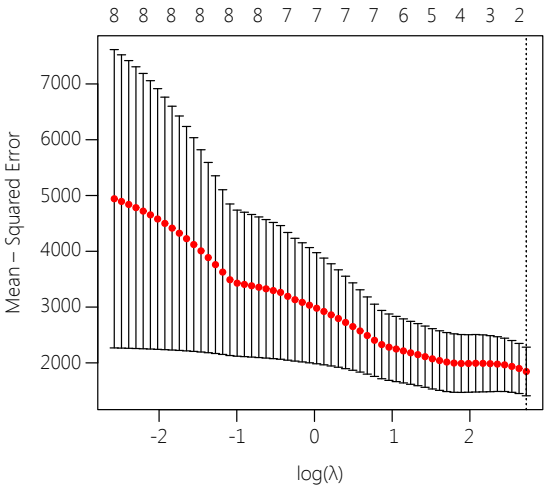

Figure 6 Tenfold cross-validation curve showing the optimal LASSO regularization parameter λ (dotted line) does not select any components (top x-axis).

Discussion

In this work it was investigated if the PVS count obtained in high-resolution scans can be estimated using the PVS count or white matter texture features of scans acquired with a commonly used clinical protocol with low resolution. We hypothesized that the correlation between PVS counts in low- and high-resolution scans is poor, and that texture measures in low-resolution MRI scans can better predict the PVS count in high-resolution scans than the PVS count in the low-resolution scans. The PVS count obtained in high-resolution scans was determined automatically in 3D T_2-weighted TSE images acquired at 7T. The PVS count in the low-resolution scans was determined manually by a human observer. Poor correlation was found between the PVS counts in the low-and high-resolution scans. Texture features based on the co-occurrence matrix were determined using T_2-weighted TSE images acquired at 3T. LASSO analysis did not result in a significant correlation between the texture features and PVS count in low- and high-resolution scans.

The method for automatic PVS detection in the high-resolution scans is a deterministic method. Thus, in contrast to visual PVS annotation, the exact same results are obtained when re-running the PVS detection method. Since this method is not verified for PVS detection in low-resolution scans, manual PVS annotation was performed in the 3T scans. As the PVS count is much lower in the low-resolution 3T scans compared with the high-resolution 7T scans, manual PVS annotation is less labor-intensive and less prone to errors.

The main advantages of 7T MRI are the high signal-to-noise ratio (SNR) and contrast-to-noise ratio (CNR). These allow for high-resolution scanning and the acquisition of images with high anatomical detail. As a result, 7T MRI enables the acquisition of information that cannot be achieved using lower field strengths. This leads to the observation of approximately a fivefold more PVS in 7T MRI images compared with 3T MRI. The correlation between the low- and high-resolution PVS counts was poor. Only the largest PVS are visible in 3T scans, whereas many PVS have a diameter below the mm-scale (*7*) and are thus smaller than the voxel size in the low-resolution 3T scans. Furthermore, PVS visibility in low-resolution scans depends strongly on the used resolution and scan sequence (*7*). As a result, the value of the PVS count in low-resolution scans is questionable. It may be illustrative that correlations between the PVS count in 3T scans and age vary between studies (*12–14*). Furthermore, at 7T the PVS count was found to correlate with SVD measures but not with age (*8*), and asymmetrical PVS counts between both hemispheres were found in epilepsy patients (*11*). The larger PVS count that can be detected at 7T is therefore likely a very valuable parameter.

In this work a LASSO regression analysis was used to determine the correlation between the low- and high-resolution PVS counts and the texture features in the low-resolution scans. This method is insensitive to non-normality of the data, and is therefore a very stable method. As hypothesized, no significant correlation was found between the texture features and the low-resolution PVS count. This suggests that the WM texture is not majorly influenced by the large PVS present in the scan. Contrary to our expectation, there was no significant correlation between the texture features in the low-resolution scans and the high-resolution PVS count. Thus, it seems that PVS that are visible in the 7T scans do not significantly affect the WM texture in the 3T scans. This may be related to the small size of most PVS, as the signal intensity in a voxel containing a small, sub-voxel PVS is only minimally increased compared to voxels containing only WM. It is currently not clear what structures further influence the WM texture features. The WM texture may for example also be affected by other (sub-voxel) structures, such as veins (*29*), or subtle WM lesions that were not visible in the low-resolution 3T scans.

Although it is difficult, it is possible to translate metrics to lower field strengths after successfully achieving this at a high-field strength. This was for example shown for the semi-automatic detection of cerebral microbleeds at 7T and at 3T by Kuijf *et al.* (*30*, *31*). However, in this work no comparison was made between the microbleed counts at 3T and 7T. The reliability of (manual) microbleed rating has been shown to be better at a high field strength (7T) compared to a low field strength (1.5T) (*32*), but also from this work it is not clear if the microbleed count at lower field strengths correlates with the microbleed count at higher field strengths. Also manual annotation of microinfarcts has been translated from 7T to 3T (*33*, *34*). Most microinfarcts that were detected at 3T were also annotated in the 7T scans, but it was not reported if there is a correlation between the 3T and 7T microinfarct counts. The main difference between the detection of cortical microinfarcts and PVS at 3T MRI is the scan resolution. For the detection of micro-infarcts 3T images were used with a voxel size of 1 mm isotropic, which is approximately double the voxel size that was used at 7T (0.8 mm isotropic). In this work commonly used clinical T_2-weighted images were used with voxel size $1\times1\times3$ mm^3, which is almost ten times the voxel size that was used at 7T (0.7 mm isotropic).

Currently, the PVS counts determined using high-resolution scans acquired at 7T MRI cannot be estimated using a commonly used clinical protocol with low-resolution, acquired at 3T MRI. However, 7T MRI is not yet widely available, while 3T MRI is. Therefore, it may be valuable to further investigate texture features in scans acquired at 3T as a measure for the high-resolution PVS count. This may be

aided by increasing the 3T scan resolution and/or SNR, which may be achieved by adjusting the scan sequence. Also the texture features in e.g. the T_1-weighted images may be included in the analysis. Furthermore, other analysis methods may be explored, such as non-linear statistical correlation methods, or deep learning methods. Since the clinical 3T protocol investigated in this work has been used during an extended period of time and has been included in many clinical studies, this merited an attempt to explore if more information could be derived from these scans with feature filtering than one would initially expect given the low resolution.

The main limitation of this work is that this was a feasibility study with a relatively small number of subjects. As a result, the statistical power was limited.

Furthermore, non-linear statistical correlation analyses or deep learning methods were not explored to correlate the low-resolution texture features with the high-resolution PVS count. This was also due to the relatively small number of subjects: for these advanced methods more data is needed to prevent overfitting.

Finally, the PVS annotations were performed in only one slice or plane. Also, the slice orientation of the low-resolution 3T scans was different from the orientation of the CSO-ROI that was positioned automatically in the high-resolution 7T scans (**Figures 1 and 2**). However, although the absolute PVS count may depend on the slice orientation, the relative PVS counts between subjects (i.e. counts in subjects with a lower versus higher PVS load) should not depend strongly on the slice orientation.

Conclusion

No correlation was found between the PVS count in low-resolution T_2-weighted scans acquired at 3T MRI and the PVS count in high-resolution T_2-weighted scans acquired at 7T. Furthermore, the co-occurrence texture features in the white matter in the low-resolution 3T scans did not correlate with the PVS count in the low- and high-resolution 7T scans. Thus, 7T MRI provides information on PVS that cannot yet be acquired using commonly used clinical protocols with modest resolution at lower field strengths. Therefore, the PVS count is currently best determined in the high-resolution scans, or 3T protocols should be improved.

References

1. R. M. Kwee, T. C. Kwee, Virchow-Robin spaces at MR Imaging. *RadioGraphics*. 27, 1071–1086 (2007).
2. R. Brown *et al.*, Understanding the role of the perivascular space in cerebral small vessel disease. *Cardiovasc. Res.* 114, 1462-1473 (2018).
3. N. J. Abbott, M. E. Pizzo, J. E. Preston, D. Janigro, R. G. Thorne, The role of brain barriers in fluid movement in the CNS: is there a 'glymphatic' system? *Acta Neuropathol.* 135, 387–407 (2018).
4. A. Bacyinski, M. Xu, W. Wang, J. Hu, The paravascular pathway for brain waste clearance: current understanding, significance and controversy. *Front. Neuroanat.* 11, 1–8 (2017).
5. A. J. Smith, A. S. Verkman, The "glymphatic" mechanism for solute clearance in Alzheimer's disease: game changer or unproven speculation? *FASEB J.* 32, 543–551 (2018).
6. B. Engelhardt *et al.*, Fluids and barriers of the CNS establish immune privilege by confining immune surveillance to a two-walled castle moat surrounding the CNS castle. *Fluids Barriers CNS.* 8, 4 (2011).
7. J. M. Wardlaw *et al.*, Neuroimaging standards for research into small vessel disease and its contribution to ageing and neurodegeneration. *Lancet Neurol.* 12, 822–838 (2013).
8. W. H. Bouvy *et al.*, Perivascular spaces on 7 Tesla brain MRI are related to markers of small vessel disease but not to age or cardiovascular risk factors. *JCBFM*. 36, 1708–1717 (2016).
9. J. Ramirez *et al.*, Imaging the perivascular space as a potential biomarker of neurovascular and neurodegenerative diseases. *Cell. Mol. Neurobiol.* 36, 289–299 (2016).
10. G. Banerjee *et al.*, MRI-visible perivascular space location is associated with Alzheimer's disease independently of amyloid burden. *Brain*. 140, 1107–1116 (2017).
11. R. E. Feldman *et al.*, Quantification of perivascular spaces at 7 T: A potential MRI biomarker for epilepsy. *Seizure.* 54, 11–18 (2018).
12. A. Charidimou *et al.*, Enlarged perivascular spaces as a marker of underlying arteriopathy in intracerebral haemorrhage: A multicentre MRI cohort study. *J. Neurol. Neurosurg. Psychiatry.* 84, 624–629 (2013).
13. S. Martinez-Ramirez *et al.*, Topography of dilated perivascular spaces in subjects from a memory clinic cohort. *Neurology.* 80, 1551–1556 (2013).
14. G. M. Potter *et al.*, Enlarged perivascular spaces and cerebral small vessel disease. *Int. J. Stroke*. 10, 376–381 (2015).
15. J. de Bresser *et al.*, White matter hyperintensity shape and location feature analysis on brain MRI; Proof of principle study in patients with diabetes. *Sci. Rep.* 8, 1–10 (2018).
16. A. Wibmer *et al.*, Haralick texture analysis of prostate MRI: utility for differentiating non-cancerous prostate from prostate cancer and differentiating prostate cancers with different Gleason scores. *Eur. Radiol*. 25, 2840–2850 (2015).
17. Y. D. Reijmer *et al.*, Microstructural white matter abnormalities and cognitive functioning in type 2 diabetes: A diffusion tensor imaging study. *Diabetes Care.* 36, 137–144 (2013).
18. J. M. Spijkerman *et al.*, Automatic quantification of perivascular spaces in T_2-weighted images at 7T MRI. Under rivision (2018).
19. J. Ashburner, K. J. Friston, Unified segmentation. *Neuroimage*. 26, 839–851 (2005).
20. S. Klein, M. Staring, K. Murphy, M. a. Viergever, J. Pluim, elastix: A toolbox for intensity-based medical image registration. *IEEE Trans. Med. Imaging.* 29, 196–205 (2010).

21. Y. Sato *et al.*, Three-dimensional multi-scale line filter for segmentation and visualization of curvilinear structures in medical images. *Med. Image Anal.* 2, 143–168 (1998).

22. A. F. Frangi, W. J. Niessen, K. L. Vincken, M. A. Viergever, in Medical Image Computing and Computer-Assisted Interventation—*MICCAI'98* (1998), pp. 130–137.

23. *MeVisLab Vesselness* (2018), (available at http://mevislabdownloads.mevis.de/docs/current/FMEsTable/ReleaseMeVis/Documentation/Publish/ModuleReference/Vesselness.html).

24. P. Moeskops *et al.*, Evaluation of a deep learning approach for the segmentation of brain tissues and white matter hyperintensities of presumed vascular origin in MRI. *NeuroImage Clin.* 17, 251–262 (2018).

25. R. M. Haralick, K. Shanmugam, I. Dinstein, Textural features for image classification. *IEEE Trans. Syst. Man Cybern.* smc 3, 610-621 (1973).

26. R. J. Gillies, P. E. Kinahan, H. Hricak, Radiomics: Images are more than pictures, they are data. *Radiology.* 278, 563–577 (2016).

27. R. Tibshirani, Regression shrinkage and selection via the lasso. *J. R. Stat. Soc.* 58, 267–288 (1996).

28. J. Friedman, T. Hastie, R. Tibshirani, Regularization paths for generalized linear models via coordinate descent. *J. Stat. Softw.* 33, 1–22 (2010).

29. H. J. Kuijf *et al.*, Quantification of deep medullary veins at 7 T brain MRI. *Eur. Radiol.* 26, 3412–3418 (2016).

30. H. J. Kuijf *et al.*, Efficient detection of cerebral microbleeds on 7.0 T MR images using the radial symmetry transform. *Neuroimage.* 59, 2266–2273 (2012).

31. H. J. Kuijf *et al.*, Semi-automated detection of cerebral microbleeds on 3.0 T MR images. *PLoS One.* 8 (2013), doi:10.1371/journal.pone.0066610.

32. M. M. A. Conijn *et al.*, Cerebral microbleeds on MR imaging: Comparison between 1.5 and 7T. *Am. J. Neuroradiol.* 32, 1043–1049 (2011).

33. S. J. van Veluw *et al.*, In vivo detection of cerebral cortical microinfarcts with high-resolution 7T MRI. *J. Cereb. Blood Flow Metab.* 33, 322–329 (2013).

34. S. J. van Veluw *et al.*, Cortical microinfarcts on 3T MRI: Clinical correlates in memory-clinic patients. *Alzheimer's Dement.* 11, 1500–1509 (2015).

Chapter 4

PC-MRI measurements of net CSF flow through the cerebral aqueduct are confounded by respiration

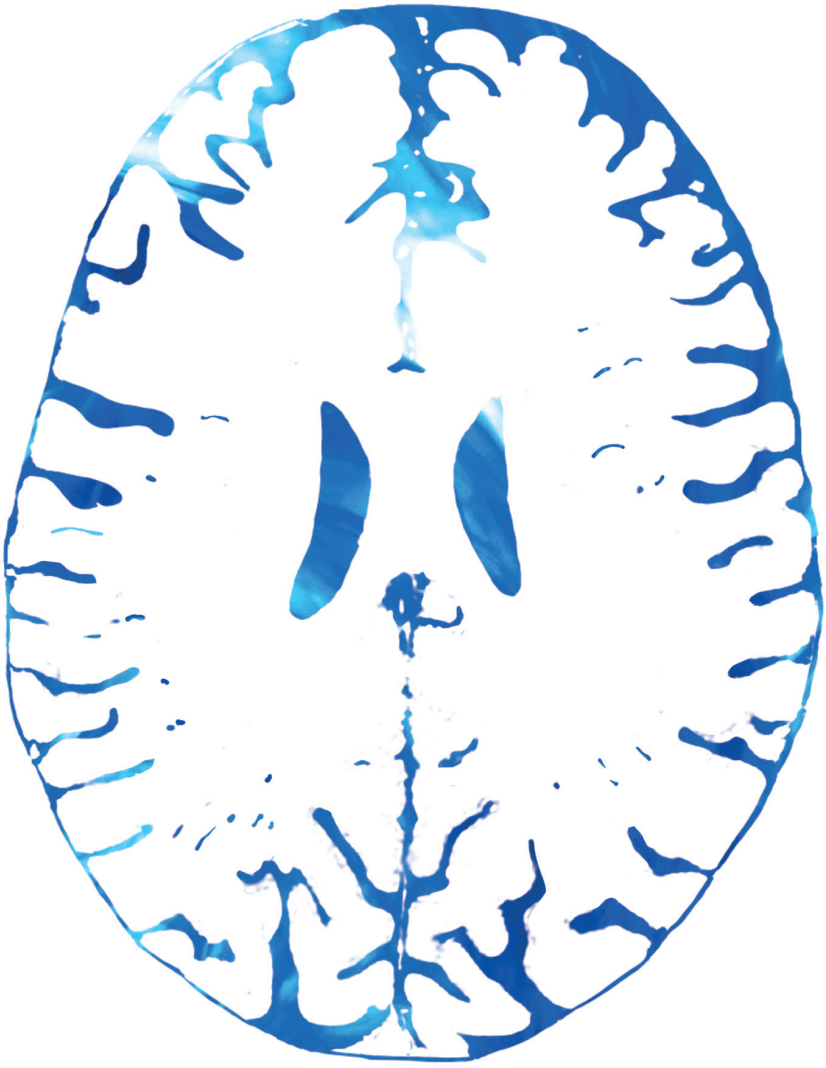

Jolanda M. Spijkerman, Lennart J. Geurts, Jeroen C.W. Siero,
Jeroen Hendrikse, Peter R. Luijten, Jaco J.M. Zwanenburg

Based on: Journal of Magnetic Resonance Imaging, 2018 [Epub ahead of print]

Abstract

Objective

Net cerebrospinal fluid (CSF) flow through the cerebral aqueduct may serve as measure of CSF production in the lateral ventricles, and changes that occur with aging and in disease. In this work the confounding influence of the respiratory cycle on net cerebrospinal fluid (CSF) flow and stroke volume measurements was investigated.

Methods

In 12 volunteers net CSF flow was measured using PC-MRI at 7T MRI, with respiratory gating on expiration and on inspiration, and without respiratory gating. All measurements were repeated. For each scan the net CSF flow and stroke volume in the aqueduct over the cardiac cycle was determined. Repeatability was determined using the Intraclass Correlation Coefficient (ICC) and linear regression analyses between the repeated measurements. Repeated measures ANOVA was performed to compare the measurements during inspiration/expiration/no gating. Linear regression analysis was performed between the net CSF flow difference (inspiration minus expiration) and stroke volume.

Results

Net CSF flow (average ± standard deviation) was 0.64±0.32 mL/min (caudal) during expiration, 0.12±0.49 mL/min (cranial) during inspiration, and 0.31±0.18 mL/min (caudal) without respiratory gating. Respiratory gating did not affect the stroke volume measurements (41±18, 42±19, 42±19 µL/cycle for expiration, no respiratory gating and inspiration, respectively). Repeatability of the net flow was best during inspiration (ICC = 0.88/0.56/-0.31 for gating on inspiration/expiration/no gating). A positive association was found between average stroke volume and net flow difference between inspiration and expiration (R = 0.678/0.605, p = 0.015/0.037 for the first/second repeated measurement).

Conclusion

The measured net CSF flows are confounded by respiration effects. Therefore, net CSF flow measurements with PC-MRI cannot - in isolation - ,be directly linked to CSF production.

Introduction

Cerebrospinal fluid (CSF) plays an important role in maintaining homeostasis and in the clearance system of the brain (*1,2*). With aging, CSF production and CSF flow decline (*3,4*), which may be related to age-related cognitive decline (*5,6*). Also, in normal pressure hydrocephalus CSF flow is altered (*7*). Therefore, non-invasive measurements of CSF production in combination with advanced brain imaging may provide a useful tool to study the role of CSF changes in aging and disease. CSF net flow through the cerebral aqueduct (aqueduct of Sylvius) over the cardiac cycle can potentially serve as a measure for CSF production in the lateral ventricles by the choroid plexus, and can be measured using phase-contrast MRI (PC-MRI) (*8–12*). PC-MRI can be acquired in approximately 2 minutes of imaging time (*4,11*); hence the resulting CSF flow waveform is the average of many cardiac cycles.

PC-MRI measurements of net CSF flow over the cardiac cycle rely on the assumption that relatively large CSF displacements due to the respiratory cycle (*13–16*) average out over the acquisition time of the measurements (*10*). Although this seems a reasonable assumption given the relatively long acquisition time compared with the duration of the respiratory cycle, respiration may be a stronger confounder in the PC-MRI measurements of net CSF flow than expected. In fact, reversed net CSF flow (in cranial direction) has also incidentally been observed in healthy subjects in several studies (*17,18*). Possibly incomplete averaging of respiratory effects contributed to these cases of reversed net CSF flow.

The main goals of this work were to determine the net CSF flow over the cardiac cycle through the cerebral aqueduct, and to investigate whether the net CSF flow measurements are confounded by respiratory-induced CSF motion. We hypothesized that the incidentally observed reversed net CSF flows may be due to respiratory effects. Our secondary goals were, first, to determine the repeatability of the measurements and, second, to compare CSF stroke volume (cardiac-induced pulsatility) with the size of the confounding effect from respiration (as a measure for respiration-induced CSF pulsatility).

Methods

Experimental design

Twelve young, healthy volunteers (7 male, age range 19 - 39 years, mean age 28.3 years) participated in this study. Informed consent was given in accordance to the Institutional Review Board of the University Medical Center Utrecht (Utrecht, The Netherlands). To achieve high SNR and good spatial resolution, which minimizes

partial volume, the measurements were performed at 7T MRI (Philips Healthcare, Best, the Netherlands) using a volume transmit coil and a 32-channel receive coil (Nova Medical, Wilmington, MA, USA). Physiology was recorded using vendor-supplied equipment: the peripheral pulse unit (PPU) was used for cardiac gating, and the respiratory belt was used for respiratory gating. Since the circadian rhythm has been reported to influence net CSF flow (*18*), all measurements were conducted between 8:00 and 10:00 a.m.. PC-MRI measurements were performed in the cerebral aqueduct with encoding velocity (v_{enc}) 15 cm/s. A single slice was acquired, with acquired resolution 0.45×0.45×3 mm^3 reconstructed to 0.25×0.25×3 mm^3, FOV 190×185×3 mm^3, and 36 – 45 frames were reconstructed per cardiac cycle, depending on the heart rate of the volunteer. Other parameters were: TR/TE 12/5.9 ms, R-R window 15%/25%, 2 k-lines per cardiac cycle with alternating positive and negative flow encoding for background phase error removal (yielding an acquired temporal resolution of 4*TR = 48 ms), bandwidth 375.2 Hz/pixel, flip angle 12 degrees, and SENSE factor 2. Retrospective cardiac gating was performed. A whole-brain 3D T_1-weighted TFE scan (resolution 1 mm isotropic, FOV 190×248×300 mm^3, TR/TE 4.2/2.0 ms, inversion recovery time 1281 ms, repetition time between inversion pulses 3000 ms, flip angle 7 degrees, SENSE factor 2, scan time 2:00 min) and a whole-brain T_2-weighted 3D balanced gradient echo scan (resolution 0.6 mm isotropic, FOV 192×221×250 mm^3, TR/TE 5.0/1.9 ms (partial echo), flip angle 30 degrees, SENSE factor 2.1, scan time 1:44 min) were acquired for planning of the PC-MRI scan, as illustrated in **Figure 1AB**. The volunteers were instructed to perform calm abdominal breathing. The PC-MRI measurements were performed for two different forms of respiratory gating: (1) respiratory gating on expiration and (2) respiratory gating on inspiration, resulting in image acquisition only during expiration or inspiration. Respiratory gating on expiration was available in the vendor-supplied scanner software, this was extended to allow also for gating on inspiration. This was compared with no respiratory gating, which can be regarded as the current common practice. Each protocol was repeated (without repositioning of the subject) to allow assessment of repeatability of the potential effect of respiration: apart from differences in the respiratory and cardiac traces, there were no variations between the scans. Scan time per scan varied between 1:28 – 1:52 min without respiratory gating, and between 4:26 – 5:38 min with respiratory gating, depending on the heart rate of the volunteer.

Data processing

Background correction was performed with a method previously developed for blood flow velocity quantification in small perforating arteries (*19*), additionally to

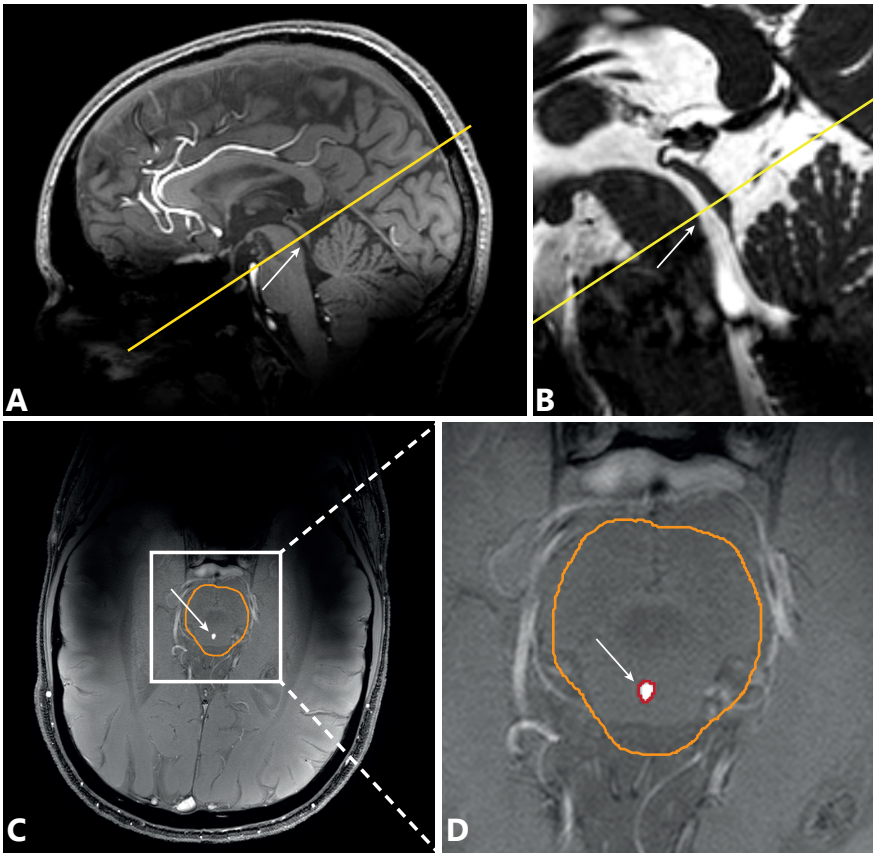

Figure 1 Slice planning of the PC-MRI scan (single slice, yellow) for subject 5, relative to a whole-brain 3D T_1-weighted TFE scan (A) and a whole-brain T_2-weighted 3D balanced gradient echo scan (B), the corresponding, manually drawn, brain stem ROI (orange) in the magnitude image (C), and the automatically determined aqueduct ROI (red) (D). The cerebral aqueduct is indicated by the white arrow.

the background velocity correction provided by the vendor. Mean background phase was determined by applying a median filter (kernel size 15×15 mm^2) to the mean of all phase images over the cardiac cycle. This mean background phase was then subtracted from all phase images over the cardiac cycle.

A region-of-interest (ROI) of the brain stem was drawn manually on the magnitude image of each scan (**Figure 1C**) , to facilitate automatic detection of the aqueduct area. Phase unwrapping was performed within this ROI using Goldstein's method (*20*), in all scans that showed phase wrapping at any time point in the cardiac cycle.

The cerebral aqueduct was automatically determined within the brain stem ROI, by selecting the voxels with a significant signal intensity relative to the background, using the magnitude images. The aqueduct mask was determined in two steps. First, the mean background magnitude was obtained by median filtering the mean magnitude image (kernel size 15×15 mm^2). Second, the standard deviation (SD) of the real and imaginary parts of the signal over the cardiac cycle was determined pixel by pixel. The root-mean-square of the real and imaginary standard deviation was median filtered (kernel size 15×15 mm^2) and used as a map of the noise background. The background signal was assumed to be stable over the cardiac cycle, therefore signal variation over the cardiac cycle was regarded as noise. One aqueduct mask is determined for all phases over the cardiac cycle, assuming that the diameter variation was well below the image resolution. The aqueduct mask was defined as all voxels with a signal intensity significantly above the background magnitude, and were automatically determined using the estimated background noise map and significance level $p<0.01$ (*19*). An example of the resulting aqueduct mask is shown in **Figure 1D**.

Finally, the average velocity curve of the aqueduct ROI was determined. Then the net velocity over the cardiac cycle was determined by integrating the average CSF velocity curve over the cardiac cycle. To obtain the net CSF flow over the cardiac cycle the net velocity was multiplied by the aqueduct area. By convention in this paper, positive flows are in cranial direction, negative flows are in caudal direction. To assess the net flow profiles in the aqueduct, for all subjects the net velocity per voxel was plotted. Furthermore, stroke volumes were determined by averaging the (absolute) systolic (caudal) and diastolic (cranial) flow volumes through the aqueduct over the cardiac cycle, for each measurement.

Statistical analysis

As a measure for the repeatability of the net CSF flow and stroke volume measurements, the difference and absolute difference in net CSF flow between the repeated measurements were determined for each subject. Also the Intraclass Correlation Coefficient (ICC) was determined, and linear regression analysis between the first (independent variable) and second (dependent variable) measurement was performed.

To visually compare the CSF flow for the different respiratory conditions, the mean normalized CSF flow curves were plotted for each respiratory condition. First the CSF flow curves were interpolated to 100 time points (0-100% of the cardiac cycle). Subsequently all flow curves were normalized relative to the absolute maximal

observed flow in any of the 6 measurements (3 respiratory conditions, each measured twice), and the average flow curve for each respiratory condition was determined. Finally, the mean ± standard error of the mean (SEM) flow curve of all volunteers were determined for each respiratory condition.

To compare the different respiratory conditions, boxplots were made for the average measured net CSF flow per subject during inspiration gating, expiration gating, and without respiratory gating. Repeated measures ANOVA was performed to compare the net CSF flows and stroke volumes during inspiration gating, expiration gating, and without respiratory gating, for the first and the second measurements separately. A significance level of $p<0.05$ was used, and Bonferroni correction was applied for the pairwise comparisons (3 tests).

To explore the relation between the CSF pulsatility (stroke volume) and the influence of the respiration phase on the net CSF flow, linear regression analyses were performed between the net CSF flow difference for inspiration minus expiration (dependent variable) and the average stroke volume of inspiration and expiration (independent variable), for the first and second measurements separately. A significance level of $p<0.05$ was used.

Data processing was performed with Matlab (version 2017A, Mathworks, Natick, MA, USA). Statistical analyses were performed with IBM SPSS (version 24).

Results

Scans were successfully completed for all volunteers. In ten scans, of three subjects, phase unwrapping was performed. The size of the automatically acquired aqueduct ROIs varied between 1.3 – 5.8 mm^2. No difference in background correction was found between gating on inspiration, gating on expiration, or no respiratory gating (data not shown). The maximum CSF velocities varied between 3.4 – 16.7, 2.8 – 13.0, 3.1 – 15.7 cm/s, during inspiration gating, expiration gating, and without respiratory gating, respectively. No (inverse) correlation was found between the aqueduct area and the maximum CSF velocity. No correlation was found between the cardiac frequency and the net CSF flow or between the cardiac frequency and the stroke volume. Between the various CSF flow scans, the cardiac frequency ranged between 97 – 105% of the average cardiac frequency for each subject (percentages averaged over all volunteers, min/max observed difference was 95%/109%). The respiratory frequencies ranged between 0.16 – 0.32 Hz.

CSF flow and stroke volume relative to the respiratory phase

Figure 2 shows the mean ± SEM normalized CSF flow in the aqueduct over the cardiac cycle during expiration gating, inspiration gating, and without respiratory gating for all volunteers and for both repeated measurements. The CSF flow curve for the inspiration gated measurements lies consistently above the curve for expiration gated measurements, and the curve for no respiratory gating lies in between the curves for inspiration and expiration. Individual CSF flow curves during inspiration and expiration gating for the first measurement show generally the same pattern, and are shown in **Figure 3**.

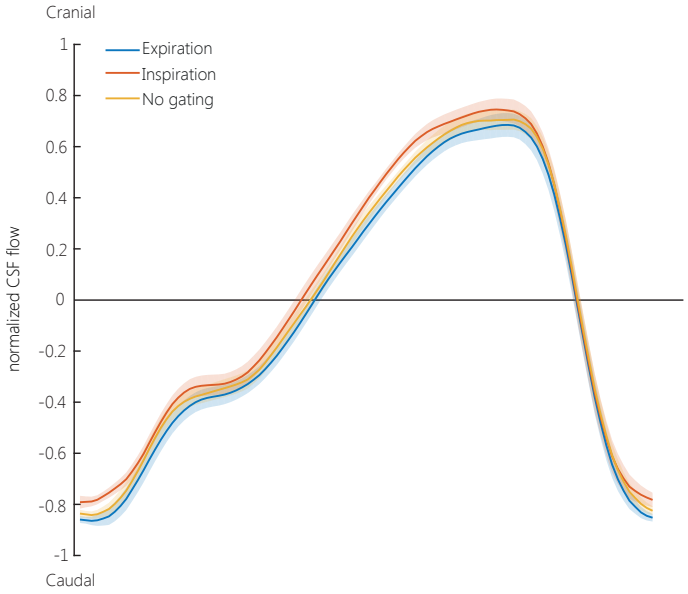

Figure 2 Average normalized CSF velocity in the aqueduct over the cardiac cycle, averaged over both repeated measurements and all subjects, during expiration (blue), inspiration (orange), and no gating (yellow). The CSF flow curves were interpolated (using cubic interpolation with the Matlab function interp1) to 100 time points (0-100% of the cardiac cycle). As triggering was performed using a peripheral pulse oximeter, the cardiac cycle starts around peak-systole. The cardiac cycle duration varied between 857 – 1090 ms. The line represents the average CSF velocity, the transparent band represents the SEM. Normalization was performed per subject, by dividing by the maximum absolute velocity of any of the 6 measurements (three respiratory conditions, each measured twice).

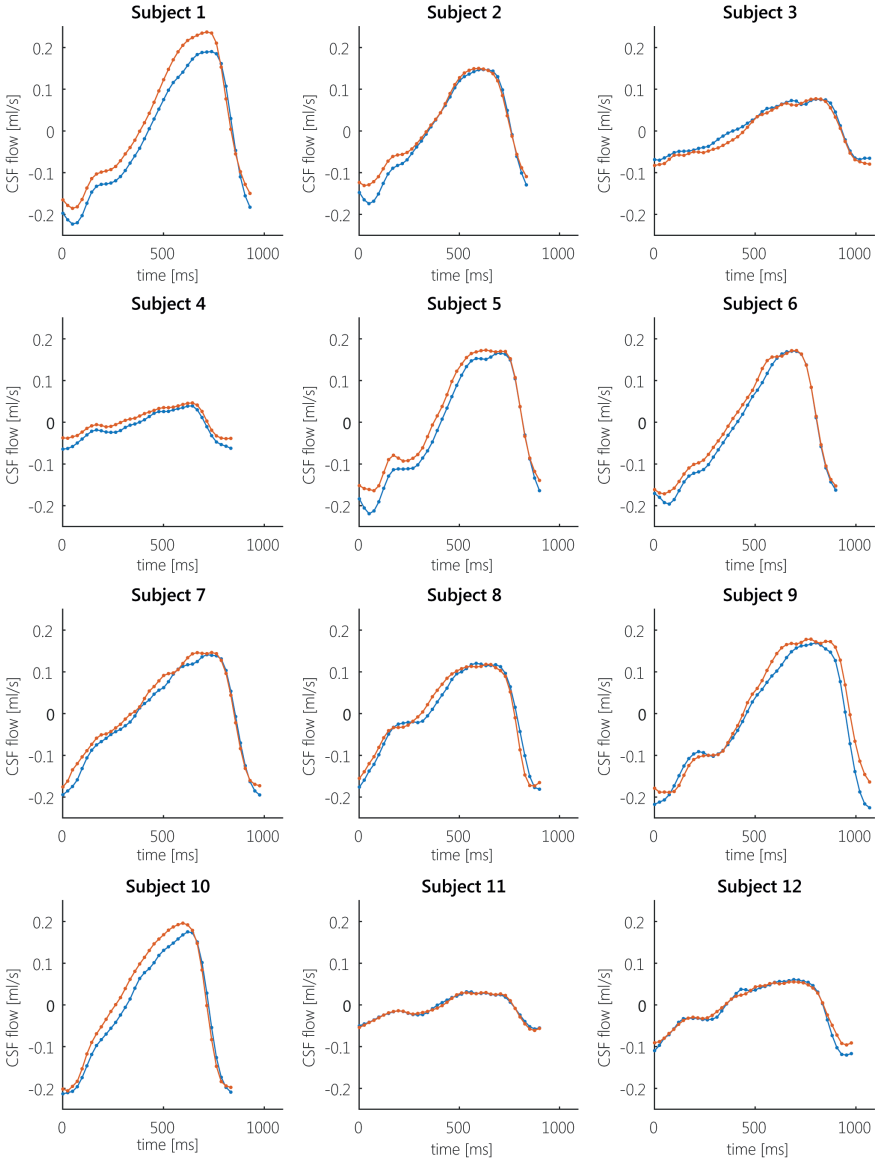

Figure 3 Individual CSF flow profiles during inspiration (orange) and expiration (blue) for all subjects, for the first measurement. Positive CSF flow is in cranial direction, negative CSF flow is in caudal direction. For most subjects, the CSF flow profile during inspiration is above the CSF flow profile during expiration. Subject 3 showed cranial net flow during expiration, and caudal flow during inspiration. Subject 11 and 12 showed similar flows during inspiration and expiration.

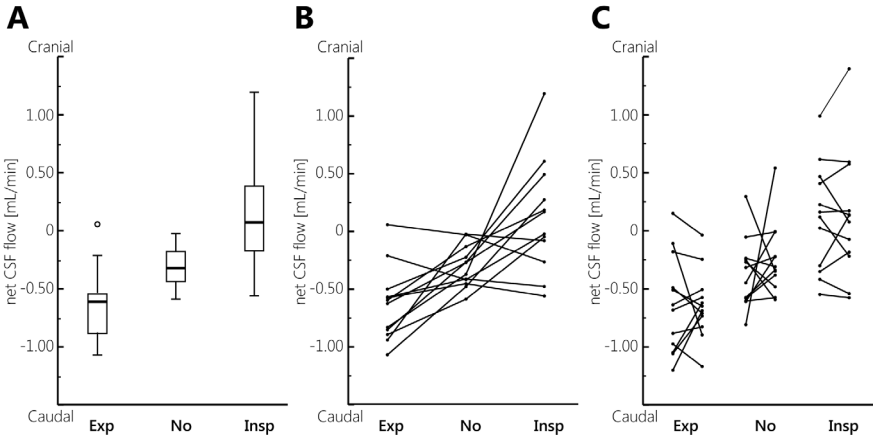

Figure 4 Boxplots of the mean net CSF flow (over both measurements) measured in each subject, during expiration gating (Exp), no gating (No), and inspiration gating (Insp) (A), the mean net CSF flow measured in each subject (B), and the net CSF flow measured in each subject during the first and second measurement (C). Outliers are represented by the open circles. Except for one outlier, only negative (caudal) net CSF flows were observed during expiration, while often positive (cranial) flows were measured during inspiration. Generally, the net CSF flow measured without respiratory gating is in between the net CSF flows measured during expiration and inspiration.

Figure 4A shows the average net CSF flow per subject during inspiration gating, expiration gating, and without respiratory gating. During expiration the largest caudal net CSF flows were found, during inspiration the largest cranial net CSF flows were found. The net CSF flows measured without respiratory gating are in between the net CSF flows measured during expiration and inspiration. **Figure 4B** shows the average net CSF flow during the different respiratory conditions per subject. In 9 out of 12 subjects, during expiration most caudal (negative) net flow was found, and during inspiration net flow was cranial (positive) or considerably smaller compared with expiration. For two subjects, similar caudal net CSF flows were found during expiration and inspiration. One subject showed a somewhat reversed effect, with caudal net flow during inspiration (0.35 mL/min and 0.18 mL/min for the repeated measurements, respectively) and inconsistent net flow during expiration (0.04 mL/min in caudal direction, and 0.15 mL/min in cranial direction for the repeated measurements, respectively).

The repeated measures ANOVA showed that overall significantly different net CSF flows were measured between the respiratory conditions (tests of within-subject effects): the resulting p-values were 0.001 for both the first and second measurement. The pairwise comparisons showed that the difference in net CSF

flow between expiration and inspiration is very similar between the repeated measurements. The resulting mean differences and the corresponding p-values for the pairwise comparisons are summarized in **Table 1**. For the stroke volumes no (significant) differences were found between the respiratory conditions: the resulting p-values were 0.122 and 0.23 for the first and second measurement, respectively.

Table 1. Net CSF flow differences

		Mean difference ± SEM [mL/min]	p-value
Measurement 1	Expiration - Inspiration	-0.75 ± 0.20	0.010 *
	No gating - Expiration	-0.26 ± 0.15	0.348
	No gating - Inspiration	0.49 ± 0.17	0.045 *
Measurement 2	Expiration - Inspiration	-0.76 ± 0.20	0.008 *
	No gating - Expiration	-0.39 ± 0.12	0.027 *
	No gating - Inspiration	0.37 ± 0.18	0.196

Net CSF flow differences (mean±SEM) between the respiratory gating conditions, and the corresponding p-values, for the pairwise comparisons of the repeated measures ANOVA, for the first and the repeated net CSF flow measurements during expiration gating, inspiration gating, and without respiratory gating. Significant p-values are represented by the asterisk symbol.

The net CSF flow for all aqueduct voxels during expiration gating, inspiration gating, and without respiratory gating for all subjects, for the first measurement, is shown in **Figure 5**. Large inter-subject variation can be observed between the net CSF flow profiles over the aqueduct. The subject specific patterns were consistent between the various respiratory gating schemes, but generally more cranial flow was observed during inspiration gating compared with expiration gating or no gating. Very similar net flow patterns were found during the second measurement (data not shown).

Repeatability of net CSF flow and stroke volume measurements

Figure 4C shows the individual net CSF flows for each subject, for the repeated measurements. For the measurements without respiratory gating the largest within-subject variation can be observed, compared with the respiratory gated

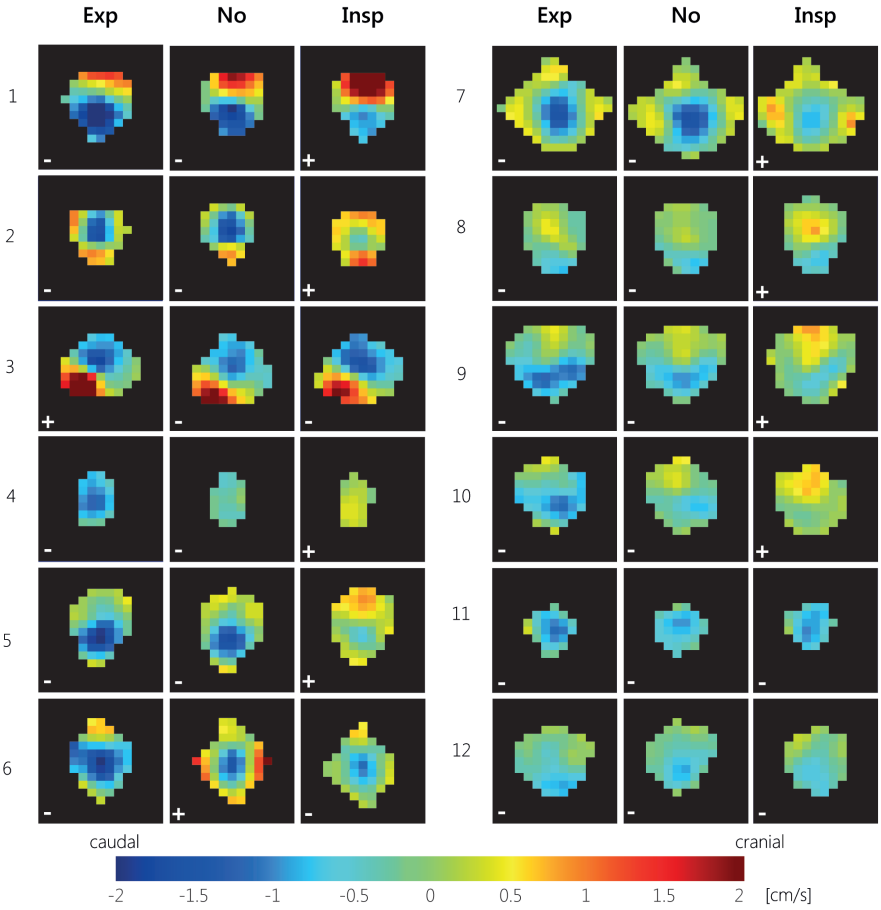

Figure 5 CSF net flow for all aqueduct voxels during expiration gating (Exp), inspiration gating (Insp), and without respiratory gating (No) for all twelve subjects, for the first measurement. For most subjects, during expiration gating most voxels show caudal net CSF flow, and during inspiration gating more voxels show (larger) cranial net CSF flow. The net CSF flow directions were indicated with +/- symbols for cranial/caudal net CSF flow.

measurements. The repeatability results for the net CSF flows and stroke volumes for expiration gating, without respiratory gating, and inspiration gating are summarized in **Table 2**. The mean net CSF flow was negative (caudal) during expiration gating and without respiratory gating, and positive (cranial) during inspiration gating, for both measurements. The difference and absolute difference between the repeated measurements are larger without respiratory gating compared with the inspiration and expiration gated measurements. Also, the standard deviation of the difference between the repeated measurements is largest without respiratory gating.

Table 2. Repeatability of net CSF flow and CSF stroke volume

	Net CSF flow [mL/min]			Stroke volume [µL/cycle]		
	Exp	**No**	**Insp**	**Exp**	**No**	**Insp**
Measurement 1 (M1)	-0.63 ± 0.42	-0.37 ± 0.30	0.12 ± 0.46	42 ± 18	43 ± 19	41 ± 18
Measurement 2 (M2)	-0.64 ± 0.29	-0.24 ± 0.31	0.13 ± 0.54	41 ± 18	42 ± 20	43 ± 20
Average: (M1+M2)/2	-0.64 ± 0.32	-0.31 ± 0.18	0.12 ± 0.49	41 ± 18	42 ± 19	42 ± 19
Difference: M1 – M2	0.003 ± 0.35	-0.13 ± 0.49	-0.01 ± 0.25	2 ± 2	0 ± 2	-1 ± 4
Absolute difference: |M1 – M2|	0.26 (0.06 – 0.79)	0.34 (0.03 – 1.35)	0.19 (0.01 – 0.43)	2 (0 – 4)	2 (0 – 4)	3 (0 – 8)
Intraclass Correlation Coefficient (ICC)	0.56	-0.31	0.88	0.99	0.99	0.98

Repeatability of net CSF flow and CSF stroke volume (mean ± standard deviation (SD)) during expiration-, inspiration-, and no gating, showing the results for the first and second measurement, the average of the first and second measurement, and the difference (mean ± SD) and absolute difference (mean (range)) between the first and second measurement, and the Intraclass Correlation Coefficient (ICC) between both measurements.

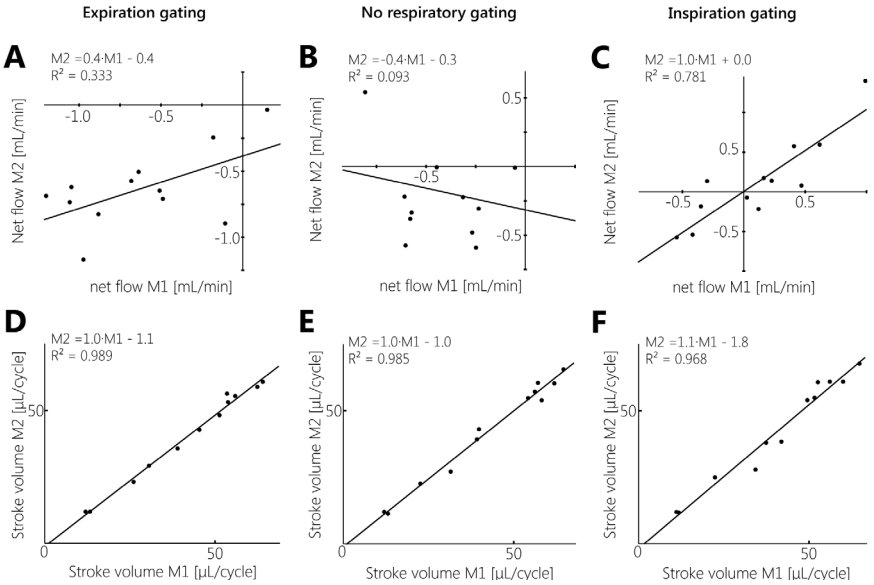

Figure 6 Linear regression analysis between the first (independent variable) and second (dependent variable) measurements for net CSF flow (A-C) and stroke volume (D-F), for gating on expiration, no respiratory gating, and gating on inspiration. For net CSF flow, only gating on inspiration showed very good repeatability, as the regression line was very close to M2 = M1; a fair correlation between both measurements was seen for gating on expiration; and no significant correlation was found between both measurements without respiratory gating. For stroke volume, repeatability was good for all respiratory conditions, with regression lines approximating M2 = M1.

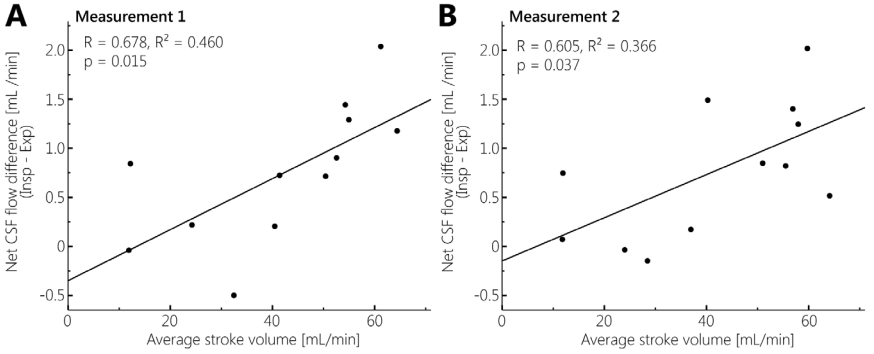

Figure 7 Regression analysis between the net CSF flow difference for inspiration minus expiration, and the average stroke volume for expiration and inspiration, for measurement 1 (A) and measurement 2 (B). Significant, positive associations were found for both measurements.

During inspiration gating the standard deviation of the difference between the repeated measurements is smallest, and the ICC is largest. Without respiratory gating ICC is negative. Regression analysis resulted in significant correlations between the first and second measurement for inspiration and expiration gating, as shown in **Figure 6A-C**. For the inspiration gated measurements, the regression line was approximately M2 = M1, indicating good repeatability.

For all respiratory conditions and both measurements similar stroke volumes were measured. The difference and absolute difference in stroke volume between the repeated measurements were close to zero, and the ICCs were high (at least 0.98). Regression analysis resulted in significant correlations between the first and second measurement, as shown in **Figure 6D-F**. For all respiratory conditions the regression line was approximately M2 = M1. The stroke volumes were highly repeatable, regardless of the type of respiratory gating.

Net CSF flow difference relative to CSF stroke volume

Overall, smaller net CSF flow differences between inspiration and expiration gating were observed for the subjects that showed less pulsatile (flatter) CSF flow curves (**Figure 3**); this can also be observed from the smaller difference between the CSF flow profiles during the inspiration and expiration gated measurements. Linear regression analysis confirmed this correlation between net CSF flow difference (inspiration gated minus expiration gated) (dependent variable) and stroke volume (average stroke volume of inspiration and expiration) (independent variable), as illustrated in **Figure 7**: for both measurements significant, positive associations were found.

Discussion

In this work it was investigated whether net CSF flow measurements with PC-MRI are confounded by respiratory-induced CSF motion, by performing PC-MRI measurements with various respiration conditions, using respiratory gating. The results confirmed that net CSF flow measurements are confounded by respiration: consistent caudal net CSF flow was found during expiration, while on average cranially directed net CSF flow was found during inspiration. Stroke volumes were not affected by respiratory gating. The repeatability of the net CSF flow measurements was best during inspiration. A significant, positive association was found between CSF stroke volume and net CSF flow difference between inspiration and expiration

gated measurements. During the measurements without respiratory gating two outliers were found in the repeated measurements of two different subjects with a relatively large cranially directed net CSF flow.

The observed change in net CSF flow during inspiration compared with expiration is in line with the altered CSF dynamics measured using real-time PC-MRI measurements, as shown in literature. Klose *et al.* (*15*) qualitatively investigated CSF flow dynamics over the cardiac and respiratory cycle, and showed increased cranial flow and decreased caudal flow during inspiration, and the reversed effect during expiration. Yamada *et al.* (*16*) investigated CSF movement in the cerebral aqueduct during inspiration and expiration, and found cranial CSF motion during inspiration, and caudal CSF motion during expiration. Dreha-Kulaczewski *et al.* (*13,21*) performed real-time measurements of CSF flow dynamics, and found upward (cranial) CSF flow during inspiration, and downward (caudal) CSF flow during expiration. Chen *et al.* (*14*) performed real-time velocity mapping, and also found cranial CSF velocities during inspiration, which was reversed during expiration. Takizawa *et al.* (*22*) investigated the relative contributions of the cardiac and respiratory cycles to CSF velocity and CSF displacement, and showed that the contribution of the respiratory cycle to CSF velocity in the aqueduct is smaller compared with the cardiac cycle, but that the resulting total displacement through the aqueduct is larger than the displacements induced by the cardiac cycle. Daouk *et al.* (*23*) investigated blood and CSF flows using signal intensity changes, and found that arterial blood flow is influenced mostly by the cardiac cycle, while venous blood flow is influenced mostly by the respiratory cycle. CSF appeared to act as a buffer between the arterial and venous blood compartments.

Real-time PC-MRI measurements could potentially be used to determine the net CSF flow through the aqueduct, which is usually performed using PC-MRI, as was done in this work. At 3T, Dreha *et al.* achieved a temporal resolution of 135 ms for a pair of two flow-encoded images (*21*), and Yildiz *et al.* achieved a temporal resolution of 50 ms (*24*), which could offer net CSF flow measurements that are not confounded by the respiratory cycle. However, currently the application of real-time PC-MRI to measure net CSF flow is limited by the relatively low spatial resolution, Dreha *et al.* achieved a spatial resolution of 1.2×1.2×5 mm^3 (*21*), and Yildiz *et al.* achieved a spatial resolution of 2.5×2.5×10 mm^3 (*24*), making this technique more prone to partial volume. PC-MRI on the other hand, offers much better spatial resolution, but low temporal resolution. Furthermore, it is important to evaluate if net CSF flow over one cardiac cycle, which can be acquired with real-time PC-MRI measurements, is representative for the net CSF flow over a longer

period of time.

The average net CSF flow acquired without respiratory gating in this work (0.31±0.18 mL/min) is in line with values found in literature, ranging between 0.26 – 0.74 mL/min (*8, 10–12, 25–27*). In these papers spatial resolutions varied between 0.39×0.39×6 mm^3 and 0.9×0.9×6 mm^3, scanning was performed at 1.5T or 3T, and 16 or 32 frames per cardiac cycle were acquired. Our net CSF flow values are on the lower end of this range, which was partially caused by the two outliers showing net cranial flow when no respiratory gating was used (excluding these two subjects would result in an average net CSF flow of 0.35±0.16 mL/min). Furthermore, our spatial resolution was relatively high (0.45×0.45×3 mm^3), especially regarding slice thickness, reducing partial volume in the aqueduct ROI and thereby resulting in smaller overestimation of net CSF flow. Also, the relatively small slice thickness, short TR, and low flip angle used in this work limited the possible bias in the acquired CSF velocities induced by RF saturation (*28*). Finally, a relatively high temporal resolution and SNR were achieved (scanning was performed at 7T, and 36 – 45 frames per cardiac cycle were acquired, with a temporal resolution of 48 ms), resulting in a relatively high accuracy of the estimated net CSF flow, which is small relative to the stroke volumes.

The stroke volumes found in this work (41±18, 42±19, and 42±19 µL/cycle for gating on expiration, gating on inspiration, and no respiratory gating, respectively) are in line with values found in literature, ranging between 30 – 50 µL/cycle (*4, 29, 30*).

Net CSF flow measurements are influenced by the respiratory cycle. In this work for two different subjects cranial net CSF flow was found when no respiratory gating was applied, which is likely due to a difference in the (changeable) respiration between these measurements. Also in previous exploratory work (*17*) and in literature (*18*) such outliers were found, with cranial net CSF flow in healthy subjects when no respiratory gating was performed. It is perhaps illustrative that the results without respiratory gating were significantly different from the inspiration gated (but not expiration gated) results in the first measurement, while this was opposite in the second measurement (**Table 1**). This suggests that, when no respiratory gating is performed, net CSF flow may be closer to either inspiration or expiration, and respiration effects may not average out over the acquisition.

These results violate the general assumption that all respiratory variation averages out over the acquisition time of net CSF flow measurements (*10*). Also Yildiz *et al.* (*24*) concluded that respiration effects average out in conventional PC-MRI, based

on phantom measurements. However, Yildiz *et al.* analyzed only the flow curve shape, but did not show the net flow. From Figure 3 in the work by Yildiz *et al.*, a slight shift between the velocity curves can be observed. Estimating the net flows from this figure using an online tool to digitize the plot (*31*), yields a net flow difference between the PC-MRI measurements with and without respiration effects of approximately 0.4 ml/min, which is comparable to the total net CSF flows in our in vivo measurements (data not shown).

We found that the stroke volume was not affected by respiration, implying that the respiratory phase determines the offset of the CSF flow curve over the cardiac cycle, but does not alter the flow curve shape. The large influence of respiration on net CSF flow measurements may be explained by changes in thoracic pressure over the respiratory cycle. During inspiration a drop in thoracic pressure occurs, resulting in increased outflow of venous blood from the head. During expiration the opposite happens: thoracic pressure increases, resulting in reduced outflow of venous blood from the head (*21*). According to the Monro-Kellie hypothesis (*32*), these changes in intracranial blood volume must be compensated by changes in CSF volume.

Between the CSF stroke volume and the net CSF flow difference between inspiration and expiration a significant, positive correlation was found. Thus, in subjects with larger CSF flow pulsatility over the cardiac cycle also larger respiratory-induced CSF flow variation was found. This suggests that either the respiratory or the cardiac cycle can be used as non-invasive driver to assess the cerebrovascular compliance: both stroke volume and net CSF flow difference between inspiration and expiration reflect changes in intracranial blood volume variation over the cardiac and respiratory cycles. Inter-individual differences in CSF dynamics in the aqueduct may either reflect differences in (intracranial) blood volume pulsation, or differences in the relative contributions of the ventricles and subarachnoidal space to accommodate blood volume pulsations. Following the Monro-Kellie hypothesis, CSF flow from either the ventricles (via the aqueduct) or the subarachnoidal space (via the spinal canal) can compensate for this blood volume variation. Balédent *et al.* (*33*) showed that stroke volumes through the aqueduct are only approximately 10% of the stroke volumes through the spinal canal, without correlation between these two stroke volumes. Therefore, spinal CSF measurements should be included when studying the cerebrovascular compliance.

Repeatability of the net flow measurements in this work was best for inspiration, followed by expiration. When no respiratory gating was performed ICC was negative. Removing the two outliers (with cranial net CSF flow) would result in

an ICC of 0.24. The low repeatability when no respiratory gating was performed is probably due to the influence of the respiratory cycle. Wåhlin *et al.* (*27*) also investigated the repeatability of net CSF flow measurements without respiratory gating, and found low ICC. They suggested this was caused by the relatively small aqueductal CSF flow with respect to the pulsatile CSF flow rates, and imperfect background correction. However, since no respiratory gating was performed, also respiratory effects may have contributed to this low ICC.

During inspiration we observed the highest inter-subject variation. Relatively large inter-subject differences can also be observed in the net CSF flow profiles in the aqueduct, for all respiratory conditions. The hydrodynamic theory by Greitz at al. (*30, 34*) states that stiffening of extracranial arterial vessel walls leads to larger expansion of intracerebral vessels over the cardiac cycle, thereby increasing CSF pulsatility. Furthermore, it has been shown that CSF pulsatility increases with age (*35*). Possibly respiration-induced CSF pulsatility also varies between subjects, similar to cardiac-induced CSF pulsatility.

Small variations between the aqueduct ROIs can be observed during inspiration gating, expiration gating, and without respiratory gating. These small variations of the aqueduct area had only a minor (non-significant) impact on the acquired net CSF flow, as the velocities at the edges are very low (data not shown). This may be (partly) due to motion between the different scans. Also, variations in background noise between the scans may play a role, since the ROIs are selected by including all voxels with a signal intensity significantly higher than the noise floor.

During the respiratory gated measurements a few outliers were observed. In one subject (subject 3) cranial net flow was found during expiration, and caudal flow was found during inspiration. The recorded physiology (cardiac and respiration) did not show striking irregularities. In this subject an irregular shape of the aqueduct was observed leading to local minor stenosis. The radiologist rated this as normal anatomical variation, but this may have led to non-laminar flow and, thus, to errors in the PC-MRI measurements. Furthermore, in two subjects similar (caudal) net CSF flows were observed during expiration and inspiration. In neither of these subjects irregularities were found in the anatomy or recorded physiology. It is uncertain to what extent these subjects indeed have less variability with respiration or whether unidentified measurement errors played a role.

There is currently a debate whether CSF is produced by the choroid plexus alone, but the main consensus is that CSF is produced mainly by the choroid plexus (*2, 36–38*). This work shows that net CSF flow measurements with PC-MRI are not

necessarily suitable as a marker for CSF production in the lateral ventricles, because of the considerable confounding influence of the respiratory cycle on these measurements.

Cranially directed net CSF flows have been found in communicating hydrocephalus by Hladky *et al.* (*37*). However, Schroth and Klose (*39*) observed net caudal CSF flow over one cardiac cycle using real-time MRI measurements in normal pressure hydrocephalus patients, although the CSF pulsation was found to be of higher amplitude. Also, Gideon *et al.* (*40*) found mostly caudal net CSF flows in normal pressure hydrocephalus patients. It could be that the reported reversed (cranial) net CSF flows, acquired with PC-MRI, were affected by altered CSF dynamics with respect to the respiratory cycle. Our results indicate that the effect size of respiration on net CSF flow measurements is sufficiently large to find reversed (cranial) net CSF flow over the cardiac cycle (**Figure 4**).

When respiration is taken into account, net CSF flow measurements may offer an interesting quantitative measure for CSF dynamics, and may be used to study differences between the healthy and diseased brain.

The major limitation of this work is the limited number of subjects, which makes it difficult to interpret the outliers in the measurements without respiratory gating. Also, no clinical patients were included. Therefore, it remains unknown if respiration also confounds net CSF flow measurements in diseased populations. If an MRI method for net CSF flows could be developed without confounding effects from respiration, it should be developed for field strengths widely available in the clinic (1.5T or 3T), as 7T MRI is still not widely available.

Furthermore, since only aqueductal CSF flow was measured, it was not possible to identify whether inter-individual differences in aqueductal CSF flow dynamics reflect differences in (intracranial) blood volume pulsation, or differences in the relative contributions of the ventricles and subarachnoidal space to compensate for blood volume pulsations. Therefore, in future work spinal measurements should be performed together with aqueductal CSF flow measurements.

Finally, no respiratory scheme was enforced. Therefore, a relatively large variation in respiratory patterns occurred, with deeper or more shallow breaths and faster or slower breaths, as compared with a fixed respiratory scheme, as used in literature (*13,21*). Regularizing the respiratory patterns by providing the subjects with a paced breathing cue may improve the consistency of the net CSF flow measurements

and, thus the confounding effects of respiration. This has to be evaluated in the future, and its performance may still be variable between different subjects and between patient groups.

Conclusion

The net CSF flow through the cerebral aqueduct was increased during expiration, and reversed (in cranial direction) during inspiration. When no respiratory gating was used, mostly caudal net CSF flow was found, except for two outliers. Repeatability was best for respiratory gating on inspiration, followed by gating on expiration. CSF stroke volume was not affected by respiration. A positive, significant association was found between stroke volume and net flow difference between inspiration and expiration. Since the measured net CSF flows are confounded considerably by the respiratory cycle, care should be taken in linking measured net CSF flows to CSF production.

References

1. N. A. Jessen, A. S. F. Munk, I. Lundgaard, M. Nedergaard, The glymphatic system: A beginner's guide. *Neurochem. Res.* 40, 2583–2599 (2015).
2. R. Spector, S. Robert Snodgrass, C. E. Johanson, A balanced view of the cerebrospinal fluid composition and functions: Focus on adult humans. *Exp. Neurol*. 273, 57–68 (2015).
3. C. May *et al.*, Cerebrospinal fluid production is reduced in healthy aging. *Neurology*. 40, 500–503 (1990).
4. S. Stoquart-ElSankari *et al.*, Aging effects on cerebral blood and cerebrospinal fluid flows. *J. Cereb. Blood Flow Metab.* 27, 1563–1572 (2007).
5. G. D. Silverberg *et al.*, The cerebrospinal fluid production rate is reduced in dementia of the Alzheimer's type. *Neurology*. 57, 1763–1766 (2001).
6. M. J. de Leon *et al.*, CSF clearance in Alzheimer Disease measured with dynamic PET. *J. Nucl. Med*., 1471–1476 (2017).
7. W. G. Bradley, CSF flow in the brain in the context of normal pressure hydrocephalus *AJNR. Am. J. Neuroradiol*. 36, 831–838 (2015).
8. D. A. Feinberg, A. S. Mark, Human brain motion and cerebrospinal fluid circulation demonstrated with MR velocity imaging. *Radiology.* 163, 793–799 (1987).
9. F. Ståhlberg *et al.*, A method for MR quantification of flow velocities in blood and CSF using interleaved gradient-echo pulse sequences. *Magn. Reson. Imaging*. 7, 655–667 (1989).
10. D. R. Enzmann, N. J. Pelc, Cerebrospinal fluid flow measured by phase-contrast cine MR. *AJNR Am J Neuroradiol.* 14, 1301–1307 (1993).
11. O. Balédent *et al.*, Relationship between cerebrospinal fluid and blood dynamics in healthy volunteers and patients with communicating hydrocephalus. I*nvest. Radiol.* 39, 45–55 (2004).
12. K. Yoshida *et al.*, Phase-contrast MR studies of CSF flow rate in the cerebral aqueduct and cervical subarachnoid space with correlation-based segmentation. *Magn. Reson. Med. Sci.* 8, 91–100 (2009).
13. S. Dreha-Kulaczewski *et al.*, Inspiration is the major regulator of human CSF flow. *J. Neurosci.* 35, 2485–2491 (2015).
14. L. Chen, A. Beckett, A. Verma, D. A. Feinberg, Dynamics of respiratory and cardiac CSF motion revealed with real-time simultaneous multi-slice EPI velocity phase contrast imaging. *Neuroimage*. 122, 281–287 (2015).
15. U. Klose, C. Strik, C. Kiefer, W. Grodd, Detection of a relation between respiration and CSF pulsation with an echoplanar technique. *J. Magn. Reson. Imaging.* 11, 438–444 (2000).
16. S. Yamada *et al.*, Influence of respiration on cerebrospinal fluid movement using magnetic resonance spin labeling. *Fluids Barriers CNS.* 10, 36–42 (2013).
17. J. M. Spijkerman *et al.*, in I*SMRM proceedings* (2017), p. 2849.
18. C. Nilsson *et al.*, Circadian variation in human cerebrospinal fluid production measured by magnetic resonance imaging. *Am. J. Physiol.* 262, R20–R24 (1992).
19. W. H. Bouvy *et al.*, Assessment of blood flow velocity and pulsatility in cerebral perforating arteries with 7-T quantitative flow MRI. *NMR Biomed*. 29, 1295–1304 (2016).
20. R. M. Goldstein, H. A. Zebker, C. L. Werner, Satellite radar interferometry: Two-dimensional phase unwrapping. *Radio Sci.* 23 (1988), pp. 713–720.

21. S. Dreha-Kulaczewski *et al.*, Identification of the upward movement of human CSF in vivo and its relation to the brain venous system. *J. Neurosci.* 37, 2395–2402 (2017).

22. K. Takizawa, M. Matsumae, S. Sunohara, S. Yatsushiro, K. Kuroda, Characterization of cardiac and respiratory-driven cerebrospinal fluid motion based on asynchronous phase-contrast magnetic resonance imaging in volunteers. *Fluids Barriers CNS.* 14, 1–8 (2017).

23. J. Daouk, R. Bouzerar, O. Baledent, Heart rate and respiration influence on macroscopic blood and CSF flows. *Acta radiol.* 58, 977–982 (2017).

24. S. Yildiz *et al.*, Quantifying the influence of respiration and cardiac pulsations on cerebrospinal fluid dynamics using real-time phase-contrast MRI. *J. Magn. Reson. Imaging*. 46, 431–439 (2017).

25. T.-Y. Huang *et al.*, Supratentorial cerebrospinal fluid production rate in healthy adults: Quantification with two-dimensional cine phase-contrast MR imaging with high temporal and spatial resolution. *Radiology.* 233, 603–608 (2004).

26. S. K. Piechnik, P. E. Summers, P. Jezzard, J. V. Byrne, Magnetic Resonance measurement of blood and CSF flow rates with phase contrast - Normal values, repeatability and CO2 reactivity. Acta Neurochir. Suppl., 263–270 (2008).

27. A. Wåhlin *et al.*, Phase contrast MRI quantification of pulsatile volumes of brain arteries, veins, and cerebrospinal fluids compartments: Repeatability and physiological interactions. *J. Magn. Reson. Imaging*. 35, 1055–1062 (2012).

28. S. Ragunathan, J. G. Pipe, Radiofrequency saturation induced bias in aqueductal cerebrospinal fluid flow quantification obtained using two-dimensional cine phase contrast magnetic resonance imaging. *Magn. Reson. Med.* 79, 2067–2076 (2018).

29. D. S. Kim, J. U. Choi, R. Huh, P. H. Yun, D. I. Kim, Quantitative assessment of cerebrospinal fluid hydrodynamics using a phase-contrast cine MR image in hydrocephalus. *Child's Nerv. Syst.* 15, 461–467 (1999).

30. G. A. Bateman, C. R. Levi, P. Schofield, Y. Wang, E. C. Lovett, The pathophysiology of the aqueduct stroke volume in normal pressure hydrocephalus: Can co-morbidity with other forms of dementia be excluded? *Neuroradiology*. 47, 741–748 (2005).

31. A. Rohatgi, *WebPlotDigitizer* (2017), (available at https://automeris.io/WebPlotDigitizer/).

32. B. Mokri, The Monro-Kellie hypothesis. *Neurology*. 56, 1746–1748 (2001).

33. O. Balédent, M.-C. C. Henry-Feugeas, I. Idy-Peretti, Cerebrospinal fluid dynamics and relation with blood flow. *Invest. Radiol.* 36, 368–377 (2001).

34. D. Greitz, J. Hannerz, T. Rahn, H. Bolander, A. Ericsson, MR imaging of cerebrospinal fluid dynamics in health and disease on the vascular pathogenesis of communicating hydrocephalus and benign intracranial hypertension. *Acta radiol.* 35, 204–211 (1994).

35. C. B. Beggs *et al.*, Aqueductal cerebrospinal fluid pulsatility in healthy individuals is affected by impaired cerebral venous outflow. *J. Magn. Reson. Imaging*. 40, 1215–1222 (2014).

36. D. Orešković, M. Radoš, M. Klarica, Role of choroid plexus in cerebrospinal fluid hydrodynamics. *Neuroscience.* 354, 69–86 (2017).

37. S. B. Hladky, M. A. Barrand, Mechanisms of fluid movement into, through and out of the brain: evaluation of the evidence. *Fluids Barriers CNS.* 11, 26–57 (2014).

38. S. B. Hladky, M. A. Barrand, Fluid and ion transfer across the blood–brain and blood–cerebrospinal fluid barriers; a comparative account of mechanisms and roles. *Fluids Barriers CNS.* 13, 19–87 (2016).

39. G. Schroth, U. Klose, Cerebrospinal fluid flow III. Pathological cerebrospinal fluid pulsations. Neuroradiology. 35, 16–24 (1992).

40. P. Gideon *et al.*, Cerebrospinal fluid flow and production in patients with normal pressure hydrocephalus studied by MRI. Neuroradiology. 36, 210–215 (1994).

Chapter 5

T_2 mapping of cerebrospinal fluid at 3T and 7T MRI

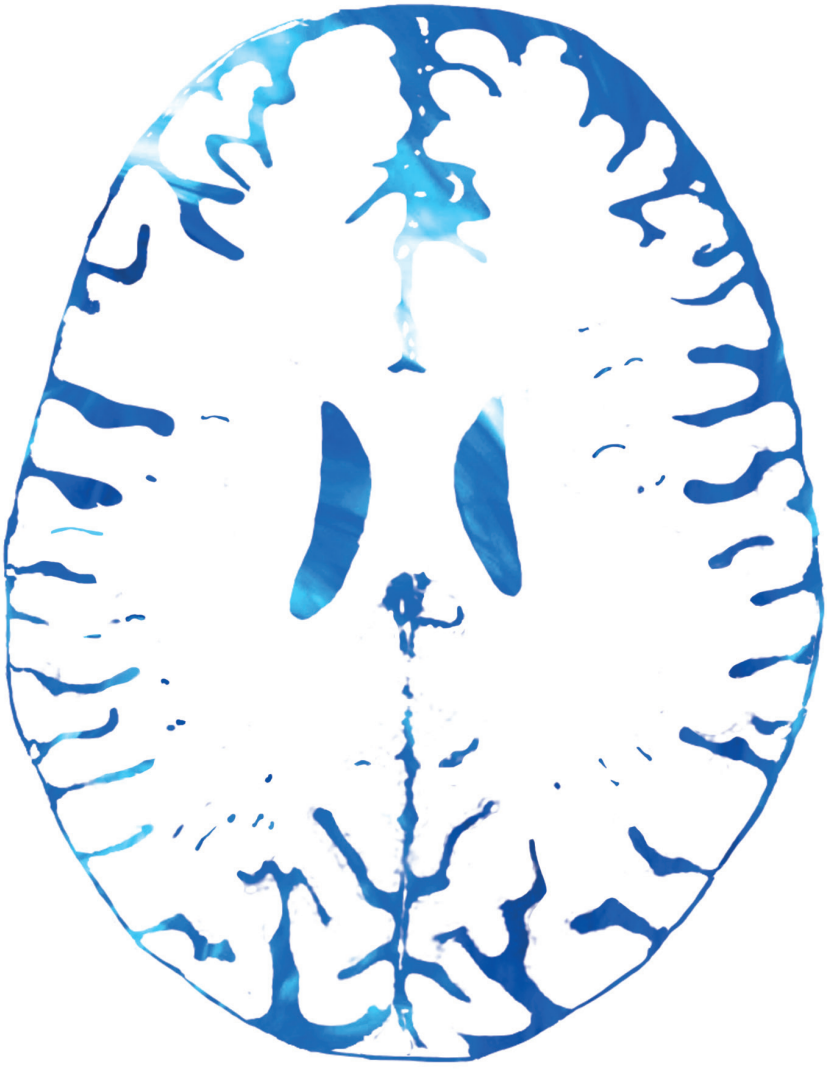

Jolanda M. Spijkerman, Esben T. Petersen,
Jeroen Hendrikse, Peter R. Luijten, Jaco J.M. Zwanenburg

Based on: Magnetic Resonance Materials in Physics, Biology and Medicine. 31, 415-424 (2018)

Abstract

Objective

CSF T_2 mapping can potentially be used to investigate CSF composition. A previously proposed CSF T_2-mapping method reported a T_2 difference between peripheral and ventricular cerebrospinal fluid (CSF), and suggested that this reflected different CSF compositions. We studied the performance of this method at 7T MRI and evaluated the influence of partial volume and B_1 and B_0 inhomogeneity.

Methods

T_2-preparation-based CSF T_2-mapping was performed in 7 healthy volunteers at 7T and 3T and was compared with a single echo spin-echo sequence with varying TEs. The influence of partial volume was assessed by analyzing the longest TEs only. B_1 and B_0 maps were acquired. B_1 and B_0 dependency of the sequences was tested using a phantom.

Results

$T_{2,CSF}$ was shorter at 7T compared to 3T. At 3T, but not at 7T, peripheral $T_{2,CSF}$ was significantly shorter than ventricular $T_{2,CSF}$. Partial volume contributed to this T_2 difference, but could not fully explain it. B_1 and B_0 inhomogeneity had only very limited effect. $T_{2,CSF}$ did not depend on the voxel size, probably due to the selection method of the regions-of-interest.

Conclusion

CSF T_2 mapping is feasible at 7T. The shorter peripheral $T_{2,CSF}$ is likely a combined effect of partial volume and CSF composition.

Introduction

In previous work by Qin (*1*) a fast method was proposed at 3T MRI to map the volume and T_2 of cerebrospinal fluid (CSF) in the brain. A striking finding with this method was the observation of a shorter T_2 of the peripheral CSF compared to the T_2 of the CSF in the lateral ventricles. The paper suggested that this T_2 difference is caused by differences in CSF composition between both areas, implying that CSF T_2 ($T_{2,CSF}$) can be used as a non-invasive biomarker for CSF composition. This would be highly relevant in the light of the recent attention for the clearance of brain waste products, in which CSF is involved (*2–5*). A method that can non-invasively assess CSF composition would provide a non-invasive window on the brain clearance system, with great potential for applications in studying diseases related to dementia such as Alzheimer's disease and cerebral small vessel disease. If $T_{2,CSF}$ indeed appears to be useful as functional marker of the brain clearance system, it could be studied next to other advanced imaging markers of early brain damage such as microbleeds, microinfarcts, and hippocampus subfield volumes and atrophy. As many of these advanced markers are acquired at 7T (*6–8*), it is desirable to implement and evaluate CSF T_2 mapping at 7T as well.

At 7T, B_1 inhomogeneity is considerable and may influence the T_2 mapping results, despite the relative B_1 insensitivity of the used CSF T_2 mapping method. Even at 3T, considerable B_1 inhomogeneity in the brain can be observed (*9*). Also, when measuring T_2 in peripheral CSF, partial volume effects with tissue cannot be avoided. So, we hypothesized that these partial volume effects and B_1 imperfections can explain the previously observed T_2 differences. De Vis, *et al.* (2015) (*10*) obtained a rough estimation of the influence of partial volume effects on the estimated $T_{2,CSF}$ by scanning with two different resolutions. The higher resolution resulted in longer T_2 times, indeed suggesting a role for partial volume effects. Because the influence of B_1 inhomogeneity and partial volume effects is not clear yet, it remains uncertain to what extent $T_{2,CSF}$ can be used to assess the composition of CSF.

In this work we studied the performance of Qin's CSF T_2 mapping method at 7T MRI. The specific goals were to investigate the influence of B_1 and B_0 imperfections on the estimated $T_{2,CSF}$, to assess the influence of partial volume effects, and to evaluate to what extent the previously observed difference in $T_{2,CSF}$ between periphery and ventricles can be explained from B_1, B_0, and partial volume effects. B_1 and B_0 sensitivity was investigated with phantom measurements, and by comparing the method between 7T and 3T MRI in healthy human subjects. Partial volume effects were estimated by removing the influence of partial volume with tissue, through selection of only the last (longest) TEs. Also different resolutions were scanned.

Methods

Sequence

The CSF T_2 mapping sequence used in this research is based on T_2 preparation, and has been described elsewhere (*1*, *10*). For this study the method has been further extended to improve the fit reliability of the long T_2 times by implementing longer refocusing pulse trains, yielding longer echo times. Briefly, the sequence consists of four parts (**Figure 1**). First, a set of four nonselective WET (Water suppression Enhanced through T_1 effects) pulses is applied for saturation, to prevent slice history effects. These pulses are optimized for saturation of free water (applicable for T_1 values between 3 – 6 s), the pulse angles are 156°, 71°, 109°, and 90° (*11*). Second, a delay time (T_{delay}) follows, where T_1 relaxation occurs, followed by crusher gradients.

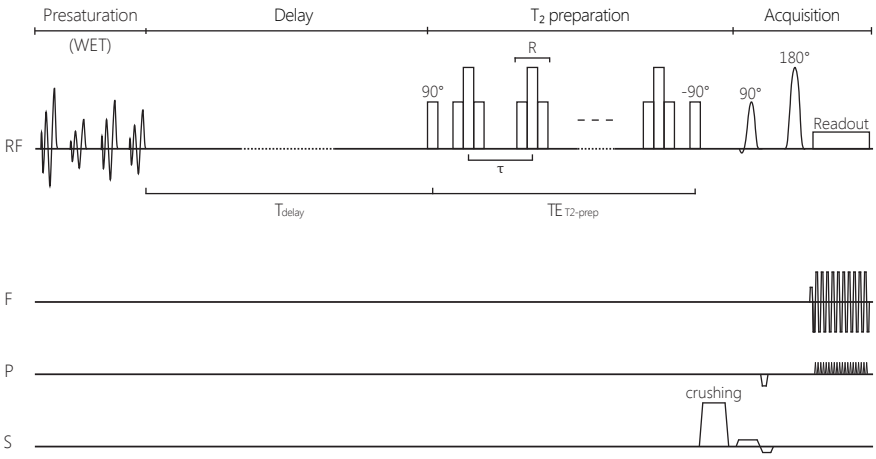

Figure 1 CSF T_2 mapping pulse sequence. The sequence consists of four parts: WET presaturation, a fixed delay with duration T_{delay}, a T_2 preparation module with MLEV phase cycling, and a SE-EPI image acquisition. To perform T_2 mapping the sequence was repeated, while increasing the number of refocusing pulses (and therefore $TE_{T2\text{-}prep}$) for a fixed inter-pulse delay τ. The applied RF pulses are shown on the RF axis, the applied gradients are shown on the frequency (F), phase (P), and slice (S) encoding axes.

Third, T_2 preparation is applied, consisting of a nonselective 90° pulse, a set of 4, 8, 16 or 32 non-selective refocusing pulses (R) according to the MLEV (Malcolm Levitt) phase cycling scheme, and a nonselective -90° pulse with a crusher gradient to crush any remaining transversal magnetization (*12*). Each refocusing pulse R is a

composite pulse, consisting of $90_x°$, $180_y°$, $90_x°$ rectangular pulses (or the inverse : $90_{-x}°$, $180_{-y}°$, $90_{-x}°$). The duration of a single refocusing pulse was 2.6 ms. T_2 relaxation occurs during $TE_{T2\text{-}prep}$, which is determined by the number of refocusing pulses and the spacing between the centers of the refocusing pulses (τ). To achieve long $TE_{T2\text{-}prep}$s, τ was chosen at 150 ms. This resulted in $TE_{T2\text{-}prep}$ durations of 600, 1200, 2400, and 4800 ms. Also one scan was acquired without any refocusing pulses; this scan was not used in data analysis. The fourth part of the sequence is a single shot 2D SE-EPI readout. During the EPI train also T_2 decay occurs; this can however be regarded as a constant factor, and was therefore neglected in the analysis.

Although the refocusing train in the T_2 preparation is relatively insensitive to B_1 inhomogeneities due to the MLEV phase cycling scheme, the 90° rectangular pulses before and after the train may fail in case of B_1 deviations. Consequently, we hypothesized that a fraction of the magnetization may be unaffected by the T_2-preparation module, which could have a relatively large impact on the measured signal in case of partial volume effects. Also, in case of imperfect B_1, T_1-weighted stimulated echoes may influence the T_2 measurements, although this effect is expected to be relatively small due to the long T_1 of CSF (4.4 s (*13*)). Therefore, T_2 mapping with a single echo SE-EPI sequence with various TEs was used as truly B_1 insensitive reference (shown in supplemental material).

Nonselective pulses were used where possible to minimize motion sensitivity. Consequently, only the excitation pulse of the SE-EPI readout was selective.

Phantom measurements

Phantom measurements were performed to test the B_1 and B_0 sensitivity. The experiments were performed on a 7T Philips Achieva scanner (Philips Medical Systems, Best, The Netherlands) with a 32-channel head coil (Nova Medical, Wilmington, MA, USA), with a tap water phantom at room temperature. Phantom size was 200×95×20 mm^3. The phantom was scanned with equal echo times as used for the in vivo experiments. A single slice was acquired with 3×3×6 mm^3 resolution, FOV 240×96 mm^2, T_{delay} of 15 s, (which is more than 3 times the T_1 of CSF (4.4 s (*13*))), and sensitivity encoding (SENSE) (*14*) (with SENSE factor 1, meaning that the coil sensitivities of the receive coils were used for optimal coil combination without imaging acceleration). A series of T_2 maps with increasing through-plane B_0 gradients was acquired to study the effect of diffusion for B_1 100%. The following through-plane B_0 gradient strengths were applied by adding this strength to the linear shim term in the user interface: 0, 0.05, 0.1, 0.2, 0.3, and 0.5 mT/m. The phantom appeared sensitive to free induction decay (FID) artifacts, due to the

relatively large volume of water and more pronounced B_1 inhomogeneity (*15*). The acquisition with the highest B_0 gradient yielded images free of FID artifacts, which allowed to study the B_1 dependency of the CSF T_2 mapping sequence. B_0 and B_1 maps were acquired, using identical resolution and FOV as the T_2 mapping acquisitions. The B_0 map was obtained with a gradient echo sequence with two different TEs (1.64 and 2.64 ms). The B_1 mapping sequence was based on the actual flip angle method (*16*), with $TR_1/TR_2/TE$ equal to 40/160/0.96 ms, and a flip angle of 50 degrees.

In vivo measurements

In vivo experiments were performed at both 7T and 3T to test the feasibility of CSF T_2 mapping at 7T, to further assess the sensitivity to B_1 inhomogeneities, and to explore the influence of partial volume effects. Seven healthy volunteers (3 male, age range 21 – 54 years, mean age 34 years) participated in this study. Informed consent was given by all subjects in accordance to the Institutional Review Board of the University Medical Center Utrecht (Utrecht, The Netherlands). All volunteers were scanned at both a 3T Philips Achieva scanner with an 8-channel head coil (Philips Healthcare, Best, The Netherlands), and the 7T scanner that was also used for the phantom study. The CSF T_2 mapping scans were acquired in a single coronal slice, planned through both the lateral ventricles and the fourth ventricle (**Figure 2A**). The scanning parameters are summarized in **Table 1**. The fixed T_{delay} was 15 s and TR varied between 20 – 25 s, depending on $TE_{T2\text{-}prep}$. Other parameters were: SENSE factor 2.3 in left-right direction, FOV 240×240 mm^2. Due to the long TR, SAR remained well within the SAR limits, also at 7T. No additional methods were used to correct for eddy currents. The low bandwidth of the scan may cause distortions in areas with poor shimming, such as the nasal cavities. However, shimming was good in the selected coronal slice. Also B_0 and B_1 maps were acquired.

Data analysis

Phantom

The resulting T_2 estimates were analyzed as a function of B_1 and B_0. B_1 sensitivity was assessed using the scans with the highest B_0 gradient strength (0.5 mT/m), where no FID artifacts were present. The B_1 range present in the scan was used. Based on the B_1 in each voxel, the voxels were sorted over 8 bins of 5% B_1, leading to B_1 bins ranging from 85±2.5% to 120±2.5%. The signal was averaged over each B_1 bin, and T_2 times were fitted over this averaged signal. B_0 sensitivity was assessed using the varying applied B_0 gradient strengths (0, 0.05, 0.1, 0.2, 0.3, and 0.5 mT/m). In

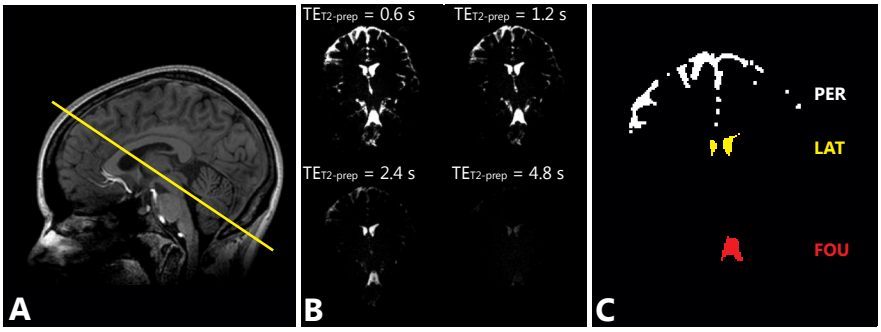

Figure 2 Planning of the CSF T_2 mapping scans, through the lateral ventricles and the fourth ventricle (A), the CSF T_2 mapping scans at 7T for increasing $TE_{T2\text{-}prep}$ ($TE_{T2\text{-}prep}$ is 0.6s, 1.2s, 2.4s, 4.8s), shown with equal intensity scaling (B), and the used ROI masks of the periphery (white), the lateral ventricles (yellow), and the fourth ventricle (red) (C).

Table 1. Scan parameters used for the in vivo experiments for the CSF T_2 mapping sequence (based on T_2-preparation).

	Resolution	$TE_{readout}$ [ms]	$TE_{T2\text{-}prep}$ [ms]	EPI factor	BW (phase/freq) [Hz/voxel]	Scan dur. [min]
3T	1×1×4	133	0 – 4800 [1]	105	8.1 / 961	2:59
	3×3×6	42	0 – 4800 [1]	67	28.2 / 2308	2:59
7T	1×1×2	127	0 – 4800 [1]	107	8.4 / 1082	3:04
	1×1×4	126	0 – 4800 [1]	107	8.4 / 1082	3:04
	3×3×6	23	0 – 4800 [1]	37	55.1 / 2642	3:04

[1] The used $TE_{T2\text{-}prep}$s were: 0, 600, 1200, 2400, 4800 ms

each scan only voxels with B_1 between 97.5 – 102.5% were included. An additional intensity threshold was applied on the scan with the longest $TE_{T2\text{-}prep}$, to minimize the influence of artifacts in the lower B_0 gradient scans. This threshold was set at 75% of the maximum intensity for the longest TE. The signal of all included voxels was averaged over each scan, and T_2 times were fitted over this averaged signal.

In vivo

Three regions of interest (ROI) were defined on the acquired in vivo scans: the lateral ventricles, the fourth ventricle and peripheral CSF. The ROI masks were made by applying an intensity threshold to the first echo time ($TE_{T2\text{-}prep}$ = 0.6 s). The intensity threshold was set at 25% of the maximum intensity in the image.

Figure 2BC shows the acquired CSF T_2 mapping scan at 7T with resolution 1×1×4 mm^3 at all echo times for one volunteer, and the used ROIs. Conservative ROIs were used in the ventricles by eroding the intensity based ROIs with one voxel, to minimize both partial volume and motion sensitivity. Erosion of the peripheral ROIs was not feasible.

The signal was averaged over each ROI, and T_2 times were fitted over this averaged signal, using a single exponential decay model. Also mean B_0 and B_1 values were determined for each ROI. In order to minimize the influence of e.g. motion or partial volume effects on the data analysis, only fit results with an R^2 of 0.99 or higher were considered.

Partial volume assessment

In the peripheral CSF an additional assessment of the influence of partial volume was made, by performing a partial volume correction. Only $TE_{T2\text{-}prep}$s of minimally 1200 ms (excluding the shortest $TE_{T2\text{-}prep}$ of 600 ms) were taken into account in the analysis. Thereby, maximal nulling of e.g. tissue signal was achieved, since the T_2 times of tissue are below 100 ms (*17*, *18*), which is about 10 times shorter than the shortest $TE_{T2\text{-}prep}$ used. The analysis with only the last $TE_{T2\text{-}prep}$s was also performed on the phantom scans to check for any systematic errors, for all applied B_0 gradient strengths and B_1 between 97.5 – 102.5%.

All data analyses were performed in Matlab (version 2015B, Mathworks, Natick, MA, USA). IBM SPSS (version 21.0) was used for statistical analysis. Median $T_{2,CSF}$ values and full ranges are reported. Wilcoxon signed-rank tests (significance level $p<0.05$) were used to compare CSF T_2 times in the lateral and fourth ventricles with the periphery to explore the observed T_2 differences.

Results

Phantom measurements

Figure 3 shows the results of the phantom measurements for the B_1 dependency (**Figure 3A**) and B_0 gradient dependency (**Figure 3B**). The CSF T_2 mapping sequence resulted in a T_2 time of 1.71 s (95% confidence interval (CI): 1.66 – 1.76 s) for B_1 of 100±2.5% and B_0 gradient strength of 0 mT/m. The sequence showed only minor B_1 sensitivity (assessed in the scans with B_0 gradient strength of 0.5 mT/m), with T_2 times ranging from 1.41 s (95% CI: 1.38 – 1.43 s) at B_1 of 85±2.5% to 1.49 s (95% CI: 1.40 – 1.57 s) at B_1 of 105±2.5%. Also minor B_0 gradient dependency was observed.

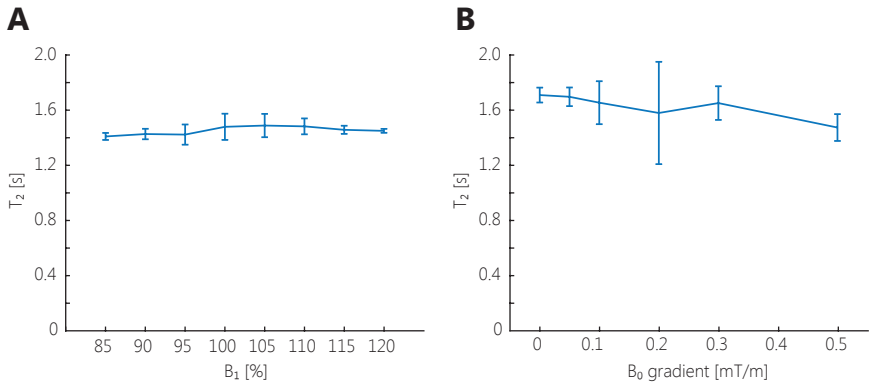

Figure 3 Results of the phantom measurements for the B_1 (A) and B_0 gradient dependency (B), showing the fitted T_2 times for different B_1s and through-plane B_0 gradient strengths, respectively. The error bars show the 95% confidence interval of the fitted T_2 times. The CSF T_2 mapping sequence shows only minor sensitivity to B_1 and to the through-plane B_0 gradient, (and, thus, to diffusion). The effect of the B_0 gradient was most apparent for the highest B_0 gradient. The B_1 dependency was determined with a B_0 gradient strength of 0.5 mT/m to avoid FID artifacts in regions with B_1 deviating from 100%. For B_0 gradient 0.2 mT/m the confidence interval was larger, this was due to FID artefacts.

In vivo measurements

A total of 35 CSF T_2 mapping scans was acquired, for both field strengths, and the different resolutions. Per scan 3 fits were made, one per ROI, resulting in a total of 105 fits (42 at 3T, 63 at 7T). Based on the strict requirement on minimum R^2, 14 fits were excluded (4 at 3T, 10 at 7T), which is 13% of the total number of fits (10% at 3T, 16% at 7T), see **Table 2** for a detailed overview.

The in vivo results for the scans with resolution 1×1×4 mm^3 are summarized in **Figure 4**. The results for the other resolutions were not significantly different from the data shown here (all data are shown in **Tables S3, S4, and S5** in the supplemental material). Although T_2 differences between the resolutions were not significant, in most cases the shortest T_2 times were observed for the largest voxel sizes.

At 7T significantly shorter T_2 times were found compared to 3T. At 3T the T_2 times measured in the periphery were significantly shorter compared to the lateral and fourth ventricles. The T_2 times measured at 7T were not significantly different between the three ROIs. At 3T, the median B_1 in the periphery was 85% (range: 79 – 90%), while in the lateral and fourth ventricles B_1 was 109% (ranges: 106 – 112% and 103 – 114%). The median B_0 gradient in the periphery was 0.13 mT/m (range: 0.07 – 0.38 mT/m), while in the lateral and fourth ventricles the median B_0 gradients

Table 2. Number of excluded fits

		Scans (fits)	Excluded fits		
			Lateral ventricles	Fourth ventricle	Periphery
3T	1×1×4	7 (21)	0	1	0
	3×3×6	7 (21)	2	1	0
Total		*14 (42)*	*2*	*2*	*0*
7T	1×1×2	7 (21)	0	1	0
	1×1×4	7 (21)	1	3	0
	3×3×6	7 (21)	1	4	0
Total		*21 (63)*	*2*	*8*	*0*

Number of acquired scans and performed T_2 fits, and the number of excluded T_2 fits per ROI.

were 0.02 mT/m and 0.03 mT/m, respectively (ranges: 0.02 – 0.06 mT/m and 0.01 – 0.03 mT/m). At 7T lower B_1 values in the periphery and the fourth ventricle were observed (median 86% (range: 75 – 94%) and 93% (range: 62 – 101%), respectively), and higher B_1 in the lateral ventricles (median 111% (range (109 – 116)). Similar B_0 gradients were observed in the three ROIs (median 0.07 mT/m (range (0.03 – 0.10 mT/m), 0.06 mT/m (range (0.04 – 0.08 mT/m), and 0.06 mT/m (range: 0.05 – 0.09 mT/m), for the lateral ventricles, the fourth ventricle, and the periphery, respectively).

Partial volume assessment

Figure 5 shows the results for the additional analysis of peripheral CSF to assess the influence of partial volume. The partial volume correction resulted in longer T_2 times, with an increase of 118 ms at both 3T and 7T. This T_2 increase was significant at 7T. At 7T the corrected peripheral CSF T_2 was quite similar to the ventricular T_2 (1.01 vs 1.05 s), while at 3T the mean peripheral T_2 was still approximately 200 ms shorter than the ventricular T_2 times (1.79 s (range 1.49 – 1.82 s) vs 2.03 s (range 1.73 – 2.16 s), $p = 0.02$). The results for this analysis of the phantom data is shown in **Figure 6**. Both analysis methods (including all TEs or only the longest TEs) resulted in similar T_2 times, indicating no systematic errors in the additional analysis with only the longest TEs.

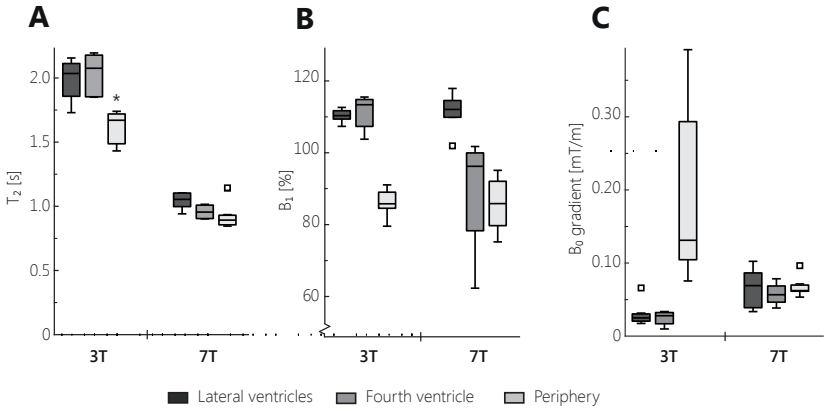

Figure 4 In vivo results: T_2 (A), B_1 (B), and B_0 gradient (C) values for the three different ROIs. Outliers are represented by a square symbol. Significant differences in measured T_2 were found between the periphery and the lateral and fourth ventricles at 3T (indicated using the asterisk symbol).

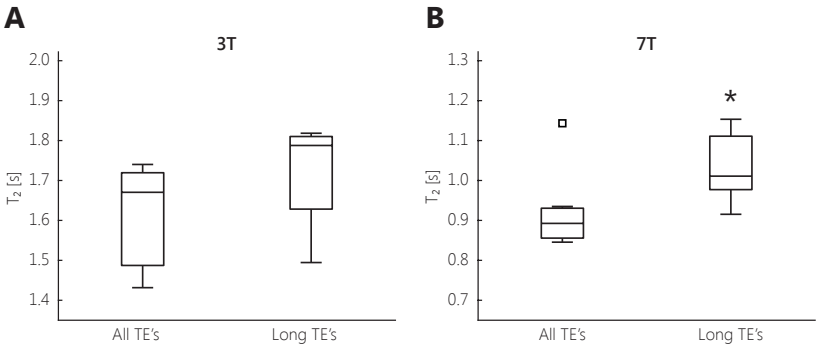

Figure 5 T_2 times of peripheral CSF, resulting from the use of only the longest TEs, compared with the original analysis, at 3T (A) and at 7T (B). Outliers are represented by a square symbol. At both 3T and 7T an increase in T_2 can be observed. The asterisk symbol indicates a significant difference with the original analysis (including all TEs).

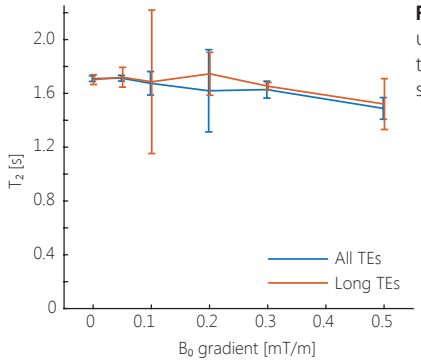

Figure 6 T_2 times of the phantom, resulting from the use of only the longest TEs (orange), compared with the original analysis (blue). Both analyses result in similar T_2 times.

Discussion

In this research we have shown the feasibility of CSF T_2 mapping at 7T with a dedicated CSF T_2 mapping sequence based on T_2 preparation, which was initially developed at 3T. We investigated the sensitivity of this sequence for the influence of B_1, diffusion (B_0 gradient), and partial volume effects. The sequence appeared to be relatively insensitive to B_1 and B_0 inhomogeneity. Partial volume effects tend to lower the observed T_2 times at the periphery. $T_{2,CSF}$ was considerably shorter at 7T compared to 3T in all three ROIs. The peripheral $T_{2,CSF}$ was significantly shorter than the ventricular $T_{2,CSF}$ at 3T (but not at 7T).

The peripheral $T_{2,CSF}$ increased considerably upon partial volume correction, as obtained from the analysis with only long TEs (>10 times tissue T_2). The partial volume correction for the SE-EPI sequence, which was used as relatively B_1-insensitive reference (data shown in supplement), did not significantly increase the T_2 times, although the SE-EPI sequence showed an even larger T_2 difference between the periphery and ventricles. The ventricular T_2 times measured with the CSF T_2 mapping sequence at 3T match with T_2 times found in literature (*1*, *10*, *19*, *20*). Given our results, we believe that the observed T_2 difference between the ventricular and peripheral CSF could be partly due to physiological differences. However, the different results for different sequences and field strengths and the confounding influence of partial volume will make it challenging to accurately isolate and quantify any true physiological effect from confounders. This will hamper applications in research focusing on in vivo evaluation of the (regional) composition of CSF.

In the phantom measurements only minor B_1 dependency was found for the CSF T_2 mapping sequence, as shown in **Figure 3A**. Also, the measurements with an increasing through-plane B_0 gradient showed only limited B_0 gradient dependency, except for the highest B_0 gradient (0.5 mT/m), as shown in **Figure 3B**. In the in vivo measurements the B_0 gradient was similar between the periphery and the ventricles at 7T, and differed by maximally 0.38 mT/m (median B_0 gradient was 0.13 mT/m) at 3T (shown in **Figure 4C**). This difference in B_0 homogeneity between 3T and 7T is probably due to different shimming techniques: image based third order shimming was used at 7T, and linear shimming was used at 3T. The low sensitivity to B_0 gradient shows that the T_2 mapping sequence is relatively insensitive to diffusion. It is not likely that B_0 gradients due to imperfect shimming contributed considerably to the observed difference in T_2 between periphery and ventricles.

The different resolutions used at both field strengths did not yield considerably different T_2 times (shown in **Tables S3-S5** in the supplemental material), although there is a trend of longer measured ventricular T_2 times for smaller voxel sizes at 3T, similar to De Vis, *et al.* (2015) (*10*). As the ventricular ROIs were eroded, the voxels at the edges, where more partial volume is expected, were discarded. For the periphery however, erosion was not feasible due to the thin ROI shape. Moreover, the ROI definition was based on an intensity threshold, which depends on the CSF fraction in each voxel. Since the total subarachnoidal CSF volume is quite small, and distributed over a relatively large area (*21*), partial volume is probably present in all peripheral ROIs, independent of the voxel sizes used in this work.

The role of partial volume effects regarding the measured peripheral $T_{2,CSF}$ was investigated by using the longest TEs only (**Figure 5**), to maximally remove the influence of partial volume. It could seem unexpected that the use of the late TEs reveals considerable partial volume effect, since the first $TE_{T2\text{-}prep}$ is already relatively long compared with the tissue T_2. The T_2 of grey matter is approximately 90 ms at 3T (*18*, *22*) and 55 ms at 7T (*18*, *23*), while the first TE was 600 ms. However, it is possible that partial volume occurs with a compartment with a relatively long T_2 at the cerebral cortex, like arterial blood (T_2 around 150 ms at 3T (*24*, *25*)) or the outer rim of the cortex (unknown but long T_2 (>100 ms) at 7T (*26*)). At the shortest TE_{T2prep} (600 ms), the signal of arterial blood has decayed to 2%. However, in case of small partial volume fractions of CSF in the periphery, this could still have a considerable influence on the measured T_2. The outer layer of the cerebral cortex (layer I) may have a long T_2 due to the fact that it contains almost no neuronal cell bodies, and many glial cells instead, similar to gliotic lesions, which also have a long T_2 (*26*).

De Vis *et al.* (*10*) found a T_2 difference of 609±133 ms between the periphery and the ventricles at 3T, Qin found a T_2 difference of 420±155 ms at 3T. Also in this work a shorter $T_{2,CSF}$ was measured in the periphery compared with the ventricles, as shown in **Figure 4A**. This T_2 difference is larger at 3T compared with 7T: the T_2 difference is 365 ms at 3T, and 161 ms at 7T, which is 18% and 15% relative to the T_2 in the lateral ventricles, for 3T and 7T respectively. Partial volume correction, which led to a peripheral CSF T_2 increase of 118 ms at both field strengths (**Figure 5**), resulted in remaining T_2 differences of 247 and only 43 ms for 3T and 7T, respectively. This is a T_2 difference of 12% and 4% relative to the ventricular CSF T_2 for 3T and 7T, respectively. A relatively larger T_2 difference was found when a SE-EPI sequence was used, which remained largely unchanged after partial volume correction (data shown in supplement).

These results indicate a true T_2 difference between peripheral and ventricular CSF. A potential physiological explanation for this observed T_2 difference could be sought in differences in e.g. O_2, protein, and/or glucose levels, since these substrates are known to decrease T_2 (*20*, *27–29*). However, relatively large concentration differences are necessary to bridge the difference between peripheral and ventricular $T_{2,CSF}$. So although differences in CSF composition may partly cause the observed T_2 difference, it seems unlikely that this is the only contributor.

The shorter in vivo CSF T_2 at 7T compared to 3T (**Figure 4A**), is in line with published in vivo measurements by Daoust *et al.* (*20*). However, Daoust suggested that the T_2 of CSF is not field strength dependent, but that residual field gradients cause errors in in vivo measurements at higher field strengths. If the T_2 measurements are strongly dependent on residual gradients, one might expect that the T_2 difference between periphery and ventricles observed at 3T is also largely due to residual field gradients, such as B_0 gradients. However, the CSF T_2 mapping sequence used in our study showed negligible B_0 gradient dependency for the measured T_2 up to and including 0.3 mT/m, while the observed B_0 gradients in the brain were between 0.07 – 0.38 mT/m, and on average well below 0.20 mT/m. The limited diffusion sensitivity of the CSF T_2 mapping sequence is also visible from the results of the long TE analysis on the phantom measurements. The measured T_2 remained unchanged when only long TEs (with stronger diffusion weighting) was used (see **Figure 6**).

Before CSF T_2 mapping can be used as a parameter to study diseases such as cerebral Small Vessel Disease, several uncertainties need to be resolved. It is not yet clear to what extent the T_2 difference between ventricular and peripheral CSF reflects physiological differences in CSF composition. The CSF T_2 mapping sequence shows a much smaller T_2 difference compared with SE-EPI, while the difference also varies with field strength. Overall, the T_2 difference between peripheral and ventricular CSF could (partly) be explained by (a combination of) physiological differences. The possibility that the shorter peripheral T_2 is entirely caused by an artefact, like B_0 gradients caused by imperfect shimming and/or partial volume effects between tissue, blood, and CSF, seems unlikely.

Care should be taken when interpreting T_2 measurements of CSF, and more work is necessary to find the true explanations for the T_2 differences between 3T and 7T and between the peripheral and ventricular CSF at 3T.

The major limitation of this work is that it is an observational study, which limits the extent to which underlying mechanisms causing the observations can be

identified. Despite the efforts to separate the effects of partial volume and true physiological differences, it remains uncertain to what extent the observed shorter peripheral $T_{2,CSF}$ is due to different CSF compositions.

Furthermore, the statistical power of this study was limited by the small number of subjects combined with the stringent R^2 criterion, which resulted in a relatively large dropout of ROIs.

Moreover, only macroscopic B_0 gradients could be determined in the in vivo scans, and the magnitude of microscopic, subvoxel B_0 gradients remains unknown.

Finally, no in vitro CSF sample was used to validate the in vivo measurements. In vitro CSF is prone to changes in e.g. O_2 content compared with in vivo CSF, which may induce T_2 differences between in vitro and in vivo CSF.

Conclusion

CSF T_2 mapping with a dedicated sequence is feasible at both 3T and 7T, and yields shorter CSF T_2 times at 7T compared to 3T. At 3T shorter T_2 times were found for peripheral CSF compared to ventricular CSF, at 7T this effect was much smaller. Partial volume effects can partly explain this T_2 difference, but a physiological contribution to the difference in T_2 between ventricular and peripheral CSF is possible. The different results between different sequences and field strengths, and the confounding influence of partial volume, will make it challenging to accurately isolate and quantify any true physiological effect for applications in research focusing on in vivo evaluation of the (regional) composition of CSF.

References

1. Q. Qin, A simple approach for three-dimensional mapping of baseline cerebrospinal fluid volume fraction. *Magn Reson Med.* 65, 385–391 (2011).
2. J. J. Iliff et al., A paravascular pathway facilitates CSF flow through the brain parenchyma and the clearance of interstitial solutes, including amyloid β. Sci. Transl. Med., 4, 147ra111 (2012).
3. J. J. Iliff, M. Nedergaard, Is there a cerebral lymphatic system? *Stroke*. 44, 2013–2016 (2013).
4. L. Xie *et al.*, Sleep drives metabolite clearance from the adult brain. *Science*. 342, 373–377 (2013).
5. R. Spector, S. Robert Snodgrass, C. E. Johanson, A balanced view of the cerebrospinal fluid composition and functions: Focus on adult humans. *Exp. Neurol.* 273, 57–68 (2015).
6. J. De Bresser *et al.*, Visual cerebral microbleed detection on 7T MR imaging: Reliability and effects of image processing. *Am. J. Neuroradiol.* 34, E61–E64 (2013).
7. S. J. van Veluw, G. J. Biessels, P. R. Luijten, J. J. M. Zwanenburg, Assessing cortical cerebral microinfarcts on high resolution MR images. *J. Vis. Exp.,* e53125 (2015).
8. L. E. M. Wisse *et al.*, Hippocampal subfield volumes at 7T in early Alzheimer's disease and normal aging. *Neurobiol. Aging.* 35, 2039–2045 (2014).
9. S. Saekho, F. E. Boada, D. C. Noll, V. A. Stenger, Small tip angle three-dimensional tailored radiofrequency slab-select pulse for reduced B_1 inhomogeneity at 3 T. *Magn. Reson. Med.* 53, 479–484 (2005).
10. J. B. de Vis *et al.*, Cerebrospinal fluid volumetric MRI mapping as a simple measurement for evaluating brain atrophy. *Eur. Radiol*. 26, 1254–1262 (2015).
11. X. Golay, E. T. Petersen, F. Hui, Pulsed Star Labeling of Arterial Regions (PULSAR): A robust regional perfusion technique for high field imaging. *Magn. Reson. Med*. 53, 15–21 (2005).
12. M. H. Levitt, R. Freeman, T. Frenkiel, Broadband heteronuclear decoupling. *J. Magn. Reson.* 47, 328–330 (1982).
13. W. D. Rooney *et al.*, Magnetic field and tissue dependencies of human brain longitudinal ^1H_2O relaxation *in vivo. Magn Reson Med.* 57, 308–318 (2007).
14. K. P. Pruessmann *et al.*, SENSE: sensitivity encoding for fast MRI. *Magn. Reson. Med.* 42, 952–962 (1999).
15. B. M. Dale, M. A. Brown, R. C. Semelka, MRI Basic principles and applications (John Wiley & Sons Inc, Fifth edit., 2015).
16. V. L. Yarnykh, Actual flip-angle imaging in the pulsed steady state: A method for rapid three-dimensional mapping of the transmitted radiofrequency field. *Magn. Reson. Med.* 57, 192–200 (2007).
17. A. MacKay *et al.*, Insights into brain microstructure from the T_2 distribution. *Magn. Reson. Imaging.* 24, 515–525 (2006).
18. E. Cox, P. Gowland, in *Proc. Intl. Soc. Mag. Reson. Med.* (2008), p. 1411.
19. K. P. Whittall *et al.*, In vivo measurement of T_2 distributions and water contents in normal human brain. *Magn. Reson. Med.* 37, 34–43 (1997).
20. A. Daoust *et al.*, Transverse relaxation of cerebrospinal fluid depends on glucose concentration. *Magn. Reson. Imaging.* 44, 72–81 (2017).

21. S. Yamada, M. Ishikawa, K. Yamamot, Optimal diagnostic indices for idiopathic normal pressure hydrocephalus based on the 3D quantitative volumetric analysis for the cerebral ventricle and subarachnoid space. *Am. J. Neuroradiol.* 36, 2262–2269 (2015).

22. G. J. Stanisz *et al.*, T_1, T_2 relaxation and magnetization transfer in tissue at 3T. *Magn. Reson. Med*. 54, 507–512 (2005).

23. F. Visser, J. J. M. Zwanenburg, J. M. Hoogduin, P. R. Luijten, High-resolution magnetization-prepared 3D-FLAIR imaging at 7.0 tesla. *Magn. Reson. Med.* 64, 194–202 (2010).

24. J. J. Chen, G. B. Pike, Human whole blood T_2 relaxometry at 3 tesla. *Magn. Reson. Med.* 61, 249–254 (2009).

25. L. C. Krishnamurthy *et al.*, Dependence of blood T_2 on oxygenation at 7 T: In vitro calibration and in vivo application. *Magn. Reson. Med.* 71, 2035–2042 (2014).

26. S. J. van Veluw *et al.*, FLAIR images at 7 tesla MRI highlight the ependyma and the outer layers of the cerebral cortex. *Neuroimage.* 104, 100–109 (2015).

27. A. L. Hopkins, H. N. Yeung, C. B. Bratton, Multiple field strength in vivo T1 and T2 for cerebrospinal fluid protons. *Magn. Reson. Med.* 3, 303–11 (1986).

28. A. Yilmaz, F. Ş. Ulak, M. S. Batun, Proton T_1 and T_2 relaxivities of serum proteins. *Magn. Reson. Imaging.* 22, 683–688 (2004).

29. N. N. Yadav *et al.*, Natural D-glucose as a biodegradable MRI relaxation agent. *Magn. Reson. Med.* 72, 823–828 (2014).

Supplemental material

T_2 mapping with a single echo SE-EPI sequence with various TEs as truly B_1 insensitive reference for the CSF T_2 mapping sequence

Methods

SE-EPI sequence

As a reference for the CSF T_2 mapping method a single echo SE-EPI sequence was used that is equal to the readout in the CSF T_2 mapping sequence, but with increasing (very) long TEs (**Figure S1**). Crushers were applied before and after the refocusing pulse to crush the free induction decay signal from the refocusing pulse in case of an imperfect 180° pulse (inhomogeneous B_1). To minimize motion sensitivity, some modifications were made: the slice rewinder gradient was applied directly after the slice excitation pulse, while the phase encoding gradient was applied just prior to the EPI readout train. The motion sensitivity of the crusher

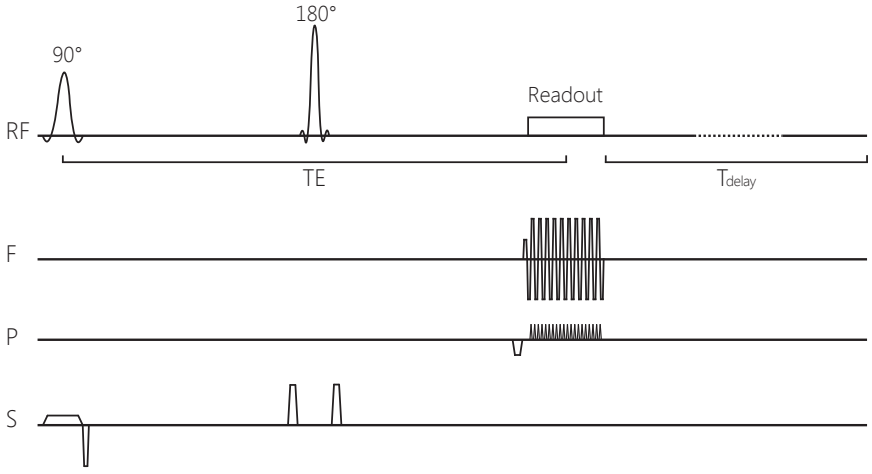

Figure S1 Single echo SE-EPI pulse sequence. For T_2 mapping, the echo time TE was varied. The applied RF pulses are shown on the RF axis, the applied gradients are shown on the frequency (F), phase (P), and slice (S) encoding axes.

gradients around the 180° refocusing pulse is limited, due the relatively slow flow of CSF (around 2 – 4 mm/s (*1*)) and the short spacing between both crusher lobes. The shortest TE used was aimed to be shorter than the first non-zero TE for the CSF T_2 mapping sequence, since the SE-EPI sequence has a higher diffusion sensitivity.

The longest TE was aimed to be in the same range as the longest TE for the CSF T_2 mapping sequence. Therefore the TEs were heuristically defined according to the following formula: $TE = 240 + 45 \cdot n^2$, for the n^{th} acquisition. This resulted in the following TEs: 240, 285, 420, 645, 960, 1365, 1860, 3120, 3885, and 4740 ms. After the readout a fixed delay time (T_{delay}) was applied. The other parameters are specified at the description of the in vivo measurements.

Phantom experiment

A single slice was acquired with 3×3×6 mm^3 resolution, FOV 240×96 mm^2, sensitivity encoding (SENSE) (*2*) factor 1, and TR of 15 s, resulting in T_{delay} of 14.7 s. A series of T_2 maps with increasing through-plane B_0 gradients was acquired to study the effect of diffusion for both sequences for B_1 100%. The following through-plane B_0 gradient strengths were applied by adding this strength to the linear shim term in the user interface: 0, 0.05, 0.1, 0.2, 0.3, and 0.5 mT/m. The acquisition with the highest B_0 gradient was used to study the B_1 dependency of the SE-EPI sequence, similar to the CSF T_2 mapping sequence.

In vivo experiment

The SE-EPI scan was acquired in all seven volunteers, in a single coronal slice (identical slice as the CSF T_2 mapping sequence). The scanning parameters are summarized in **Table S1**. Shared parameters were: SENSE factor 2.3 in left-right direction, FOV 240×240 mm^2. The fixed T_{delay} after image acquisition was 14.7 s and TR varied between 15 – 19s, depending on TE.

Data analysis

Table S1. Scan parameters Scan parameters used for the in vivo experiments for the SE-EPI sequence.

	Resolution	$TE_{readout}$ [ms]	EPI factor	BW (phase/freq) [Hz/voxel]	Scan dur. [min]
3T	1×1×4	240 – 4740 [1]	105	8.3 / 978	3:30
	3×3×6	240 – 4740 [1]	67	23.7 / 1806	3:30
7T	1×1×2	240 – 4740 [1]	107	8.5 / 1103	3:30
	1×1×4	240 – 4740 [1]	107	8.5 / 1103	3:30
	3×3×6	240 – 4740 [1]	37	56.3 / 2626	3:30

[1] The used TEs were: 240, 285, 420, 645, 960, 1365, 1860, 2445, 3120, 3885, 4740 ms

Data analysis was identical to the data analysis of the CSF T_2 mapping sequence.

The in vivo ROI masks were made by applying an intensity threshold (25% of the maximum intensity in the scan) to the first echo time for the SE-EPI sequence (TE_{SE-EPI} = 0.24 s), leading to similar ROIs compared with the CSF T_2 mapping sequence.

For the partial volume assessment only TEs of minimally 960 ms were taken into account in the analysis. The minimum TE of 960 ms is shorter than the minimum TE of 1200 ms for the CSF T_2 mapping sequence, since shorter T_2 times were expected to be found for the SE-EPI sequence due to higher diffusion sensitivity.

Results

Phantom measurements

Figure S2 shows the results of the phantom measurements for the B_1 (**Figure S2A**) and B_0 gradient (**Figure S2B**) dependency. For B_1 of 100±2.5% and B_0 gradient 0 mT/m, the T_2 time obtained with the SE-EPI sequence was 0.96 s (95% confidence interval (CI): 0.86 – 1.05 s). The SE-EPI sequence showed no B_1 dependency, but considerably shorter T_2 times were found for increasing B_0 gradients.

In vivo measurements

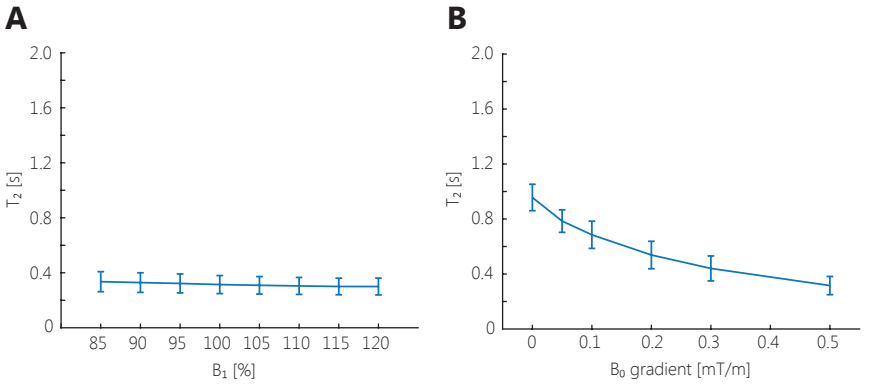

Figure S2 Results of the phantom measurements for the B_1 (A) and B_0 gradient dependency (B), showing the fitted T_2 times for different B_1s and through-plane B_0 gradient strengths, respectively. The error bars show the 95% confidence interval of the fitted T_2 times. The SE-EPI sequence shows overall shorter T_2 times than the CSF T_2 mapping sequence. The SE-EPI sequence is insensitive to B_1, but shows shorter T_2 times for increasing B_0 gradient strengths.

In one volunteer the SE-EPI scan at 3T (both resolutions) could not be acquired due to time constraints. A total of 33 SE-EPI scans were acquired, for both field strengths, and the different resolutions. Per scan 3 fits were made, one per ROI, resulting in a total of 99 fits (36 at 3T, 63 at 7T). Based on the strict requirement on minimum R^2, 21 fits were excluded (8 at 3T, 13 at 7T), which is 21% of the total number of fits (22% at 3T, 21% at 7T), see **Table S2** for a detailed overview.

The in vivo results for the SE-EPI scans with resolution 1×1×4 mm^3 are summarized

Table S2. Number of excluded fits

		Scans (fits)	Excluded fits		
			Lateral ventricles	Fourth ventricle	Periphery
3T	1×1×4	6 (18)	1	1	0
	3×3×6	6 (18)	1	5	0
Total		*12 (36)*	*2*	*6*	*0*
7T	1×1×2	7 (21)	0	2	0
	1×1×4	7 (21)	1	1	1
	3×3×6	7 (21)	3	4	1
Total		*21 (63)*	*4*	*7*	*2*

Number of acquired scans and performed T_2 fits and the number of excluded T_2 fits per ROI, for the SE-EPI sequence.

in **Figure S3**. At both 3T and 7T the T_2 times measured in the periphery were significantly shorter compared to the lateral ventricles. In all ROIs and for both field strengths, considerably shorter T_2 times were measured with the SE-EPI sequence compared to the CSF T_2 mapping sequence. The results for the other resolutions were not significantly different from the data shown here (all data, for both the SE-EPI sequence and the CSF T_2 mapping sequence, is shown in **Tables S3, S4**, and **S5**).

Partial volume assessment

The results for the additional analysis of the peripheral CSF with the longest TEs only are shown in **Figure S4**. At 3T, the peripheral CSF T_2 increased with 83 ms at 3T, although this was not significant. At 7T, no difference was observed between the corrected and uncorrected peripheral CSF T_2.

For the phantom data this analysis with only the longest TEs resulted in shorter T_2 times (**Figure S5**). This T_2 shortening was larger for larger B_0 gradients.

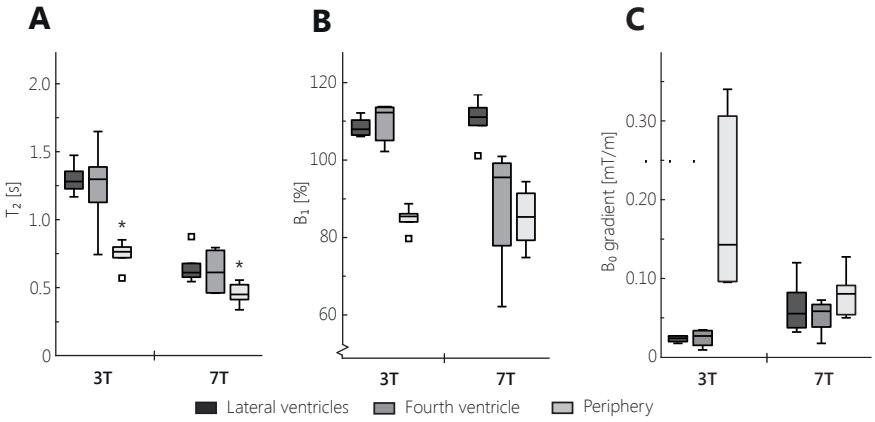

Figure S3 In vivo results: T_2 (A), B_1 (B), and B_0 gradient (C) values for the three different ROIs. Outliers are represented by a square symbol. Significant differences (indicated with the grey asterisk symbol) were found between the periphery and the lateral ventricles for the SE-EPI sequence, at both field strengths (indicated using the asterisk symbol).

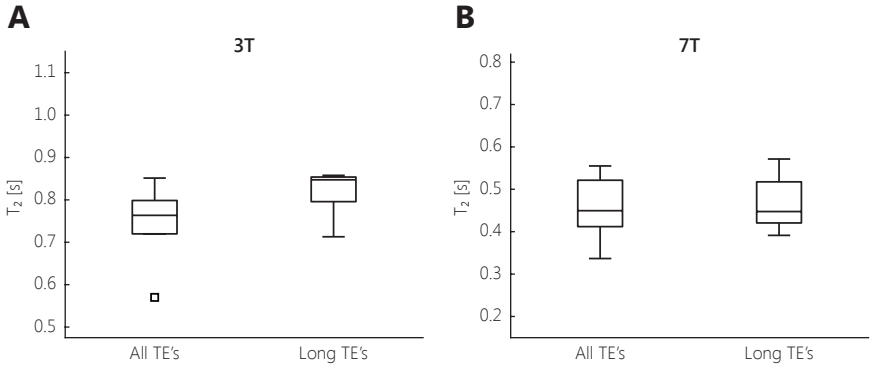

Figure S4 T_2 times of peripheral CSF, resulting from the use of only the longest TEs, compared with the original analysis, at 3T (A) and at 7T (B). Outliers are represented by a square symbol. For the SE-EPI sequence the T_2 increased only at 3T, but this was not significant.

Table S3. In vivo results, lateral ventricles

			T_2 [s] median (average±SD)	B_0 gradient [mT/m] median (average±SD)	B_1 [%] median (average±SD)	ROI size [mm²] median (average±SD)	n
3T	T_2-prep	1×1×4	2.03 (1.99±0.16)	0.025 (0.029±0.016)	109 (109±2)	122 (128±85)	7
		3×3×6	1.96 (2.02±0.10)	0.032 (0.034±0.017)	111 (111±1)	54 (68±54)	5
	SE-EPI	1×1×4	1.28 (1.30±0.11)	0.024 (0.023±0.004)	108 (108±2)	127 (148±101)	5
		3×3×6	1.13 (1.16±0.24)	0.029 (0.036±0.023)	109 (109±2)	54 (65±57)	5
7T	T_2-prep	1×1×2	1.07 (1.12±0.17)	0.059 (0.063±0.028)	110 (108±8)	98 (103±95)	7
		1×1×4	1.05 (1.04±0.07)	0.068 (0.066±0.027)	111 (110±5)	87 (83±54)	6
		3×3×6	1.06 (1.04±0.07)	0.062 (0.069±0.034)	113 (110±9)	59 (63±55)	6
	SE-EPI	1×1×2	0.64 (0.66±0.13)	0.057 (0.066±0.038)	110 (110±7)	123 (115±96)	7
		1×1×4	0.61 (0.65±0.12)	0.055 (0.064±0.034)	111 (109±8)	90 (111±110)	6
		3×3×6	0.55 (0.59±0.15)	0.068 (0.076±0.049)	110 (109±11)	54 (65±50)	4

T_2, B_1, and B_0 values for the lateral ventricles, and the ROI sizes and number of included fits, n, for both the CSF T_2 mapping sequence (T_2-prep) and the SE-EPI sequence.

Table S4. In vivo results, fourth ventricle

			T_2 [s] median (average±SD)	B_0 gradient [mT/m] median (average±SD)	B_1 [%] median (average±SD)	ROI size [mm²] median (average±SD)	n
3T	T_2-prep	1×1×4	2.08 (2.04±0.16)	0.028 (0.024±0.009)	112 (110±5)	75 (86±29)	6
		3×3×6	1.99 (1.97±0.19)	0.029 (0.023±0.012)	112 (110±5)	14 (20±13)	6
	SE-EPI	1×1×4	1.30 (1.25±0.32)	0.027 (0.024±0.011)	112 (110±5)	79 (84±26)	5
		3×3×6	1.47 (1.47±0)	0.004 (0.004±0)	100 (100±0)	27 (27±0)	1
7T	T_2-prep	1×1×2	1.12 (1.14±0.21)	0.049 (0.049±0.021)	91 (86±13)	58 (58±24)	6
		1×1×4	0.96 (0.96±0.06)	0.056 (0.057±0.016)	96 (89±18)	60 (64±30)	4
		3×3×6	1.04 (1.14±0.28)	0.051 (0.047±0.014)	92 (93±2)	18 (21±14)	3
	SE-EPI	1×1×2	0.75 (0.74±0.09)	0.042 (0.044±0.016)	94 (92±9)	52 (56±31)	5
		1×1×4	0.61 (0.62±0.15)	0.058 (0.052±0.020)	94 (88±14)	43 (52±32)	6
		3×3×6	0.73 (0.73±0.08)	0.058 (0.047±0.026)	92 (91±9)	18 (18±0)	3

T_2, B_1, and B_0 values for the fourth ventricle, and the ROI sizes and number of included fits, n, for both the CSF T_2 mapping sequence (T_2-prep) and the SE-EPI sequence.

Table S5. In vivo results, periphery

			T_2 [s] median (average±SD)	B_0 gradient [mT/m] median (average±SD)	B_1 [%] median (average±SD)	ROI size [mm²] median (average±SD)	n
3T	T_2-prep	1×1×4	1.67 (1.61±0.13) [a,b]	0.129 (0.194±0.118)	85 (86±4)	632 (664±244)	7
		3×3×6	1.59 (1.60±0.12) [a,b]	0.094 (0.150±0.143)	87 (87±4)	1161 (1103±329)	7
	SE-EPI	1×1×4	0.76 (0.74±0.10) [a]	0.143 (0.187±0.111)	85 (85±3)	818 (774±245)	6
		3×3×6	0.74 (0.72±0.10) [a]	0.114 (0.173±0.123)	86 (86±3)	1283 (1248±352)	6
7T	T_2-prep	1×1×2	0.93 (0.94±0.10) [b]	0.062 (0.067±0.014)	85 (84±7)	421 (456±119)	7
		1×1×4	0.89 (0.92±0.10)	0.061 (0.066±0.014)	85 (85±7)	484 (493±109)	7
		3×3×6	0.91 (0.93±0.10)	0.074 (0.076±0.015)	85 (85±6)	936 (928±224)	7
	SE-EPI	1×1×2	0.46 (0.46±0.08) [a,b]	0.077 (0.080±0.031)	86 (86±8)	501 (493±119)	7
		1×1×4	0.45 (0.45±0.08) [a]	0.080 (0.081±0.028)	88 (88±7)	462 (471±122)	6
		3×3×6	0.43 (0.45±0.08)	0.077 (0.075±0.015)	86 (86±5)	684 (720±207)	6

T_2, B_1, and B_0 values for the periphery, and the ROI sizes and number of included fits, n, for both the CSF T_2 mapping sequence (T_2-prep) and the SE-EPI sequence. a) significant compared to the lateral ventricles, b) significant compared to the fourth ventricle.

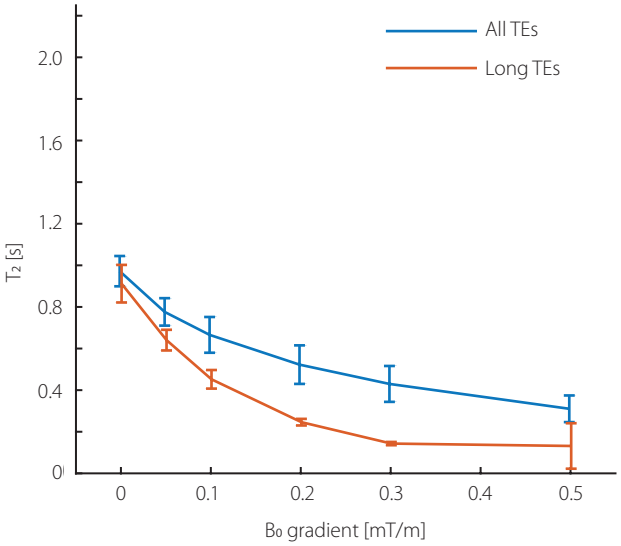

Figure S5 T_2 times of the phantom, resulting from the use of only the longest TEs (orange), compared with the original analysis (blue). For the SE-EPI sequence the T_2 times were shorter for the analysis using only the longest TEs. The difference increased for an increasing B_0 gradient.

Discussion

For the SE-EPI sequence the peripheral $T_{2,CSF}$ was significantly shorter than the ventricular $T_{2,SCF}$ at both 3T and 7T.

In the phantom measurements no B_1 dependency was found for the SE-EPI sequence, similar to the CSF T_2 mapping sequence, as shown in **Figure S2**. The measurements with an increasing through-plane B_0 gradient resulted in shorter T_2 times for larger B_0 gradients. Only a relatively small gradient was needed to find shorter T_2 times for the SE-EPI sequence, while a much larger gradient was needed to find shorter T_2 times for the CSF T_2 mapping sequence (**Figure 3B**). This can be explained by the longer echo spacings compared with the CSF T_2 mapping sequence, which increases the sensitivity for diffusion (*3*). Higher diffusion sensitivity for the SE-EPI sequence is also apparent from the analysis including only the longest TEs: shorter T_2 times were obtained for the SE-EPI sequence when only the longest echo spacings (longest TEs) were included. In contrast, the CSF T_2 mapping sequence showed similar results when only the longest TEs were included, for all B_0 gradient strengths. The difference in diffusion sensitivity of both sequences is further illustrated by the relative difference in b-value for both sequences which can be readily computed from the echo spacing and the number of refocusing pulses (*4*): the b-value of the SE-EPI sequence is 20 to 986 times larger compared to the CSF T_2 mapping sequence, for TEs 600 – 4800 ms, respectively. The difference in diffusion sensitivity is also visible in the different behavior of the long TE analysis on the phantom measurements. For the SE-EPI a shorter T_2 is measured when only long TEs (with stronger diffusion weighting) are used, while this is not the case for the CSF T_2 mapping sequence (compare **Figure 6** with **Figure S5**).

Partial volume correction showed a relatively small T_2 increase (approximately 80 ms) at 3T, but this was not significant. At 7T the T_2 times did not change. This suggests that for the SE-EPI sequence the observed T_2 difference between ventricular and peripheral CSF is (predominantly) not caused by partial volume effects. However, the T_2 times measured with this sequence are much shorter compared with the CSF T_2 mapping sequence, probably due to its high sensitivity for diffusion and flow. If the partial volume effect in the CSF T_2 mapping sequence is indeed caused by arterial blood or relatively free water in the outer rim of the cortex, the diffusion sensitivity of the SE-EPI sequence may decrease the sensitivity for partial volume effects from this compartment. Alternatively, it is possible that microscopic gradients around the (venous) vasculature at the brain surface induce a shorter T_2 due to the diffusion sensitivity of the SE-EPI sequence, and that this effect cannot be corrected by choosing longer TEs.

The T_2 difference between peripheral and ventricular CSF was 517 ms at 3T, and 160 ms at 7T, a relative difference of 40% and 26% compared with the T_2 in the lateral ventricles. After partial volume correction, the T_2 difference decreased to 433 ms for 3T, a difference of 33% relative to the ventricular CSF T_2, and was unchanged at 7T. Thus, a much larger T_2 difference between peripheral and ventricular CSF was found compared with the CSF T_2 mapping sequence. The T_2 difference at 3T can be partly explained by the larger B_0 gradients in the periphery, but at 7T the B_0 gradients were similar for all ROIs. Furthermore, overall shorter T_2 times were found compared with the CSF T_2 mapping sequence. The SE-EPI sequence is more sensitive to flow and diffusion than the CSF T_2 mapping sequence, which uses multiple refocusing pulses with a fixed echo spacing that is shorter than the shortest TE used in the SE-EPI sequence. The higher flow and diffusion sensitivity of SE-EPI might (partly) cause the larger T_2 difference between peripheral and ventricular CSF. The CSF flow in the periphery is lower compared with the ventricles and cannot explain a shorter peripheral T_2, but diffusion effects around the blood vessels on the cortex may be relatively strong. Since the ventricular walls are not covered with blood vessels, diffusion effects may be relatively small in the ventricles in areas away from the choroid plexus at the base of the ventricles. Based on Kiselev, *et al.* (*5*), the level of signal dephasing due to diffusion around blood vessels is larger at 7T compared with 3T. This would imply a larger difference between peripheral and ventricular T_2 at 7T, contrary to our observations. It is conceivable, however, that the relative contribution of macroscopic field inhomogeneity to diffusion related T_2 shortening is larger at 7T than at 3T for the SE-EPI T_2 mapping, which could partially mask regional differences in microscopic field inhomogeneity. This is, however, not supported by the measured B_0 gradients from the B_0 maps that were acquired in vivo. As we used image based third order shimming at 7T, the shimming at the periphery seemed to be better at 7T than 3T, where linear shimming was used.

The SE-EPI sequence resulted in different T_2 times compared to the CSF T_2 mapping sequence, partly due to a different sensitivity to e.g. flow and diffusion effects. The effects of these confounding factors on the observed T_2 times were not studied thoroughly in this work.

Moreover, for the phantom measurements with increasing B_0 background gradient, the acquired signal decay profile showed some deviation from a single exponential decay profile due to relatively stronger diffusion effects for longer TEs. For the in vivo data however, the acquired signal decay only showed minor deviation from a single exponential decay profile. Some in vivo scans were excluded based on the minimum R^2 of 0.99, this was mainly due to motion and/or the presence of flow voids in the data.

Finally, for the SE-EPI sequence at 7T, the measured peripheral CSF T_2 was 450 ms. For the partial volume correction a minimum TE of 960 ms was used, almost double the CSF T_2. This may decrease the sensitivity for small T_2 changes.

References

1. B. Sweetman, A. A. Linninger, Cerebrospinal fluid flow dynamics in the central nervous system. *Ann. Biomed. Eng*. 39, 484–496 (2011).

2. K. P. Pruessmann *et al.*, SENSE: sensitivity encoding for fast MRI. *Magn. Reson. Med.* 42, 952–962 (1999).

3. B. M. Dale, M. A. Brown, R. C. Semelka, MRI Basic principles and applications (John Wiley & Sons Inc, Fifth edit., 2015).

4. H. Carr, E. Purcell, Effects of diffusion on free precession in Nuclear Magnetic Resonance experiments. *Phys*. Rev. 94, 630–638 (1954).

5. V. Kiselev, S. Posse, in *Proc. Intl. Soc. Mag. Reson. Med.* (1998), p. 1397.

Chapter 6

Summary and general discussion

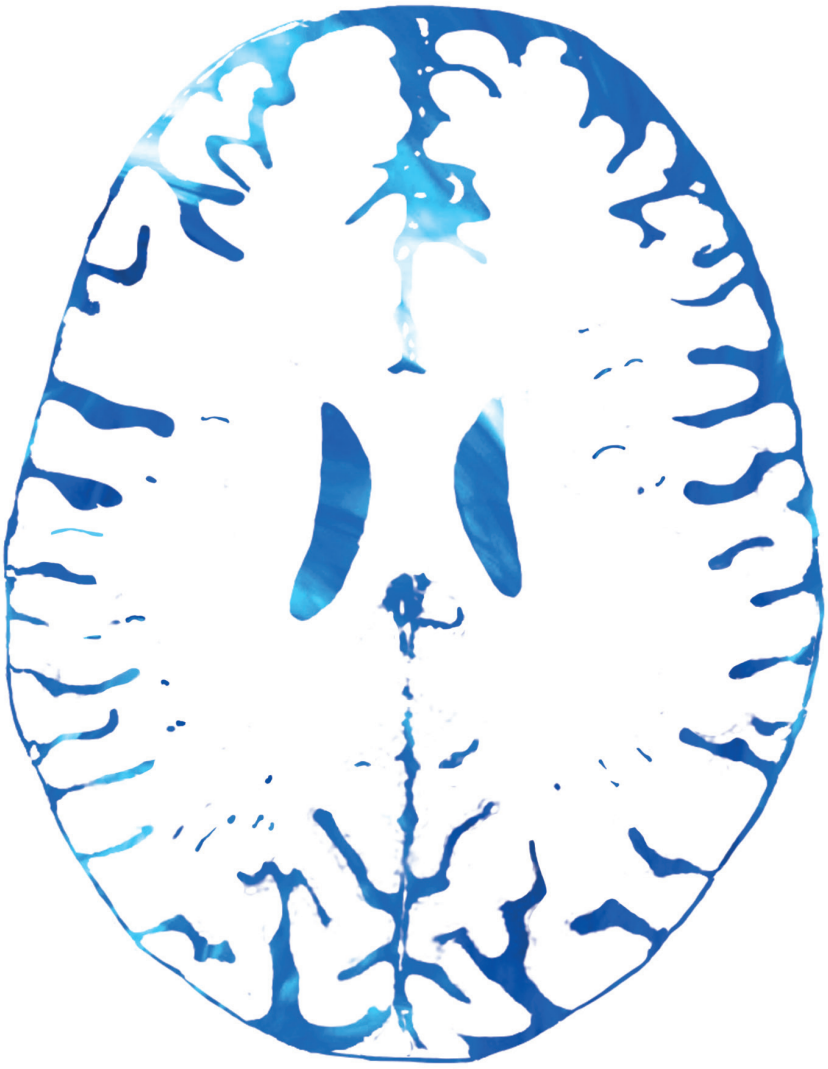

Summary

The current gold standard for imaging diseases such as cerebral Small Vessel Disease (SVD) is the assessment of structural tissue damage using anatomical MRI. However, the tissue damage is merely an (irreversible) consequence of the disease, while the underlying pathology of the blood vessels is not well known and very difficult to visualize. A potential solution could be found in quantitative MRI (qMRI), as this can be used to acquire information that goes beyond structural imaging. As the brain fluids are in connection to both the blood vessels and the brain tissue, qMRI of brain fluids may offer a window on the brain in health and disease.

The overall goal of this thesis was to explore quantitative MRI measurements of brain fluid properties as a potential measure to study diseases such as SVD. In this work we explored the mapping of perivascular spaces (PVS) count, cerebrospinal fluid (CSF) production rate, and CSF composition differences.

We presented an automatic method to annotate PVS and demonstrated that this method performs well in high-resolution T_2-weighted MRI images acquired at 7T (**Chapter 2**). Additionally, the method can determine the PVS length and tortuosity, thereby generating additional PVS metrics that are difficult to obtain manually. However, 3T MRI is much more widely available than 7T MRI, and therefore a method to accurately determine the PVS count using low-resolution scans acquired at 3T would be very valuable. As the PVS count in the low-resolution scans depends strongly on the used scan sequence and resolution, PVS annotation is likely not a suitable method in these scans. Therefore, texture features of the 3T images were explored as measure for the PVS count in the 7T images. However, we could not successfully estimate the PVS count as observed in the high-resolution images with the texture features in the low-resolution images acquired at 3T (**Chapter 3**).

Subsequently, we showed that net CSF flow PC-MRI measurements in the cerebral aqueduct are confounded by respiration (**Chapter 4**). As a result, the reproducibility of the net CSF flow measurements was poor. Including also respiratory gating in the net CSF flow PC-MRI measurements resulted in strongly improved reproducibility. Furthermore, it was found that net flow difference between inspiration and expiration correlates with stroke volume.

Finally, T_2 differences between CSF in the ventricles and CSF in the subarachnoid space have been previously reported, and were hypothesized to be caused by CSF composition differences. In **Chapter 5** this CSF T_2 difference was reproduced, but it was also found that confounding factors of i.e. partial volume and B_0-gradients also contribute to the observed CSF T_2 difference between the ventricles and the

subarachnoid space. Due to these confounding factors it appeared to be very difficult to separate the effect size of intracranial CSF composition differences on the measured CSF T_2 times.

In this Discussion chapter the value and challenges of quantitative MRI measurements of CSF will be discussed and potential solutions will be explored. Also, the results presented in this work will be compared with other non-invasive and invasive quantitative CSF measurements.

Exploring potential solutions for the challenges in qMRI of brain fluids

Perivascular spaces

Fully automatic PVS annotation offers the possibility to incorporate the PVS count as a parameter in large clinical research studies. To determine the PVS load in the brain, also the total intracranial tissue volume and/or the level of atrophy could be taken into account, rather than only the PVS count.

A fundamental problem remains for PVS annotation: the PVS can be very small, i.e. in the micrometer range (*1*), and are thus close to the noise-level. Therefore good validation is necessary before automatic PVS annotation can be applied in clinical research studies. This may be achieved by using phantom studies, with for example a 3D-printed phantom (*2*). In such a phantom the T_1- and T_2- relaxation properties should be similar to the in vivo values, to achieve a similar MRI contrast compared with the in vivo scans. Additionally, in silico studies using digital phantoms can be performed (*3*). MR images can be calculated using the digital phantoms as input, and these MR images are then used as input for the automatic post-processing method for PVS annotation. In both the real and digital phantoms all PVS parameters, such as count, diameter, length, and tortuosity, are known. This offers good validation for PVS annotation by human observers, and for automatic PVS annotation.

The structural details that can be observed with anatomical MRI will remain limited, as a decrease in voxel size, and thus an increase in resolution, is accompanied by an increase in scan time and a decrease in signal to noise ratio (SNR). Even a small decrease in voxel size (for example, from 0.8 to 0.7 mm isotropic) has a large effect on the scan time and SNR (*4*). As a result, detection of all small PVS in anatomical MRI scans is not feasible. Therefore, also alternative techniques, such as diffusion weighted imaging (DWI), $T_{1\rho}$ imaging, or imaging with extremely long echo times (*5–7*), could be explored to determine the total PVS volume.

Currently, the PVS count can be annotated accurately in high-resolution scans acquired at 7T MRI. In contrast, only the large PVS can be annotated in lower-resolution scans acquired at 3T MRI, which appeared not to be representative for the PVS count that can be acquired in high-resolution scans at 7T MRI. The white matter texture measures in 3T MRI images also appeared to be unsuitable as a measure for the PVS count observed in high-resolution scans. Thus, 7T MRI enables the acquisition of PVS information that cannot (yet) be acquired at lower field strengths.

However, given the wide availability of 3T MRI, the PVS load acquired in low-resolution 3T scans could be more easily incorporated in clinical studies as compared to the high-resolution 7T scans. Therefore, it may still be valuable to investigate alternative analyses. For example, non-linear feature analyses or deep learning methods may yield a measure for the PVS load (*8*, *9*).

CSF flow

The key advantage of net CSF flow measurements with PC-MRI as a measure for the CSF production rate is that it is a non-invasive and fast method. The current gold standard for measuring the CSF production rate is an invasive method (*10*, *11*), based on the Masserman method (*12*). Via a lumbar puncture or a ventricular catheter first the baseline intracranial pressure is determined, then a volume of CSF is collected, and finally the intracranial pressure increase is determined. The CSF production rate can be calculated using the collected CSF volume, the intracranial pressure decrease immediately after the CSF collection, and the intracranial pressure increase rate (*10*). Alternatively, the CSF production rate can be determined using the collected CSF volume and the time elapsed until the intracranial pressure returned to baseline (*11*). The main disadvantage of this method is that this is an invasive procedure, and complications can occur. Also, the accuracy of the method is under discussion, as CSF absorption during the measurement cannot be quantified (*13*), and in case of the lumbar puncture damping effects due spinal stenosis can affect the measurements (*11*, *14*).

PC-MRI of the aqueductal net CSF flow offers a non-invasive method to acquire a measure for the CSF production rate in the lateral ventricles and the third ventricle. The exact CSF production rate cannot be determined with these measurements, as a small part of the choroid plexus, which produces the CSF, is located in the fourth ventricle, which is located caudal to the cerebral aqueduct. Also, CSF flow through the ependyma towards the periventricular white matter, which has been

observed in hydrocephalus (*15*), might also occur in healthy subjects. PC-MRI has often been used in (clinical) research studies (*16–24*). These studies occasionally resulted in contradictory results: for example, in communicating hydrocephalus patients cranially directed net CSF flows have been found (*19*, *21*). We showed that respiration is a strong confounding factor in the net CSF flow measurements with PC-MRI, that can result in a cranially directed net CSF flow. The large influence of respiration is probably related to the small net flow relative to the observed stroke volumes. Given the strong confounding effect of respiration, the reliability of the net CSF flow measurements in previous clinical studies is debatable. Thorough investigation of the method and its possible confounding factors, such as respiration, should have been performed prior to application of the method in clinical studies.

Furthermore, we showed that the CSF dynamics over the cardiac and respiratory cycles are correlated. This may be related to the system's compliance to intracranial blood volume variations. CSF flow measurements can thus offer the possibility to characterize CSF dynamics over the cardiac and respiratory cycles. For such CSF measurements it is important to also take the CSF flow at the cervical level into account, as the CSF flow through the aqueduct is much smaller than the CSF flow at the cervical level (*25*). However, PC-MRI is not a suitable technique to characterize the CSF dynamics and production rate, as both the respiration and cardiac cycles contribute to the measured CSF flow. Alternatively, the DENSE sequence can be used to measure CSF displacements over the cardiac and respiratory cycle separately (*26*, *27*). This method also offers the possibility of whole-brain measurements, so that local CSF displacements can be determined. It is also possible to determine the net CSF flow over the cardiac cycle, by selecting only measurements for the same respiratory phase. This may result in a more robust estimate for the net CSF flow, without the large confounding factor of respiration. Similarly, also the CSF flow over the respiratory cycle may be determined. Finally, measurements of the brain tissue displacements over the cardiac and respiratory cycles, could give a more detailed assessment of the CSF dynamics and of the interplay between CSF and tissue.

CSF T_2 mapping

Quantitative T_2 mapping could in principle provide valuable information on the CSF composition. But although T_2 mapping of CSF is feasible, the interpretation of the results appeared to be very challenging. For the T_2 mapping of CSF we used the hypothesis that partial volume and CSF composition differences contribute

to the T_2 difference between the subarachnoid space and the ventricles. CSF composition differences of e.g. proteins and glucose could in theory account for a total T_2 difference of approximately 30 ms at 3T, assuming a 10% difference in the protein and glucose levels between the ventricular and subarachnoid CSF (*28–32*). This T_2 difference could be further increased by varying potassium levels (*33*) and possibly also by varying oxygen levels, as the CSF is produced from arterial blood by the choroid plexus (*34–36*). However, our hypothesis could not sufficiently explain the measured T_2 times, even after correcting for the confounding factors of partial volume and B_0. Therefore, this method is not yet ready for use as a marker for intracranial CSF composition differences.

As a solution, the CSF T_2 mapping method could be regulated further, for example by improving B_0 shimming to minimize the confounding effect of B_0 inhomogeneities. The effect of improved B_0 shimming on the CSF T_2 mapping method may be limited, as microscopic B_0 gradients and diffusion effects around the blood vessels at the brain surface will remain. The effect size of these gradients and diffusion effects cannot be easily estimated. However, it is possible that such microscopic B_0 gradients are similar between subjects. Furthermore, the presence of partial volume in the peripheral CSF may be corrected by taking the (cortical) atrophy into account.

It is likely that T_2 measurements of CSF are most suitable to assess differences between groups, rather than individual differences, as this would reduce the influence of remaining confounding effects of partial volume and B_0 in individual subjects. For example, shorter peripheral CSF T_2 times have been observed in patients with cognitive decline by Van der Kleij *et al.* (*37*). Also, the T_2 of the peripheral CSF was correlated with the cerebral blood flow, indicating that the peripheral CSF T_2 may be predictive for the local oxygenation in these patients. In this study longer T_2 times were observed in subjects with decreased cerebral blood flow. This may well be related to the microscopic B_0 gradients and diffusion effects around the blood vessels at the brain surface: these gradients are likely smaller if the (local) blood flow is reduced. This would then result in reduced signal dephasing and thus in longer T_2 times.

To assess individual intracranial CSF composition differences also other techniques, such as MR Spectroscopy (*38*, *39*), could be pursued, or PET could be used to assess e.g. CSF clearance (*40*). These techniques, i.e. MR Spectroscopy or PET, could also be used in combination with the CSF T_2 measurements to gain better understanding of the mechanisms underlying the measured T_2 times. However, in MR Spectroscopy

large voxel sizes are required to achieve a sufficient SNR. As low resolutions increase the problem of partial volume in the subarachnoid space, this issue would need to be addressed. A potential solution may be to incorporate a T_2-preparation phase in the scan sequence, to remove the tissue signal.

Overall, the work presented in this thesis emphasizes the importance of understanding the acquired quantitative MRI measurements. To do so, it is important to build a robust model that can fully explain the measurements, as was also argued by Novikov *et al.* (*41*). In such a model all confounding factors should be incorporated. Alternatively, the experiments should be designed such that the underlying model can be simplified and thus the number of confounding factors is reduced, or the effect of the confounding factors on the measured parameters should be equal between groups.

Value of qMRI of brain fluids

Quantitative measurements of brain fluids can potentially be very valuable in research of brain disease, as brain fluids are in contact with both the intracranial blood and the brain tissue. The most obvious application of such measurements would be SVD, where qMRI of brain fluids could be used to study the earlier stages of SVD before any structural tissue damage has occurred. However, brain fluids can also be a valuable parameter in, for example, oncology (*42*), multiple sclerosis (*43*, *44*), or epilepsy (*45*, *46*).

The three brain fluid measurements, of i.e. the PVS load, CSF dynamics, and CSF composition, supply different types of information, and may therefore be best suited to investigate different pathologies. For example, in oncology the CSF composition is likely the most interesting parameter, while the CSF dynamics would be of interest in e.g. hydrocephalus. However, as the brain fluids are interconnected it can also be argued that the brain fluid measurements are linked. For example, in case of altered CSF dynamics also the CSF composition may be altered due to an in- or decrease in CSF volume or flow. Thus, in hydrocephalus also the CSF composition may be changed, additionally to the CSF dynamics, due to the altered CSF production and/or absorption rates in this disease. Furthermore, an increased PVS count and size has been linked to impaired brain clearance (*47*), which may also affect the CSF composition. Therefore a combination of brain fluid measurements should be used to gain better insight in the early stages of complicated diseases such as SVD or Alzheimer's Disease.

Conclusion

SVD progress is difficult to assess in vivo, especially in the early stages of the disease before tissue damage has occurred. In this thesis we investigated the value of quantitative MRI of brain fluids for research of e.g. SVD. Determining the PVS load using an automatic annotation method is a very promising technique. Extending this method to annotate PVS in the whole brain can further increase the value of this method. PVS texture analysis cannot yet be used to determine the PVS load in 3T scans. However, more sophisticated analyses such as non-linear analyses, or deep learning, can still be pursued. PC-MRI measurements of CSF proved to be unsuitable as a measure for the CSF production rate, due to the confounding factor of respiration. However, our measurements showed that the CSF flow over the cardiac and respiratory cycles may provide a window to map the CSF dynamics in greater detail. Finally, mapping of intracranial CSF composition (differences) remains something for the future. On the other hand, it is possible that T_2 mapping of CSF may give insight in CSF composition differences between groups of subjects. Overall, we can conclude that brain fluids are a challenging parameter to use for SVD research, and further developments are needed before this can be used in clinical research.

References

1. J. M. Wardlaw *et al.*, Neuroimaging standards for research into small vessel disease and its contribution to ageing and neurodegeneration. *Lancet Neurol.* 12, 822–838 (2013).
2. D. Mitsouras *et al.*, 3D Printing of MRI-visible phantoms and MR Image-guided therapy simulation. *Magn. Reson. Med.* 77, 613–622 (2017).
3. T. B. Martonen, J. D. Schroeter, J. S. Fleming, 3D in silico modeling of the human respiratory system for inhaled drug delivery and imaging analysis. *J. Pharm. Sci.* 96, 603–617 (2007).
4. A. G. van der Kolk, J. Hendrikse, J. J. M. Zwanenburg, F. Visser, P. R. Luijten, Clinical applications of 7 T MRI in the brain. *Eur. J. Radiol.* 82, 708–718 (2013).
5. R. Bammer, Basic principles of diffusion-weighted imaging. *Eur. J. Radiol.* 45, 169–184 (2003).
6. A. J. Wheaton, A. Borthakur, S. R. Charagundla, R. Reddy, Pulse sequence for multislice $T_1\rho$-weighted MRI. *Magn. Reson. Med.* 51, 362–369 (2004).
7. Q. Qin, A simple approach for three-dimensional mapping of baseline cerebrospinal fluid volume fraction. *Magn Reson Med*. 65, 385–391 (2011).
8. S. L. Kukreja, J. Löfberg, M. J. Brenner, A least absolute shrinkage and selection operator (Lasso) for nonlinear system identification. *IFAC Proc. Vol.* 39, 814–819 (2006).
9. Y. LeCun, Y. Bengio, G. Hinton, Deep learning. *Nature*. 521, 436 (2015).
10. M. Edsbagge *et al.*, Alzheimer's Disease-associated cerebrospinal fluid (CSF) biomarkers do not correlate with CSF volumes or CSF production rate. *J. Alzheimer's Dis.* 58, 821–828 (2017).
11. G. D. Silverberg *et al.*, The cerebrospinal fluid production rate is reduced in dementia of the Alzheimer's type. *Neurology*. 57, 1763–1766 (2001).
12. J. H. Masserman, Cerebrospinal hydrodynamics IV. Clinical experimental studies. *Arch Neurol Psychiatry*. 32, 523–553 (1934).
13. T. Brinker, E. Stopa, J. Morrison, P. Kinge, A new look at cerebrospinal fluid circulation. *Fluids Barriers CNS*, 1–16 (2014).
14. L. Kalichman *et al.*, Spinal stenosis prevalence and association with symptoms: The Framingham Study. *Spine J.* 9, 545–550 (2009).
15. G. Ringstad, S. A. S. Vatnehol, P. K. Eide, Glymphatic MRI in idiopathic normal pressure hydrocephalus. *Brain*. 140, 2691–2705 (2017).
16. C. Nilsson *et al.*, Circadian variation in human cerebrospinal fluid production measured by magnetic resonance imaging. *Am. J. Physiol.* 262, R20–R24 (1992).
17. H. W. S. Schroeder, C. Schweim, K. H. Schweim, M. R. Gaab, Analysis of aqueductal cerebrospinal fluid flow after endoscopic aqueductoplasty by using cine phase-contrast magnetic resonance imaging. *J. Neurosurg.* 93, 237–244 (2000).
18. P. H. Luetmer *et al.*, Measurement of cerebrospinal fluid flow at the cerebral aqueduct by use of phase-contrast magnetic resonance imaging: Technique validation and utility in diagnosing idiopathic normal pressure hydrocephalus. *Neurosurgery*. 50, 534–543 (2002).
19. O. Balédent *et al.*, Relationship between cerebrospinal fluid and blood dynamics in healthy volunteers and patients with communicating hydrocephalus. *Invest. Radiol.* 39, 45–55 (2004).
20. S. K. Piechnik, P. E. Summers, P. Jezzard, J. V. Byrne, Magnetic resonance measurement of blood and CSF flow rates with phase contrast - Normal values, repeatability and CO_2 reactivity. *Acta Neurochir. Suppl.*, 263–270 (2008).

21. G. A. Bateman, K. M. Brown, The measurement of CSF flow through the aqueduct in normal and hydrocephalic children: From where does it come, to where does it go? *Child's Nerv. Syst.* 28, 55–63 (2012).

22. C. Magnano *et al.*, Cine cerebrospinal fluid imaging in multiple sclerosis. *J. Magn. Reson. Imaging*. 36, 825–834 (2012).

23. C. B. Beggs *et al.*, Internal jugular vein cross-sectional area and cerebrospinal fluid pulsatility in the aqueduct of Sylvius: A comparative study between healthy subjects and Multiple Sclerosis patients. *PLoS One*. 11, 1–13 (2016).

24. G. Ringstad, K. E. Emblem, P. K. Eide, Phase-contrast magnetic resonance imaging reveals net retrograde aqueductal flow in idiopathic normal pressure hydrocephalus. *J. Neurosurg.* 124, 1850–1857 (2016).

25. O. Balédent, M.-C. C. Henry-Feugeas, I. Idy-Peretti, Cerebrospinal fluid dynamics and relation with blood flow. *Invest. Radiol.* 36, 368–377 (2001).

26. A. Adams, P. R. Luijten, J. J. M. Zwanenburg, in *ISMRM proceedings* (2017), p. 704.

27. J. J. Sloots, A. L. Adams, P. R. Luijten, G. J. Biessels, J. J. M. Zwanenburg, Unraveling cardiac and respiratory contributions to brain tissue motion using single shot 2D DENSE at 7T MRI, *in ISMRM proceedings (2018), p. 368.*

28. A. Yilmaz, F. Ş. Ulak, M. S. Batun, Proton T_1 and T_2 relaxivities of serum proteins. *Magn. Reson. Imaging*. 22, 683–688 (2004).

29. K. Roos, *Principles of Neurologic Infectious Disease* (McGraw-Hill Professional, 2005).

30. B. L. C. Wright, J. T. F. Lai, A. J. Sinclair, Cerebrospinal fluid and lumbar puncture: A practical review. *J. Neurol.* 259, 1530–1545 (2012).

31. N. N. Yadav *et al.*, Natural D-glucose as a biodegradable MRI relaxation agent. *Magn. Reson. Med.* 72, 823–828 (2014).

32. A. Daoust *et al.*, Transverse relaxation of cerebrospinal fluid depends on glucose concentration. *Magn. Reson. Imaging*. 44, 72–81 (2017).

33. L. Bito, H. Davson, Local variations in cerebrospinal fluid composition and its relationship to the composition of the extracellular fluid of the cortex. *Exp. Neurol.* 280, 264–280 (1966).

34. N. J. Abbott, Evidence for bulk flow of brain interstitial fluid: Significance for physiology and pathology. *Neurochem. Int.* 45, 545–552 (2004).

35. H. Wolburg, W. Paulus, Choroid plexus: Biology and pathology. *Acta Neuropathol.* 119, 75–88 (2010).

36. R. Spector, S. Robert Snodgrass, C. E. Johanson, A balanced view of the cerebrospinal fluid composition and functions: Focus on adult humans. *Exp. Neurol.* 273, 57–68 (2015).

37. L. A. van der Kleij *et al.*, Lower oxygenation in the peripheral subarachnoid space reflects decreased cerebral blood flow in dementia-related brain structures. *ISMRM Proc.*, 732 (2018).

38. J. K. Nicholson, I. D. Wilson, High resolution proton Magnetic Resonance Spectroscopy of biological fluids. *Prog. NMR Spectrosc.* 21, 449–501 (1989).

39. I. L. Simone *et al.*, High resolution proton MR Spectroscopy of cerebrospinal fluid in MS patients. Comparison with biochemical changes in demyelinating plaques. *J. Neurol. Sci.* 144, 182–190 (1996).

40. M. J. de Leon *et al.*, CSF clearance in Alzheimer Disease measured with dynamic PET. *J. Nucl. Med.*, 1471–1476 (2017).

41. D. S. Novikov, V. G. Kiselev, S. N. Jespersen, On modeling. *Magn. Reson. Med.* 79, 3172–3193 (2018).

42. C. L. Weston, M. J. Glantz, J. R. Connor, Detection of cancer cells in the cerebrospinal fluid: Current methods and future directions. *Fluids Barriers CNS*. 8, 14 (2011).

43. C. H. Polman *et al.*, Diagnostic criteria for multiple sclerosis: 2010 Revisions to the McDonald criteria. *Ann. Neurol.* 69, 292–302 (2011).

44. S. Öner *et al.*, Cerebrospinal fluid dynamics in patients with Multiple Sclerosis: The role of phase-contrast MRI in the differential diagnosis of active and chronic disease. *Korean J Radiol*. 19, 72–78 (2018).

45. A. Chatzikonstantinou, A. D. Ebert, M. G. Hennerici, Cerebrospinal fluid findings after epileptic seizures. *Epileptic Disord.* 17, 453–459 (2015).

46. H. Tumani *et al.*, Effect of epileptic seizures on the cerebrospinal fluid – A systematic retrospective analysis. *Epilepsy Res.* 114, 23–31 (2015).

47. R. Brown *et al.*, Understanding the role of the perivascular space in cerebral small vessel disease. *Cardiovasc. Res.* (2018), doi:https://doi.org/10.1093/cvr/cvy113.

Addendum

Nederlandse samenvatting
Dutch summary

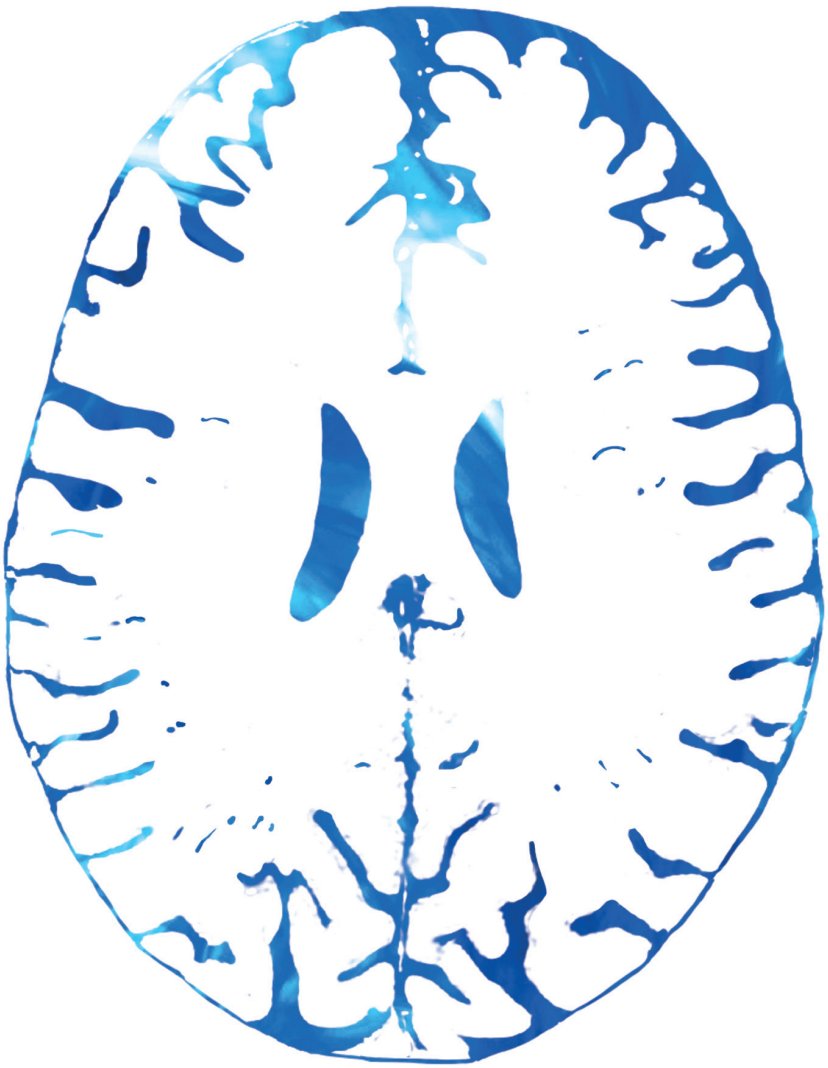

De huidige gouden standaard om ziektes als Cerebral Small Vessel Disease (SVD) in beeld te brengen, is het beoordelen van de weefselschade met anatomische MRI beelden. Deze weefselschade is echter niet meer dan een (onomkeerbaar) gevolg van SVD. Bovendien is de onderliggende pathologie aan de kleine bloedvaten in het brein heel divers, grotendeels onbekend, en zeer moeilijk in beeld te brengen. Een mogelijke oplossing kan gevonden worden in kwantitatieve MRI metingen, aangezien deze gebruikt kunnen worden om functionele informatie te verkrijgen die meer inzicht kan verschaffen in ziekteprocessen dan conventionele, anatomische MRI beelden. Aangezien het hersenvocht in verbinding staat tot zowel de bloedvaten als het breinweefsel kunnen kwantitatieve MRI metingen van hersenvocht een mogelijke opening bieden om ook de vroegste stadia van ziektes als SVD te bestuderen.

Het algemene doel van deze thesis is om kwantitatieve MRI metingen van hersenvocht te onderzoeken als mogelijke maat voor het bestuderen van ziektes als SVD. Daarvoor hebben we verschillende invalshoeken gekozen, namelijk het kwantificeren van de perivasculaire ruimtes (PVS), het meten van de productiesnelheid van de cerebrospinale vloeistof (CSF), en het bepalen van verschillen in de samenstelling van de cerebrospinale vloeistof.

Perivasculaire ruimtes zijn ruimtes rond de (kleine) bloedvaten in het brein, die gevuld zijn met vloeistof. Deze vloeistof lijkt sterk op de vloeistof in de ventrikels (grote holtes) in de hersenen, de zogeheten liquor of CSF. De perivasculaire ruimtes spelen een belangrijke rol voor het bewaren van homeostase in het brein. Zo worden ze bijvoorbeeld geassocieerd met het afvoeren van afvalstoffen uit het brein. In ziektes als SVD worden meer en grotere perivasculaire ruimtes waargenomen dan in gezonde personen. In **Hoofdstuk 2** is een automatische methode gepresenteerd waarmee de perivasculaire ruimtes geannoteerd kunnen worden in T_2-gewogen MRI beelden. We hebben laten zien dat deze methode goed werkt in hoog-resolute 7T MRI beelden. Daarnaast kan met deze methode ook de lengte en kronkeligheid van de perivasculaire ruimtes bepaald worden, maten die moeilijk handmatig te verkrijgen zijn. Omdat 3T MRI echter veel breder beschikbaar is dan 7T MRI, zou een methode om het aantal perivasculaire ruimtes te kunnen bepalen in 3T MRI beelden met een lage resolutie, zeer waardevol zijn. Aangezien het aantal zichtbare perivasculaire ruimtes in laag-resolute beelden sterk samenhangt met de gebruikte scan sequentie en de exacte resolutie van de scan, was de verwachting dat het annoteren van perivasculaire ruimtes geen geschikte methode is voor deze beelden. Daarom hebben we onderzocht of textuurmaten van de 3T MRI beelden kunnen dienen als maat voor het aantal perivasculaire ruimtes in de hoog-resolute

7T MRI beelden (**Hoofdstuk 3**). Er werd echter geen correlatie gevonden tussen deze textuurmaten en het aantal perivasculaire ruimtes in de 7T beelden.

De cerebrospinale vloeistof, ofwel het CSF, heeft verschillende functies voor het brein. Het CSF compenseert bijvoorbeeld voor het variërende intracraniële bloedvolume over de hart- en ademhalingscycli, en CSF wordt in verband gebracht met het afvoeren van afvalstoffen uit het brein.

Er wordt vermoed dat de aanvoer van nieuw CSF belangrijk is voor het behouden van homeostase in het brein. De algemene consensus is dat CSF wordt geproduceerd door de choroïde plexus, en vervolgens vanuit de ventrikels via het cerebrale aquaduct richting de subarachnoïdale ruimte en de ruggengraat stoomt. Met fase-contrast MRI wordt vaak de netto CSF stroming door het aquaduct over de hartslag bepaald als maat voor de CSF productie. We hebben echter laten zien dat deze metingen sterk beïnvloed worden door de ademhalingscyclus (**Hoofdstuk 4**). Als gevolg hiervan was de reproduceerbaarheid van de metingen slecht. Door de fase-contrast MRI metingen te synchroniseren met de ademhaling kon de reproduceerbaarheid sterk verbeterd worden. Daarnaast werd ook een correlatie gevonden tussen het slagvolume en het verschil in netto CSF verplaatsing tussen in- en uitademing.

Bij ziekte kan de afvoer van afvalstoffen via het CSF verminderen, wat kan leiden tot een veranderde samenstelling van CSF. Zo is bij de ziekte van Alzheimer de concentratie van amyloid-β in CSF gereduceerd. In een eerder onderzoek werd een T_2 verschil gevonden tussen het CSF in de ventrikels en het CSF in de subarachnoïdale ruimte. Hierbij werd de hypothese gesteld dat dit T_2 verschil veroorzaakt wordt door verschillen in de lokale CSF samenstelling. In **Hoofdstuk 5** werd het T_2 verschil gereproduceerd, maar werd ook gevonden dat factoren als partieel volume en B_0-gradiënten sterk bijdragen aan het T_2 verschil. Door deze verstorende factoren bleek het in de praktijk onmogelijk om het effect van het intracraniële verschil in CSF samenstelling op de gemeten CSF T_2 tijden te onderscheiden.

In deze thesis hebben we de waarde van MRI onderzocht voor metingen aan hersenvocht als parameter voor onderzoek naar bijvoorbeeld de vroege stadia van SVD. De automatische methode voor het kwantificeren van perivasculaire ruimtes is een veelbelovende techniek. Op dit moment kan met deze methode één 2D plak geanalyseerd worden, in de toekomst kan dit worden uitgebreid naar een 3D methode. De PVS kunnen nog niet gekwantificeerd worden in 3T MRI beelden, maar technieken als non-lineaire analyses of deep learning kunnen wellicht uitkomst bieden. De fase-contrast metingen van netto CSF stroming in het aquaduct bleken niet geschikt om de CSF productie te bepalen.

Onze resultaten lieten echter zien dat metingen van de CSF verplaatsing over de hart- en ademhalingscycli wel de mogelijkheid bieden om de CSF dynamica in het brein in meer detail te onderzoeken. Tenslotte bleek dat het bepalen van intracraniële verschillen in de CSF samenstelling op basis van de T_2 van CSF op dit moment toekomstmuziek blijft. Het is echter wel mogelijk dat met de T_2 van CSF meer inzicht verkregen kan worden in de verschillen in de CSF samenstelling tussen groepen. We kunnen concluderen dat hersenvocht een zeer uitdagende parameter is, en er zijn nog verscheidene hordes die overwonnen moeten worden voor kwantitatieve MRI metingen van hersenvocht toegepast kunnen worden in klinisch onderzoek.

Addendum

List of publications

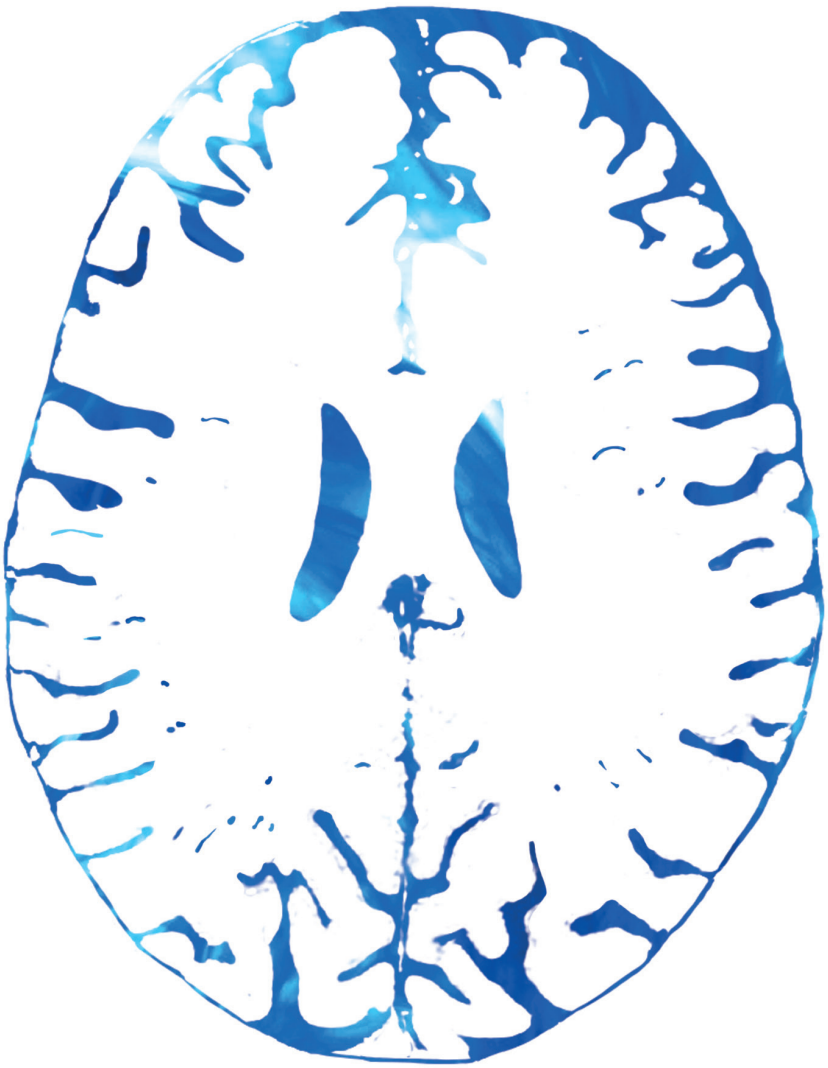

Peer-reviewed publications

Jolanda M. Spijkerman, Lennart J. Geurts, Jeroen C.W. Siero, Jeroen Hendrikse, Peter R. Luijten, Jaco J.M. Zwanenburg
Phase Contrast MRI measurements of net cerebrospinal fluid flow through the cerebral aqueduct are confounded by respiration.
Journal of Magnetic Resonance Imaging. (2018) [Epub ahead of print]

Jolanda M. Spijkerman, Esben T. Petersen Jeroen Hendrikse Peter Luijten Jaco J.M. Zwanenburg
T_2 mapping of cerebrospinal fluid: 3 T versus 7 T.
Magnetic Resonance Materials in Physics, Biology and Medicine. 31, 415-424 (2018).

Jill B. De Vis, Jaco J.M. Zwanenburg, Lisa A. van der Kleij, **Jolanda M. Spijkerman**, Geert-Jan Biessels, Jeroen Hendrikse, Esben T. Petersen
Cerebrospinal fluid volumetric MRI mapping as a simple measurement for evaluating brain atrophy.
European Radiology. 26, 1254-1262 (2016).

Submitted manuscript

Jolanda M. Spijkerman, Jaco J.M. Zwanenburg, Willem H. Bouvy, Mirjam I. Geerlings, Geert-Jan Biessels, Jeroen Hendrikse, Peter R. Luijten[1], Hugo J. Kuijf
Automatic quantification of perivascular spaces in T_2-weighted images at 7T MRI

In preparation

Jolanda M. Spijkerman, Bas H.M. van der Velden, Geert-Jan Biessels, Jeroen Hendrikse, Peter R. Luijten, Jaco J.M. Zwanenburg, Hugo J. Kuijf
Assessing the perivascular spaces count using texture features in 3T MRI scans: a feasibility study

Conference presentations (first author only)

Jolanda M Spijkerman, Lennart J Geurts , Jeroen C.W. Siero , Jeroen Hendrikse , Peter R. Luijten, Jaco J.M. Zwanenburg - *PC-MRI measurements of net CSF flow through the cerebral aqueduct strongly depend on respiration.*
Oral presentation, ISMRM 2018, Paris, France
Oral presentation, ISMRM Benelux 2018, Antwerp, Belgium (2nd best presentation award)

Jolanda M. Spijkerman, Hugo J. Kuijf, Willem H. Bouvy, Miriam I. Geerlings, Jeroen Hendrikse, Peter R. Luijten, Jaco J.M. Zwanenburg
Quantitative measurements of perivascular spaces at 7T, using a semi-automatic tracking method.
E-poster presentation, ISMRM 2017, Honolulu, Hawaii
Power poster presentation, ISMRM Benelux 2017, Tilburg, the Netherlands

Jolanda M. Spijkerman, Jeroen C.W. Siero, Lennart J. Geurts, Matthew J. Donahue, Jeroen Hendrikse, Peter R. Luijten, Jaco J.M. Zwanenburg
Quantification of cerebrospinal fluid flow through the cerebral aqueduct using 7T MRI.
Poster presentation, ISMRM 2017, Honolulu, Hawaii

Jolanda M. Spijkerman, Esben T. Petersen, Peter R. Luijten, Jeroen Hendrikse, Jaco J.M. Zwanenburg
T_2 mapping of ventricular cerebrospinal fluid (CSF) at 7 Tesla with comparison to 3T.
E-poster presentation, ISMRM 2016, Singapore

Jolanda M. Spijkerman, Jill B. de Vis, Esben T. Petersen, Jeroen Hendrikse, Peter R. Luijten, Jaco J.M. Zwanenburg
T_2 measurements during hyperoxia in the lateral ventricles and peripheral CSF.
E-poster presentation, ISMRM 2016, Singapore

Jolanda M. Spijkerman, Esben T. Petersen, Peter R. Luijten, Jeroen Hendrikse, Jaco J.M. Zwanenburg
Influence of partial volume effects on T_2 mapping of cerebrospinal fluid.
Poster presentation, ISMRM Benelux 2016, Eindhoven, the Netherlands

Jolanda M. Spijkerman, Esben T. Petersen, Peter R. Luijten, Jeroen Hendrikse, Jaco J.M. Zwanenburg
A fast method for T_1 and T_2 mapping of cerebrospinal fluid at 7T.
E-poster presentation, ISMRM 2015, Toronto, Canada
Poster presentation, ISMRM Benelux 2015, Ghent, Belgium

Addendum

Dankwoord
Acknowledgements

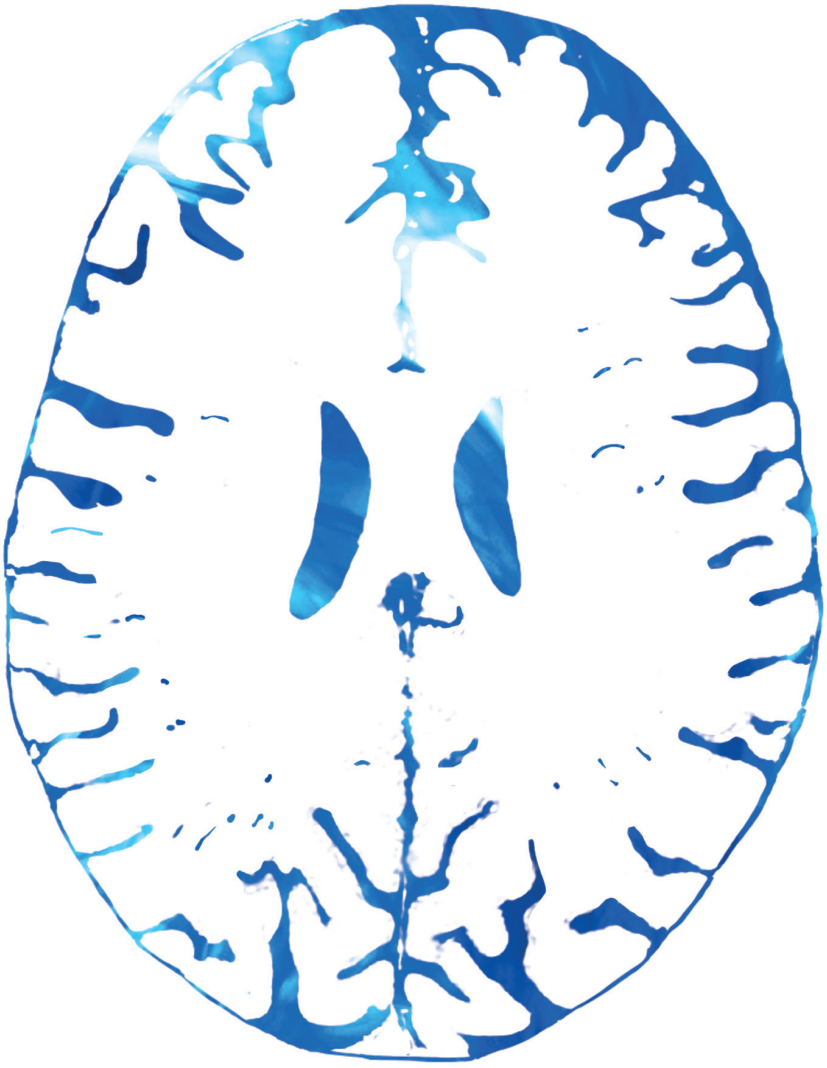

Graag wil ik hier iedereen bedanken die heeft bijgedragen aan dit proefschrift. Dankzij al jullie bijdragen en steun ben ik tot dit eindresultaat gekomen. In het bijzonder wil ik ook alle vrijwilligers bedanken die voor mij in de scanner zijn geweest, want zonder hen was dit onderzoek niet mogelijk geweest. Ook wil ik graag iedereen bedanken die mij hulp, aanmoediging, of de broodnodige afleiding hebben geboden.

Prof. dr. Luijten, beste Peter, bedankt dat ik deel mocht uitmaken van de 7T groep. Het is een unieke, diverse groep waarin technici en clinici samenkomen. De openheid en hulpvaardigheid van alle collega's in de groep hebben me erg geholpen bij het voltooien van dit proefschrift.

Prof. dr. Hendrikse, beste Jeroen, ik heb veel bewondering voor je niet-aflatende positiviteit en je vele onderzoeksideeën. Ik ben erg gaan waarderen hoe je geregeld langs onze kamer kwam om te vragen hoe het ervoor stond.

Dr. ir. Zwanenburg, beste Jaco, jij was mijn dagelijkse begeleider tijdens dit promotietraject. Dit was je ook letterlijk: ik kon altijd bij je binnenwippen voor input, en ook tijdens scansessies in weekenden was je altijd bereikbaar om een helpende hand te bieden. Ik heb in de afgelopen jaren veel opgestoken van je brede kennis en kritische blik.

De leescommissie, bestaande uit prof. dr. Dijkhuizen, prof. dr. Verkooijen, prof. dr. Velthuis, prof. dr. de Jong, en prof. dr. Nederveen, hartelijk bedankt voor de tijd en energie die jullie hebben gestoken in het beoordelen van dit proefschrift.

Beste co-auteurs, bedankt voor de waardevolle bijdragen aan de hoofdstukken in dit proefschrift. Hugo, bedankt voor je ideeën en je hulp met de scripts voor het kwantificeren van de perivasculaire ruimtes. Als ik die had moeten missen had het een stuk langer geduurd voor mijn proefschrift af was. In het bijzonder ook wil ik de co-auteurs van Hoofdstuk 3 bedanken voor hun snelle inzet. Bas en Hugo, jullie hebben gemerkt hoe irritant vaak ik kan vragen of er al resultaten zijn, en leken me toch nooit niet echt zat te raken: bedankt daarvoor! En prof. dr. Biessels, Geert-Jan, Jeroen, Peter en Jaco, bedankt voor jullie snelle feedback op het manuscript.

Beste Roy, bedankt voor het maken van de layout en cover van dit boekje, en voor het achter mijn broek zitten om alles aan te leveren, aangezien dat er soms bijna bij inschoot met alle drukte..!

Beste Sylvia, pas nu ik een tijdje weg ben realiseer ik me pas echt hoezeer jij de spil van de 7T groep bent. Je zorgt er altijd met verve voor dat alles op tijd geregeld wordt, maar bent ook altijd in voor een gezellig praatje!

Door de jaren heen heb ik stiekem best veel kamerenoten versleten: Lennart, Esben, Nils, Nikki, Lidy en Rashid, bedankt voor alle kletspraatjes tussen het werken door. Nikki, dankjewel voor je opbeurende woorden, hulp met figuren en statistiek, en natuurlijk alle gezelligheid! Je bent een echte vriendin geworden, en hebt heel veel bijgedragen aan de leuke tijd die ik in de 7T groep heb gehad!

Ook alle collega's van de 7T groep: inmiddels is de groep te groot geworden om iedereen hier op te noemen, maar ik wil jullie enorm bedanken voor de gezelligheid tijdens lunchpauzes, borrels, filmavondjes, en congressen.

Lieve paranimfen, Lisa en Tine, jullie waren niet alleen heel gezellige collega's, maar stonden ook altijd klaar met een luisterend oor of een helpende hand. Super dat jullie achter mij staan op deze belangrijke dag!

Lieve vriendinnen, Iris, Evelyn, Eva, we zien elkaar niet altijd even vaak, maar we gaan eigenlijk altijd door waar we gebleven waren. Wonderlijk hoe goed een gezellige avond bijkletsen kan helpen om weer op te laden!

Lieve schoonfamilie, Jos, Karien, Jos, en Sigrid, bedankt voor de interesse in mijn promotie-onderzoek de afgelopen jaren. En ook heel erg bedankt dat jullie niet doorvroegen als ik even helemaal niet aan mijn promotie wilde denken!

Lieve familie, heel erg bedankt voor alle steun, die had ik soms echt nodig! Rein, zo kalm als jij kunt zijn heb je me erg geholpen om de boel te relativeren. Marion, ik volg nu in je voetsporen, jij hebt mij op 20 december natuurlijk al het goede voorbeeld gegeven! Het was ook ontzettend fijn om soms even flink te klagen bij jou, dat luchtte enorm op! Luuk, bedankt ook voor je steun en je begrip als er weer een uitwisseling van promotie-verhalen voorbij kwam. Papa en mama, enorm bedankt voor jullie onvoorwaardelijke steun en toewijding. Net zoals ik hadden jullie niet verwacht dat ik deze weg zou inslaan, maar alles is op z'n pootjes terecht gekomen. Hoewel jullie niet altijd precies begrepen waar ik mee bezig was, boden jullie altijd een luisterend oor en wilden jullie altijd meedenken aan een oplossing als ik ergens tegenaan liep

Lieve Fons, zonder jou had ik dit proefschrift nooit af gekregen. Al meer dan 11 jaar ben je de constante factor in mijn leven, ondanks al mijn (soms best heftige) ups en downs die je over je heen hebt gekregen. Je bent echt mijn rots in de branding, hoe afgezaagd het ook klinkt! Zeker in het afgelopen jaar, waarin we alles tegelijk lijken te doen: mijn promotie en nieuwe baan, de verhuizing, en straks de kleine. Ik zou het niet zonder jou kunnen of willen!

Addendum

Biography

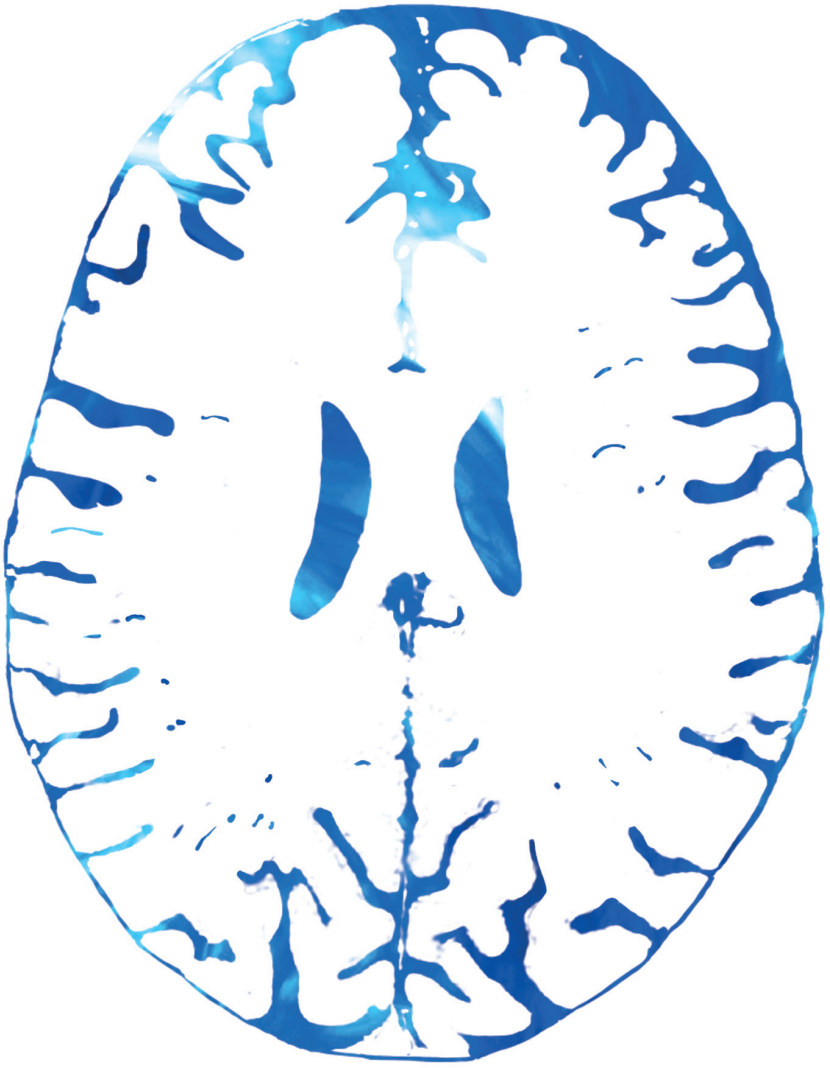

Jolanda Margaretha Spijkerman was born on November 10th 1989 in Nyköping, Sweden. When she was 2 years old she moved with her family to Woensdrecht, the Netherlands, where she grew up. She attended the Gymnasium Juvenaat H. Hart in Bergen op Zoom, where she gained an interest in the technology used in healthcare and especially in medical imaging. After obtaining her diploma, she moved to Eindhoven for the bachelor study Biomedical Engineering. During her master study Medical Engineering she spent her short internship at the Danish Research Center for Magnetic Resonance in Copenhagen, where she worked on fMRI data. During her master thesis project she worked on registration of pre- and post-treatment PET-CT scans of lung cancer patients in Maastro Clinic, which resulted in her first scientific journal publication. After obtaining her Master's degree, she successfully applied for a PhD position in the 7 Tesla group in the UMC Utrecht, where she worked on quantitative MRI of brain fluids under the supervision of Prof. Dr. Peter R. Luijten, Prof. Dr. Jeroen Hendrikse, and Dr. Ir. Jaco J.M. Zwanenburg. Currently she is working on the safety aspects of a new type insert-gradient coil at the Donders Institute for Brain, Cognition, and Behavior in Nijmegen and at MR Coils BV in Zaltbommel.